TIP LEAKAGE FLOW IN A LINEAR TURBINE CASCADE

by

James S. Tilton

Thesis submitted to the Graduate Faculty of the

Virginia Polytechnic Institute and State University

in partial fulfillment of the requirements for the degree of

MASTER OF SCIENCE

in

Mechanical Engineering

APPROVED:

J. Moore, Chairman

W. F. O'Brien

H. L. Moses

August 1986

Blacksburg, Virginia

TIP LEAKAGE FLOW IN A LINEAR TURBINE CASCADE

by

James S. Tilton

ABSTRACT

An experimental investigation was performed to study the details of flow in the tip clearance gap of a linear turbine blade cascade. The cascade was designed and built to be geometrically similar to the earlier VPI&SU cascade; however, the new cascade also had a tip gap (2.1 percent of blade height) and two endwall boundary layer bleeds upstream of the blade row. The boundary layer bleeds were designed to reduce secondary flow other than the tip gap leakage flow in the cascade, and they performed well. The cascade flow had an exit Reynolds number based on the axial chord of 4.5×10^5.

Static pressure measurements were made on the blades and on the endwall with particular attention given to the tip gap. Also, flow visualizations on the endwall and on the suction surface of the middle blade were performed.

From the pressure measurements, a minimum static pressure coefficient of -6.85 (based on the freestream velocity head) was obtained along the bottom of the blade, near the tip gap inlet. A vena contracta was evident, also in the tip gap entrance region, and a contraction coefficient of 0.61 was calculated from measured data. Mixing occurred after the vena contracta with the static pressure across the tip gap exit being fairly uniform. The flow visualizations showed a separation and reattachment on the endwall under the blade and a tip gap

leakage vortex in the passage.

Models of the tip gap flow, based on potential flow theory and potential flow theory with mixing were discussed and developed. Potential flow theory accurately models the unloading along the pressure surface of the blade, and the endwall static pressure distribution of the tip gap, up to the vena contracta. It also predicts a contraction coefficient of 0.61.

The combined potential flow and mixing model accounts for the pressure rise in the tip gap due to mixing. It predicts a minimum static pressure coefficient under the blade of -6.81, which agrees well with measured data.

ACKNOWLEDGEMENTS

This work was conducted under the sponsorship of Rolls-Royce plc., Aero Division, England.

The author would like to give special thanks to his advisor, Dr. John Moore, whose help was invaluable. Thanks also go to Professors Hal L. Moses and Walter F. O'Brien for being the other two members of the author's advisory committee. C. L. (Jack) Gray, Jerry R. Lucas, and all the other technicians in the machine shop deserve recognition for the important assistance they rendered during this project.

This thesis is dedicated in the memory of the author's father, Winfield S. Tilton, to his mother, Joyce M. C. Tilton, who provided incalculable amounts of love and support, and to his Lord, Jesus Christ, who was his pillar of strength.

TABLE OF CONTENTS

TABLE OF CONTENTS (continued)

LIST OF FIGURES

LIST OF FIGURES (continued)

LIST OF FIGURES (continued)

LIST OF TABLES

NOMENCLATURE

A	station A (Fig. 5)
B	station B (Fig. 5)
c	chord
C	station C (Fig. 5)
C_c	contraction coefficient
cp_s	static pressure coefficient
D	station D (Fig. 5)
E	station E (Fig. 5)
L	flow line (Fig. 22)
M	pressure maximum (Fig. 22)
P	pressure
P_{exit}	tip gap exit pressure
P_s	local static pressure
P_{so}	endwall static pressure upstream of blade 3
P_1	upstream pressure
P_2	downstream pressure
$\dot{Q}$	volume flow rate through tip gap per unit length
r	radius
R	reattachment line (Fig. 22)
S	separation line (Fig. 22)
U	velocity
U_{max}	maximum velocity in tip gap
U_o	upstream freestream velocity
W_t	velocity reached in tip gap with potential flow analysis
δ_t	tip gap height

δ_{99} boundary layer thickness

δ^* displacement thickness

Δz span

ζ complex velocity

H_{12} shape factor = δ^*/θ

σ contraction ratio

θ momentum thickness

I. INTRODUCTION

The desire to improve efficiency and increase performance in turbine blade design has fueled much research into flow modeling. Two dimensional flow calculations were found to be limited in their accuracy due to three dimensional effects and their associated losses (termed secondary losses), present in turbomachinery. This inadequacy required that the three dimensionality of flow through turbomachinery passages be studied. In the last few years, much progress has been made in this area. Most studies, however, have not included the loss mechanism of flow under the blade tip. This flow can reduce the blade loading and adversely affect the turbine performance.

Tip leakage flows are caused by the clearance between the rotor blade ends and the engine casing. The difference in pressure on the sides of the turbine blades drives the flow through the tip gap and creates a vortex near the endwall, in the suction surface corner region of the blade.

Attempts to control tip leakage flow are based on minimizing the discharge coefficient under the blade tip. Some efforts have been made to alter the discharge coefficient by modifying the tip geometry [1]. To effectively alter the discharge coefficient, however, the flow behavior in the tip gap region must be understood.

In this study, details of the flow in the tip clearance gap are investigated. Models of tip gap leakage flow based on potential flow theory and potential flow theory with mixing are discussed and developed. The contribution of this investigation is to gain increased knowledge of the mechanisms of tip leakage flow, and to aid in

developing methods for further reducing the tip gap discharge coefficient.

II. LITERATURE REVIEW

Three dimensional effects in turbine blade cascades without tip clearances have been well documented [2,3,4,5,6,7]. This is not to say that the study of tip leakage flows is a new subject. Herzig, Hansen, and Costello [8] looked at this while examining flow through a cascade of thin blades. Utilizing smoke for flow visualizations, they made some important observations. First, the tip leakage vortex rotated in the opposite direction to that of the passage vortex. Instead of mixing together, the tip leakage vortex stayed close to the suction surface of the blade and displaced the passage vortex more toward the center of the channel. Also, moving endwalls decreased the tip leakage flow by creating a scraping of the endwall boundary layer that could, with a small enough tip gap, cancel the effects of the tip clearance.

Roelke [9] developed a general order of magnitude estimate of the increase of inefficiency in a turbine due to tip leakage, see Fig. 1. While the inefficiency is shown dependent on the reaction of the turbine, the rough estimate of a 2 percent loss for every 1 percent in tip clearance as a fraction of blade height seems quite accurate.

Rains [10] considered flow through the tip gap of a compressor blade. He noted that the pressure gradient across the blade is much larger compared to that along the blade. Thus, the tip gap flow can be considered as normal to the camber line of the blade.

He presented an idealized flow model based on potential flow theory and also suggested a more plausible flow with separation, reattachment, and flow mixing. These two models are shown in Fig. 2.

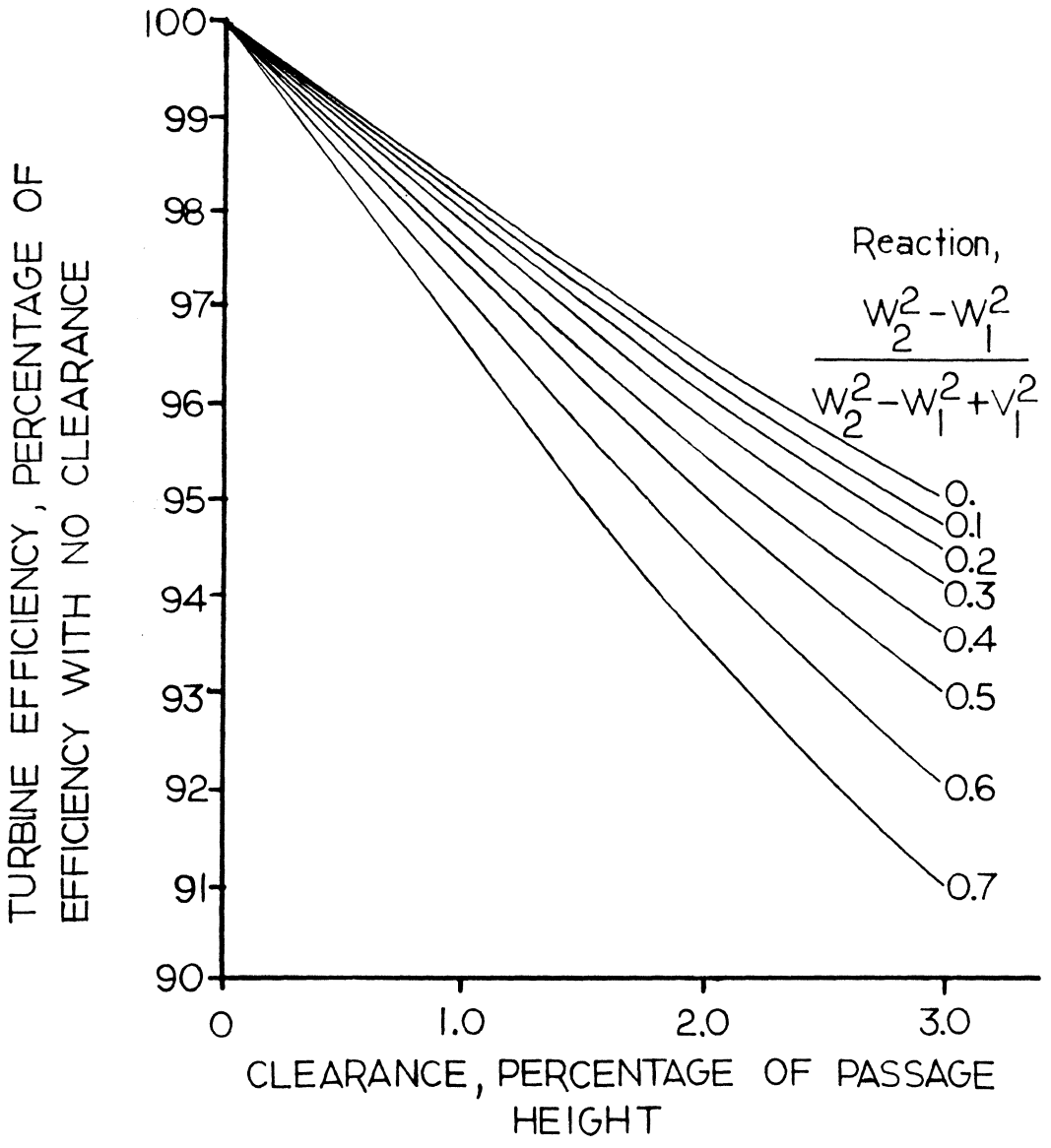

Fig. 1 Tip Clearance Correlation for Unshrouded Blades (after Roelke [9]).

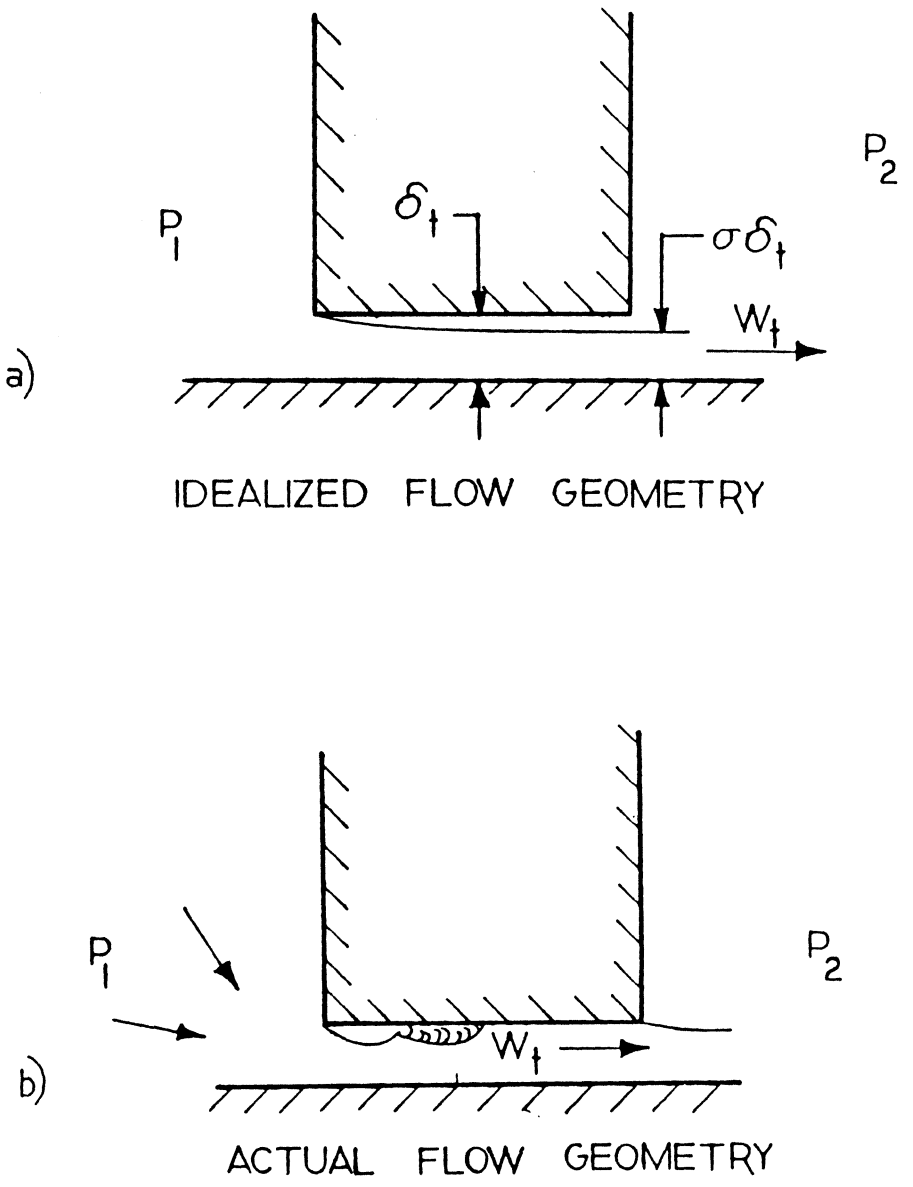

Fig. 2 Comparison of Tip Clearance Flow Geometries (after Rains [10]).

For the potential flow model Bernoulli's equation was applied between the conditions far upstream and downstream of the tip gap to give

$$W_t = \left[\frac{2(P_1 - P_2)}{\rho}\right]^{1/2} . \qquad (1)$$

Referring to Fig. 2a, the pressure all along the free streamline under the blade was taken as equal to P_2. The contraction ratio, σ, giving the ratio of the downstream jet width to the tip gap height, was determined to be 0.611. With the exception of tip pressure measurements made on the pressure and suction sides of the tip gap on the endwalls, no detailed experimental confirmation of his potential flow theory was provided.

Rains' "more plausible" model contains mixing after the vena contracta, shown in Fig. 2b.

Booth [9] stated that at normal tip clearances, 1-2 percent of the blade height, viscous effects are fairly small, being reduced to those creating separations and reattachments, but he did not mention mixing. He sought to reduce the tip gap discharge coefficient by adjusting the blade shape or loadings.

Booth [11] then modelled the tip gap leakage flow with a two-dimensional viscous analysis. His experimental data, from pressure taps located under the tip gap, but not including any on the blade tip, was compared against his theory and is shown in Fig. 3. His data indicated the pressure falls at the tip gap entrance and remains relatively constant, similar to what Rains' potential flow theory would predict.

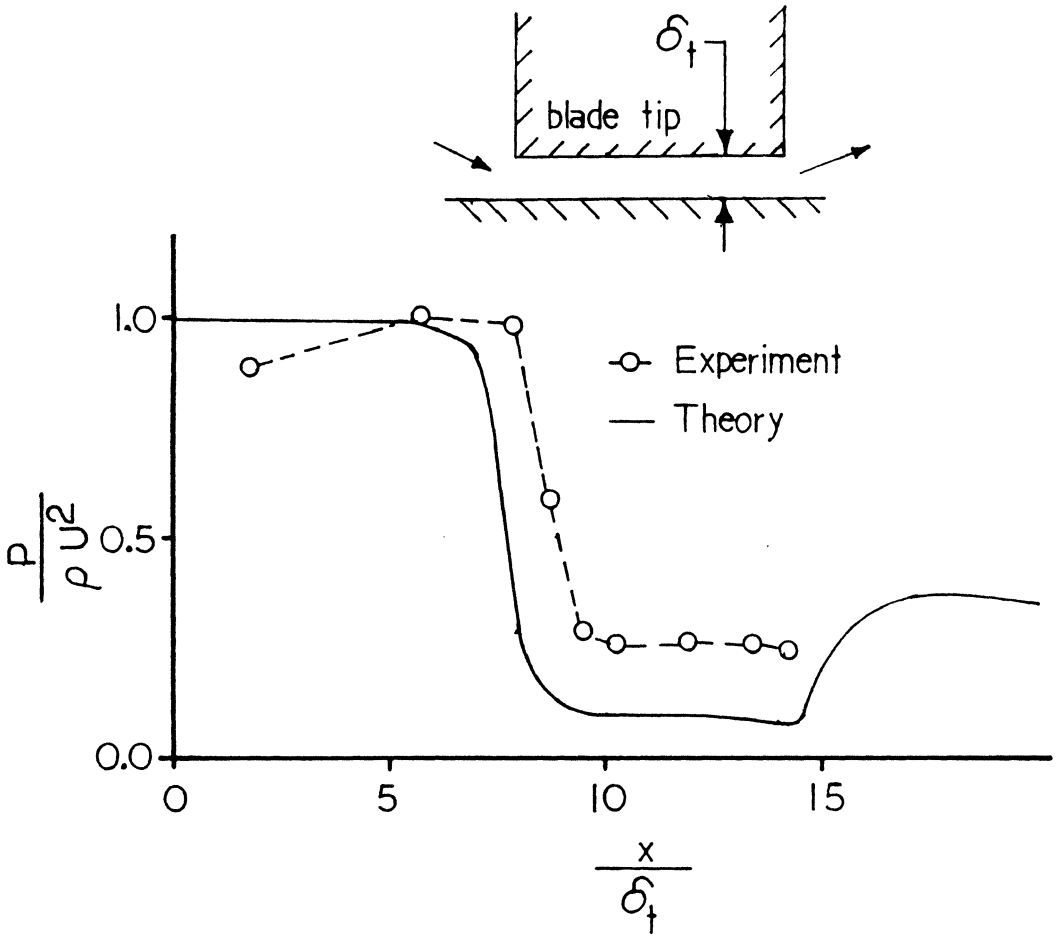

Fig. 3 Pressure Distribution Across the Blade Tip (after Booth [11]).

Lakshimarayana [12] studied only the effects of tip gap leakage flow and did not investigate the flow behavior in the tip clearance.

In this thesis, a model for the actual flow geometry, found to be similar to that shown in Fig. 2b, is developed. Hopefully, this flow model will be more accurate in predicting flow behavior in the tip gap region.

III. EXPERIMENTAL APPARATUS

The study was conducted using a low speed, open circuit wind tunnel, shown in Fig. 4. The equipment used is divided into six major categories:

A) The wind tunnel

B) The cascade test section

C) The blade row

D) The tip gap

E) The boundary layer bleeds

F) The measuring equipment

The wind tunnel and measuring apparatus required some reconstruction and upkeep, while the boundary layer bleeds and cascade test section had to be designed and built.

A. The Wind Tunnel

The wind tunnel was of a blower configuration, as shown in Fig. 4, with a blower motor power of 20.4 KW. Downstream of the diffuser was a plenum chamber responsible for straightening the flow. Directly following the plenum chamber, a nozzle contracted the flow to an area 0.91 m wide and 0.3 m high. The tunnel was equipped with an adjustable Plexiglas roof; however, for this study a constant tunnel height of approximately 0.3 m was maintained up to the boundary layer bleeds.

The bottom wall was constructed of a single piece of 19 mm plywood with 1.6 mm thick white Formica, creating a smoother and more consistent surface, covering the side exposed in the tunnel. The side walls, bolted to the tunnel, were built from various sized sections of 19 mm

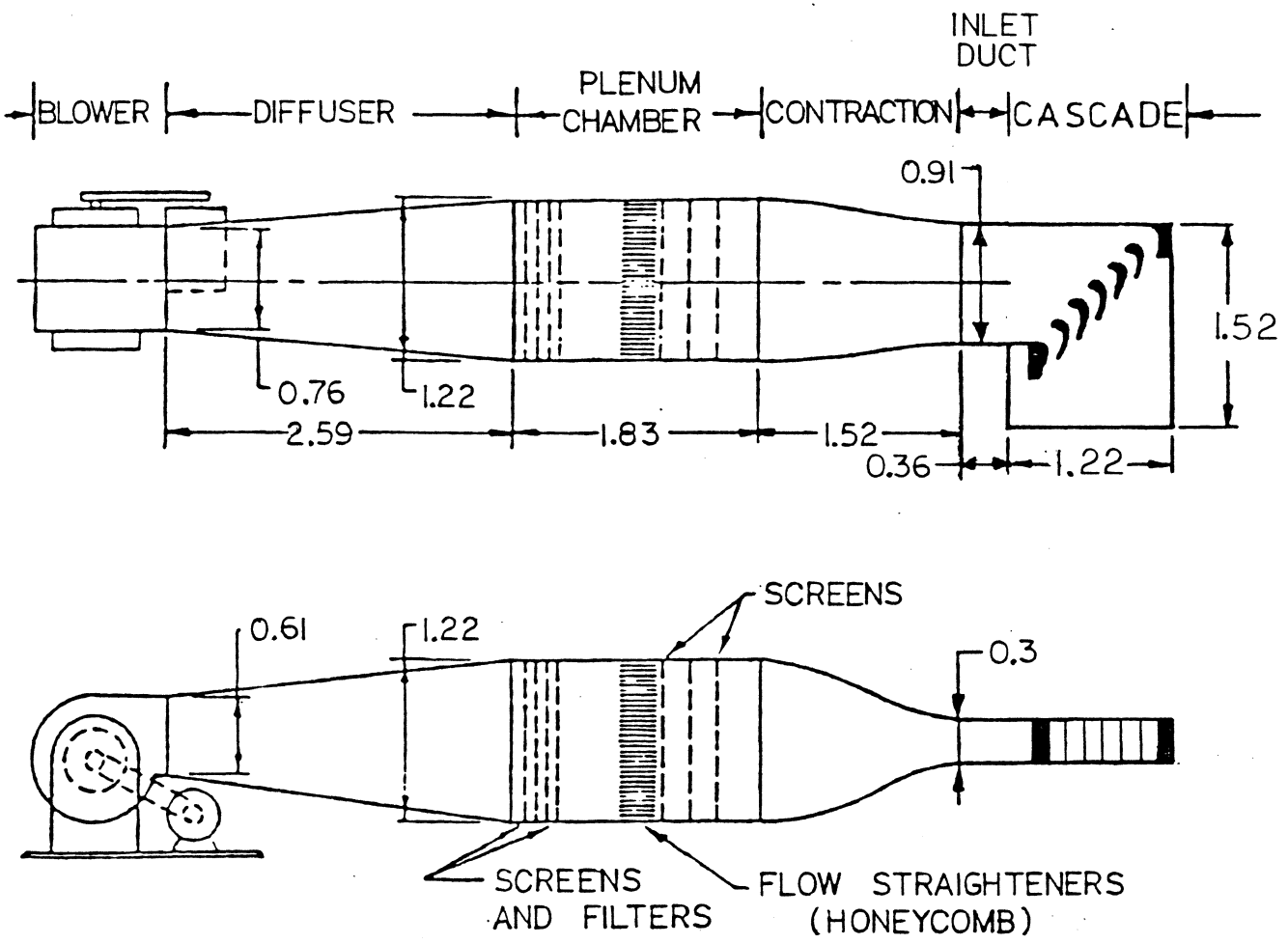

Fig. 4 Low Speed Wind Tunnel (all dimensions in meters)

plywood also lined with 1.6 mm thick white Formica, and two sections of 9.7 mm Plexiglas. The sectioning of the side walls allowed easy access to the tunnel, while the Plexiglas pieces also permitted visual inspection of the tunnel and apparatus. Joints and surface irregularities in the tunnel were filled with Plasticene.

The screens and filters in the wind tunnel and the diffuser were checked for blockages and obstructions.

B. The Cascade Test Section

A plan view of the cascade test section is shown in Fig. 5. Shown upstream of the blades in this view is the bleed for the bottom wall boundary layer, to be discussed later. Also included are three upstream static pressure tappings and five instrumentation ports. The two wooden bleeds, positioned on either end of the blade cascade, were adjustable to achieve flow repeatability. They slid, pivotting on threaded rods located in slots cut out in the plywood endwalls.

The three upstream instrumentation ports, lettered A, B, and C in Fig. 5, were used to insert a pitot probe to measure the inlet boundary layer thicknesses. Three more ports were located in the top endwall, directly above the ones shown. The two instrumentation ports in the blade passage, lettered D and E, were used to measure the velocity distribution as the flow left the tip gap.

C. The Blade Row

The cascade consisted of five blades and a pair of wooden bleeds, creating six passages. A top view of the blades, shown in Fig. 6, shows

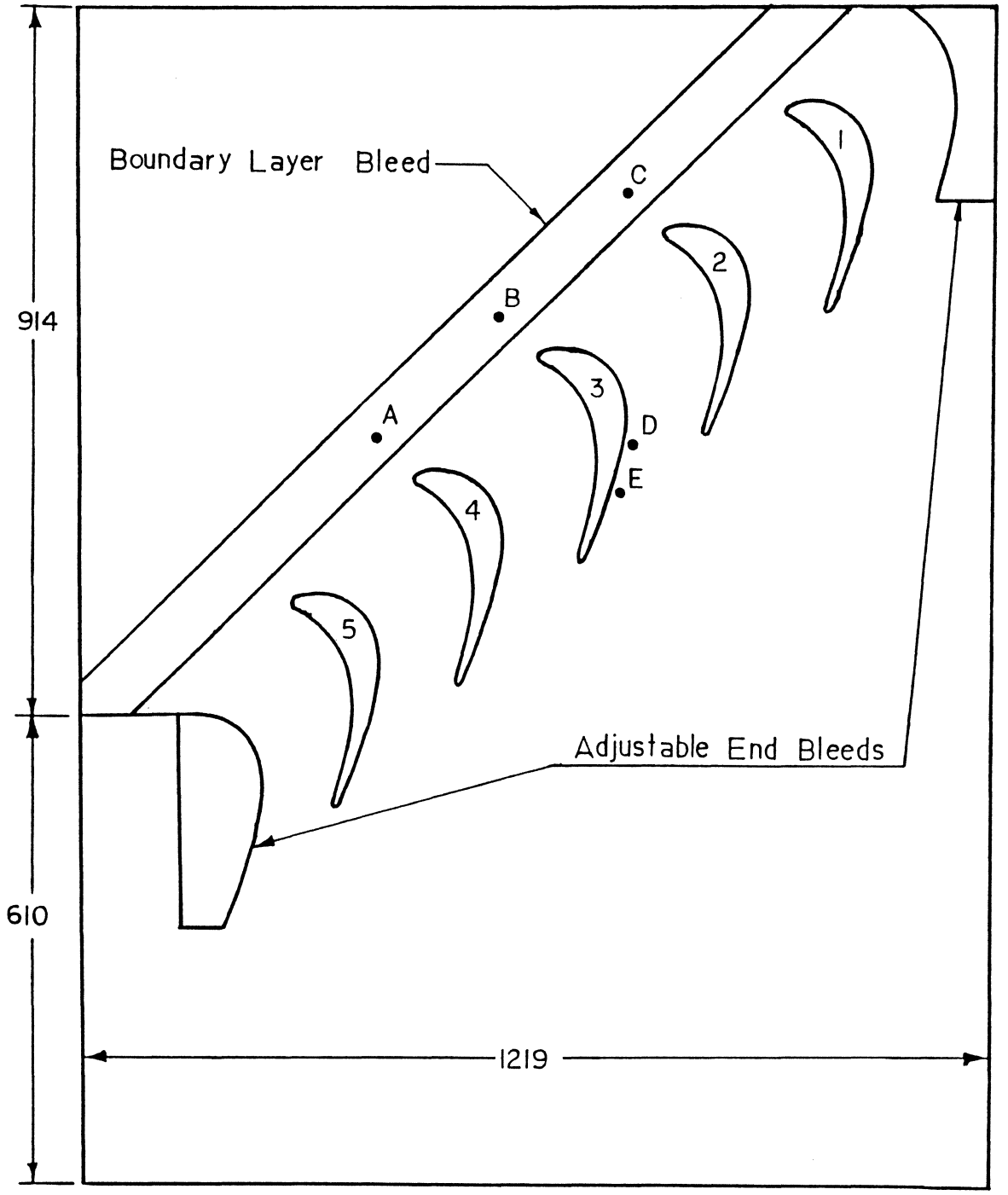

Fig. 5 Plan View of the Top Endwall of the Cascade Test Section (all dimensions in mm).

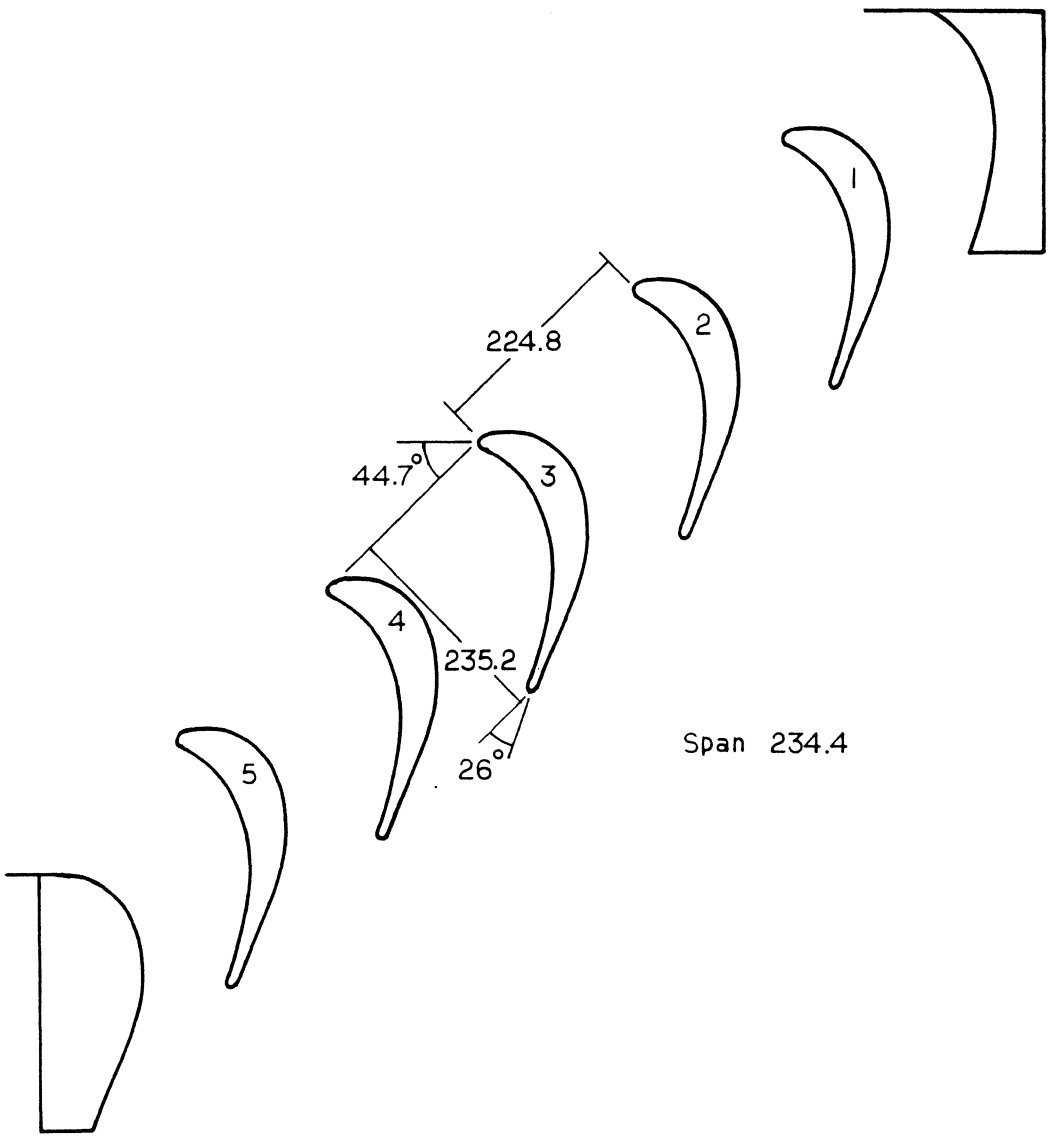

Fig. 6 Cascade Dimensions and Geometry (all linear dimensions in mm).

the numbering of the blades. The blades were designed to be almost identical to ones built earlier by Moore [13], and are geometrically similar to blades used by Langston [3]. This blade profile was chosen for the tip leakage study because of the previous work done on it here at VPI&SU, and in order to complement the wealth of information now available on it.

One major difference from Moore's previous turbine cascade was the presence of a tip gap, which necessitated that the blades be supported from one end only, the other end being the blade's bottom surface. Also, different locations for additional static pressure tappings were utilized. Other than this, the blades were constructed following the method described in reference 13. The blade sizes were not altered. A brief description of the blades will be given here.

Each blade was constructed using three 9.5 mm handmade aluminum formers, connected by six aluminum spacers, and covered on the pressure and suction surfaces by 3.2 mm thick Plexiglas. Screwed to the aluminum formers were a 25.4 mm outer diameter Plexiglas tube and a 14.3 mm diameter aluminum rod, forming the leading and trailing edges, respectively. The blade profile shape is given in Fig. 7. Figure 8 shows an exploded view of a similar blade from the previous VPI&SU turbine cascade [13]; this was used in earlier tests by Ransmayr, Smith, Adhye, and Shaffer.

The blade overall dimensions are:

Axial Chord	=	235.2 mm
Span	=	234.4 mm
Pitch	=	224.8 mm.

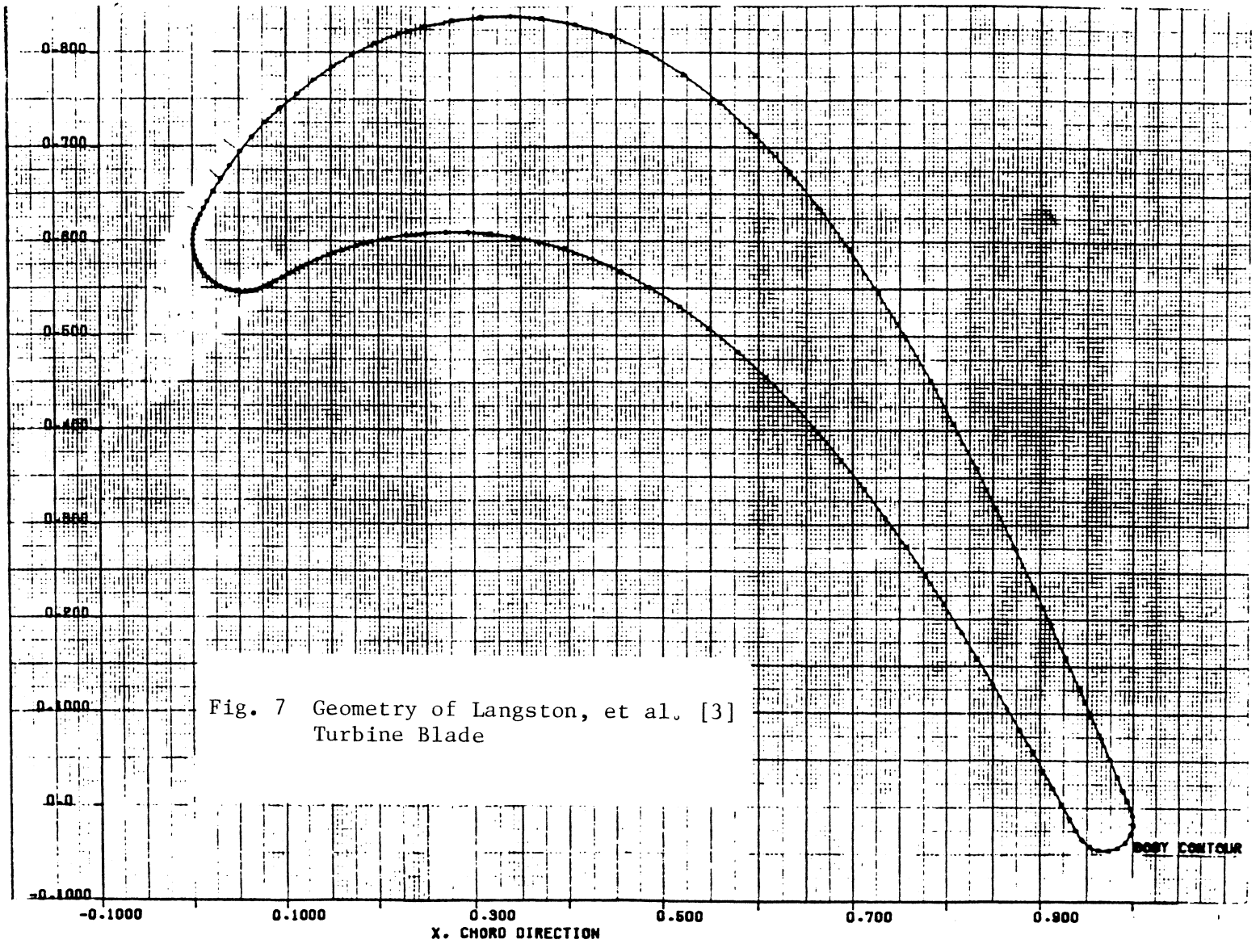

Fig. 7 Geometry of Langston, et al. [3] Turbine Blade

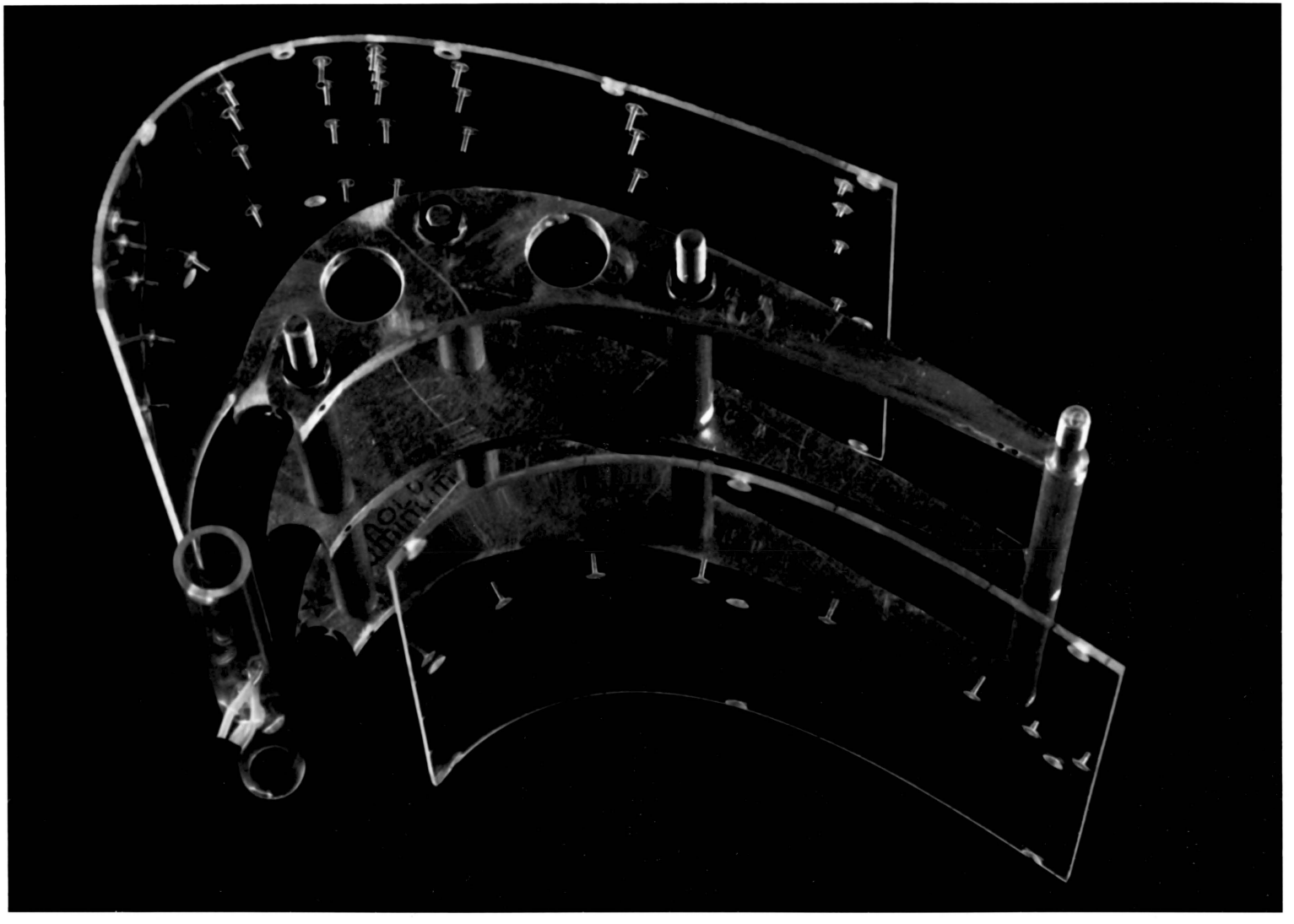

Fig. 8 Example of Blade Construction Technique [15], Showing Individual Components.

The airfoil section is that of a reaction turbine rotor with mean camber line angles of $\beta_1 = 43.99°$ and $\beta_2 = 25.98°$, giving a nominal turning angle of 110° and a velocity ratio of 1.6. The air inlet angle is 44.7°, close to zero incidence. The Zweifel loading parameter is 1.124.

The leading edges, the middle blade (blade 3), and the pressure side of blade 2 were instrumented with static pressure tappings. These locations will be discussed in Section V.A.1. In the Plexiglas the diameter of the holes for the tappings was 0.51 mm. Across the bottom wall of blade 3, in the aluminum former, the diameter of the holes was 0.76 mm. Tygon tubing was attached to either brass fittings epoxied to the Plexiglas sides, or steel tubes epoxied to the bottom aluminum former.

The five blades were bolted through the top endwall to a piece of 101 mm channel aluminum, which was secured to the two wooden end bleeds. The wooden bleeds had no tip gap and were themselves bolted to the top and bottom endwalls.

A cross-section of the blade showing construction details is shown in Fig. 9.

Trip wires of 0.51 mm diameter were epoxied to the blade surface in an attempt to start a uniform turbulent profile boundary layer in the spanwise direction. They were located approximately 3 mm downstream of the joint of the leading edge Plexiglas tube and the two Plexiglas sides. The areas of contact between the Plexiglas sides and the bottom aluminum former were bonded together with silicon rubber to prevent any air leaks into the tip gap region. All surface irregularities were

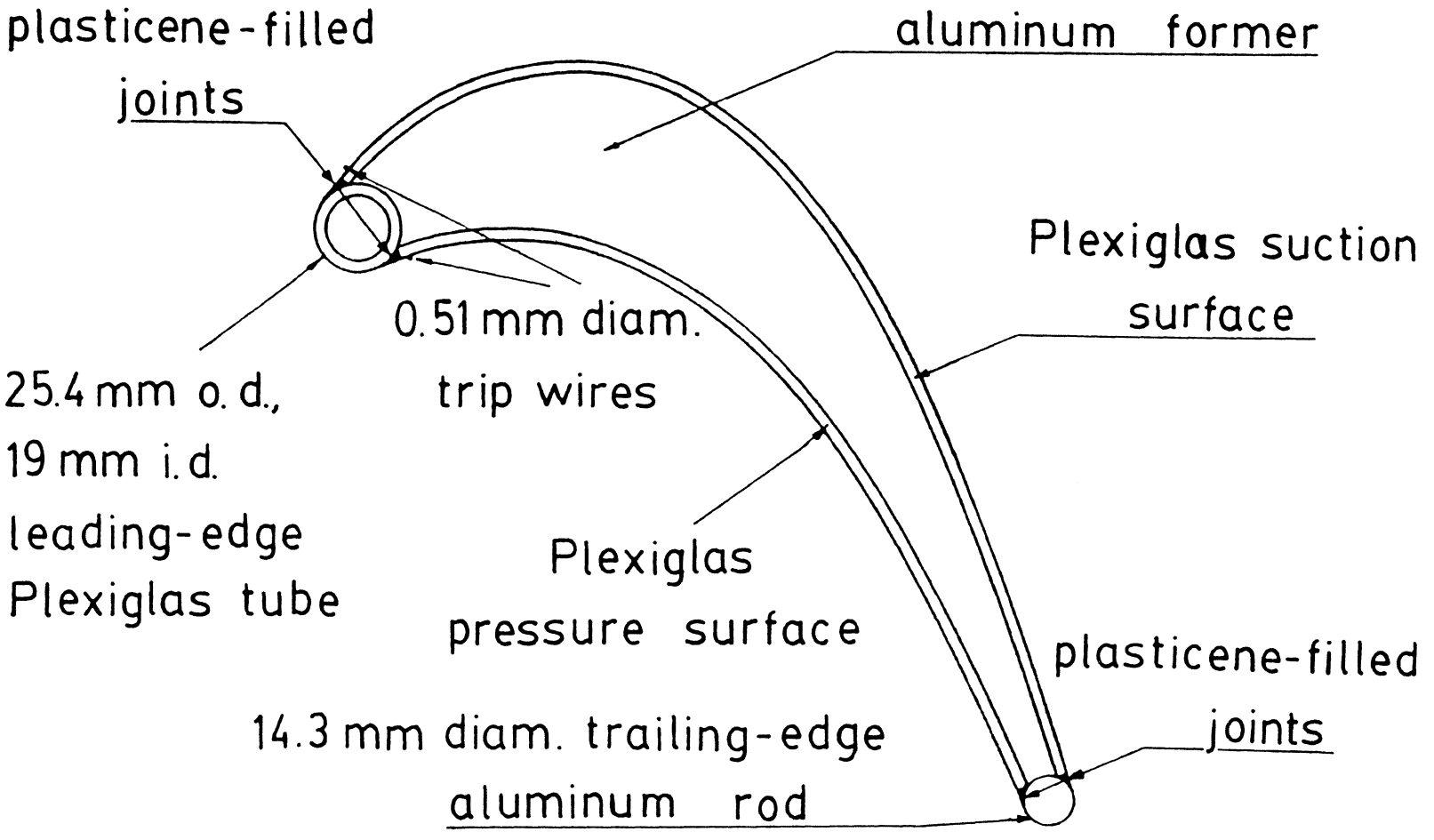

Fig. 9 Cross-section of Turbine Blade Showing Details of the Blade Construction.

removed and joints and countersunk screw holes were filled with plasticene to create a smooth surface.

D. The Tip Gap

The final tip gap selected was 2.1 percent of the blade span, 5.0 mm. Across the blade row, the tip gap varied from 2.0 to 2.3 percent, as shown in Fig. 10. However, for the middle three blades, the variation was only between 2.0 and 2.1 percent. Typically, turbines run with tip gaps in the range of one to three percent.

Using Graham's [14] tentative plot of various tip leakage flow regimes, Fig. 11, a tip clearance of at least 1.2 percent, which covers most turbines, in an engine operating at standard speed will produce a tip leakage vortex. A 2.1 percent tip clearance at zero endwall speed will also produce this flow behavior; thus, our study will represent most real life situations.

An upstream view showing the tip gap in relation to a blade passage is shown in Fig. 12.

E. The Boundary Layer Bleeds

Two boundary layer bleeds, one on either endwall upstream of the blade row were constructed. They reduced the size of the endwall boundary layers as they entered the blade cascade. The purpose of this was to reduce other secondary flows so that the three dimensional flow development would be dominated by the tip gap leakage flow. The earlier tests with the VPI&SU turbine cascade used a thick inlet boundary layer, $\delta_{99}/\Delta z = 0.162$. Here an attempt was made to reduce the inlet

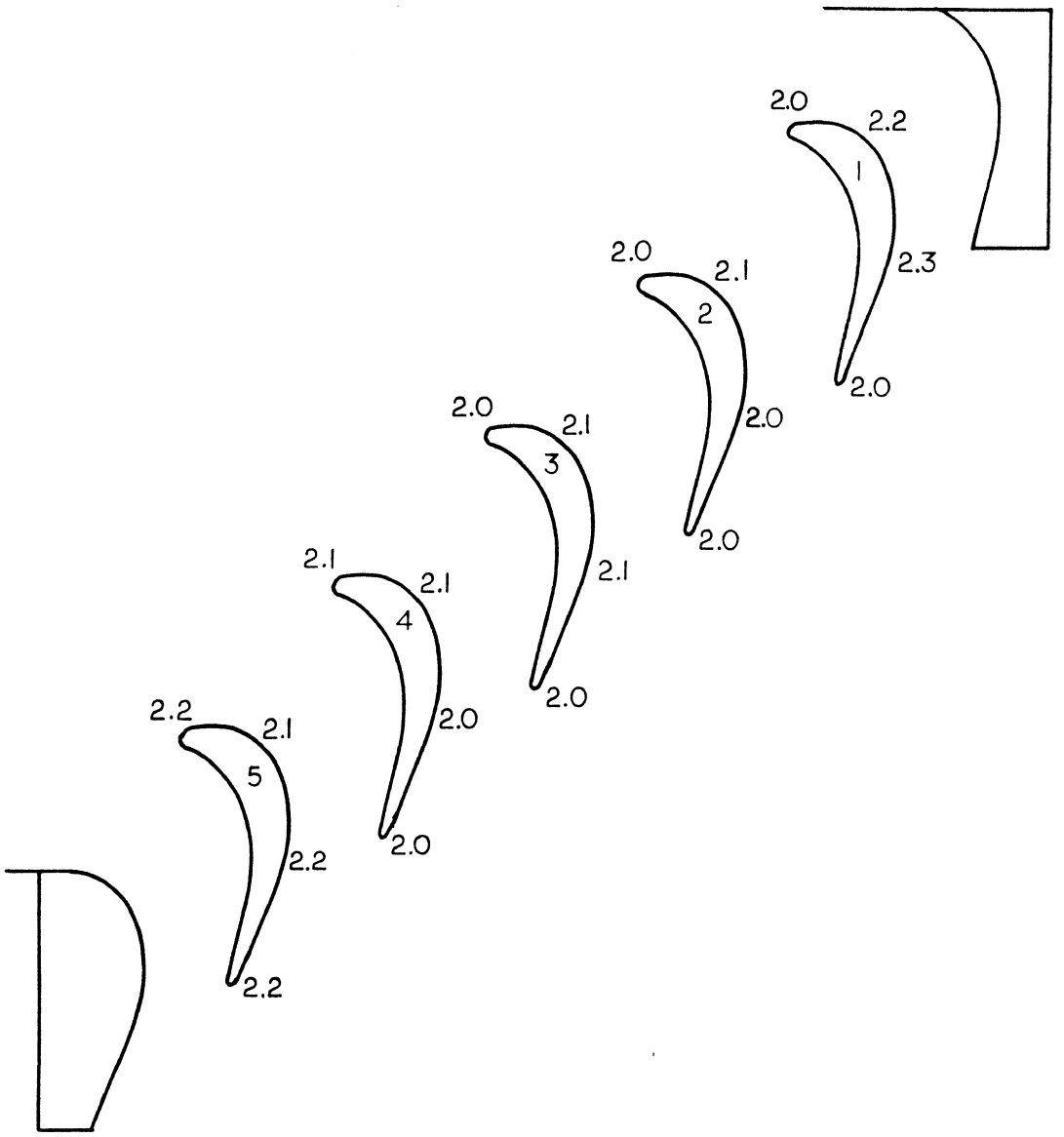

Fig. 10 Tip Gap Variation Across Blade Row, Percent of Blade Height.

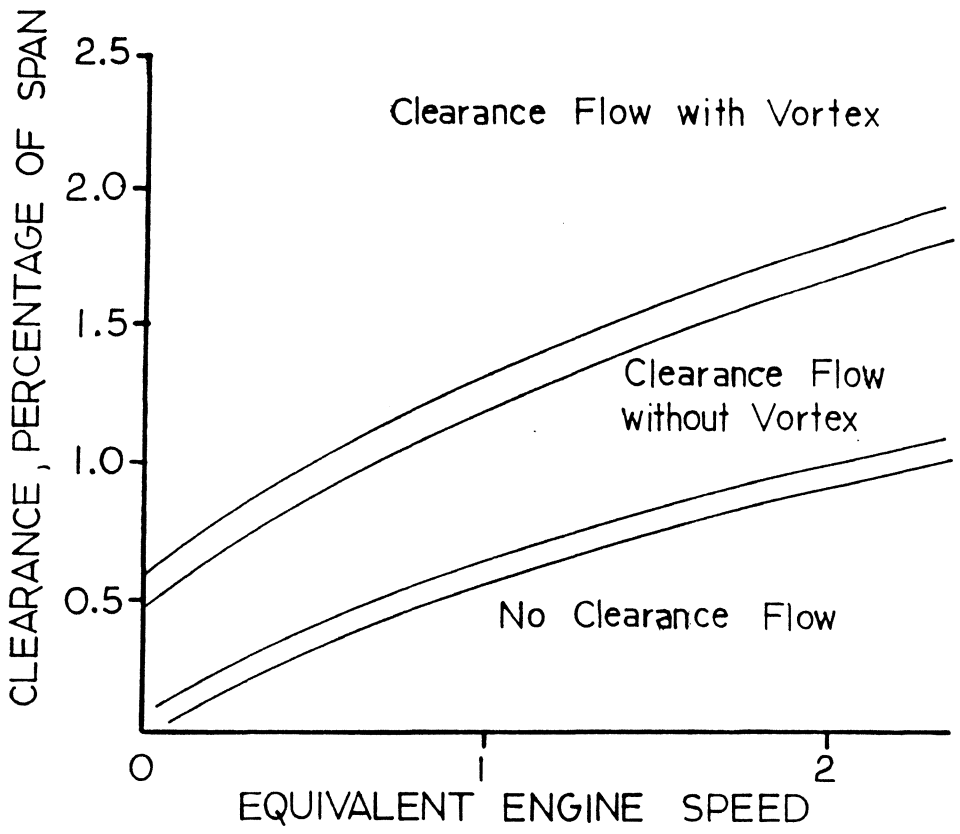

Fig. 11 Clearance Vortex Flow Regimes (after Graham [13]).

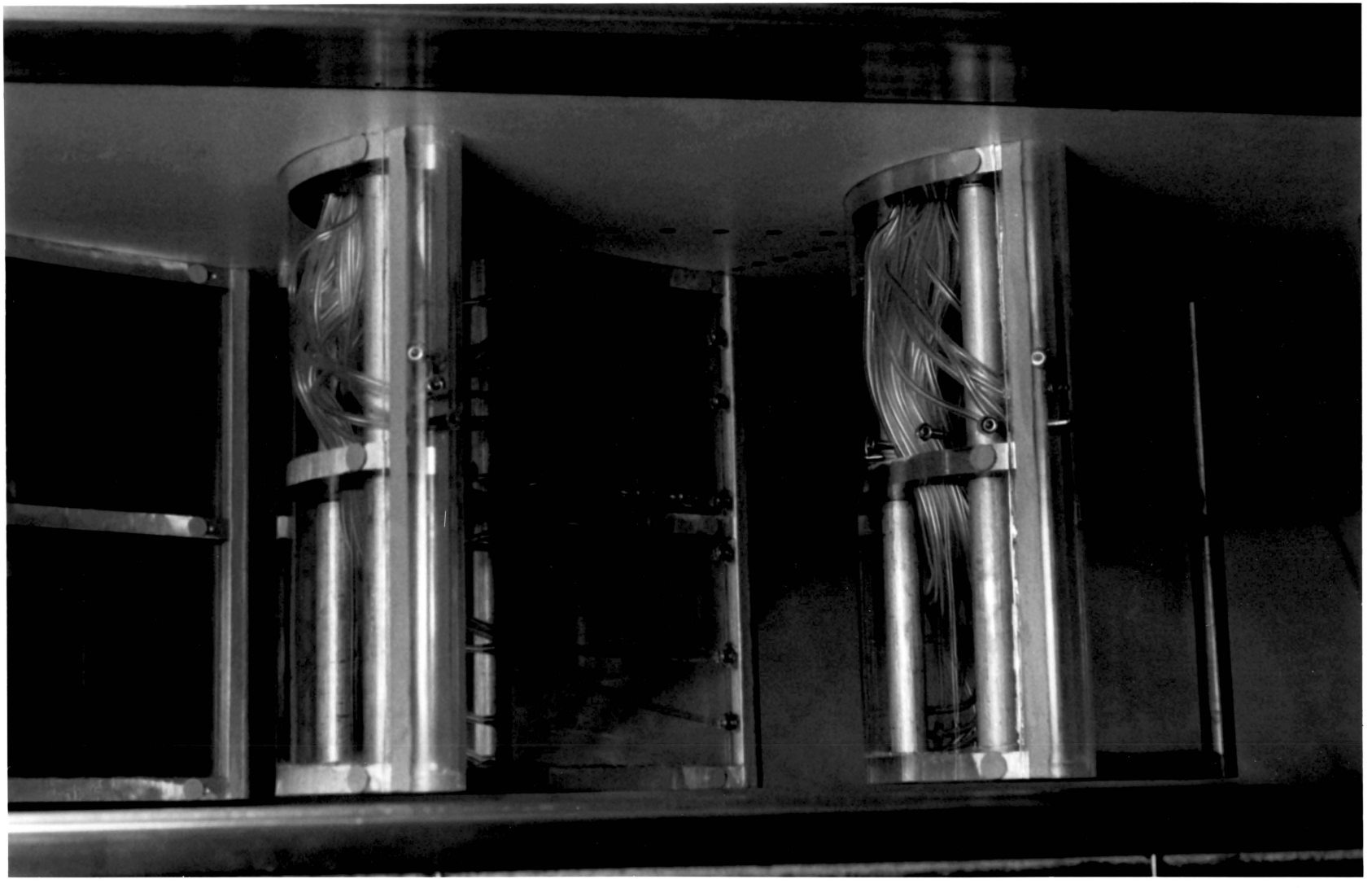

Fig. 12 Upstream View of Blade Passage and Tip Gap.

boundary layer thickness below that of the tip clearance gap, $\delta_t/\Delta z$ = 0.021.

Figure 13 shows a top view of the cascade test section, with the cross-sectional view A-A given in Fig. 14. An actual view looking along the row, in the opposite direction, from B-B, is shown in Fig. 15.

With the blade row and wind tunnel dimensions set, the height of the wind tunnel through the test section needed to decrease from 0.3 m to 0.24 m. This allowed for the bleeds on the top and bottom endwalls to be each 30 mm in height.

The two bleed pieces were constructed of 19 mm thick aluminum, 76 mm wide. The leading edges were chamfered on a milling machine to produce the shape shown in Fig. 16. The chamfer was selected to reduce the possibility of flow separation occurring over the leading edge of the bleed pieces. Due to the chamfer used, the distance from the leading edge of the chamfer to the endwall was 25.4 mm.

A 0.51 mm diamter trip wire was epoxied on the tunnel side of the chamfer on each of the two aluminum bleed pieces, approximately 9.5 mm downstream of the leading edges, as shown in Fig. 16. The trip wire assisted the establishment of a uniform turbulent endwall boundary layer entering the blade row.

The plenum chambers for the endwall bleeds were built from 3 mm aluminum. They were made to be as identical as possible, to produce uniform effects on the flow. Each plenum chamber had a base consisting of two pieces, see Fig. 14, both secured to the wind tunnel. Attached to these pieces was bolted a plenum cover. The top plenum cover was bolted through slots, allowing for adjustments in the height of the wind tunnel or the test section.

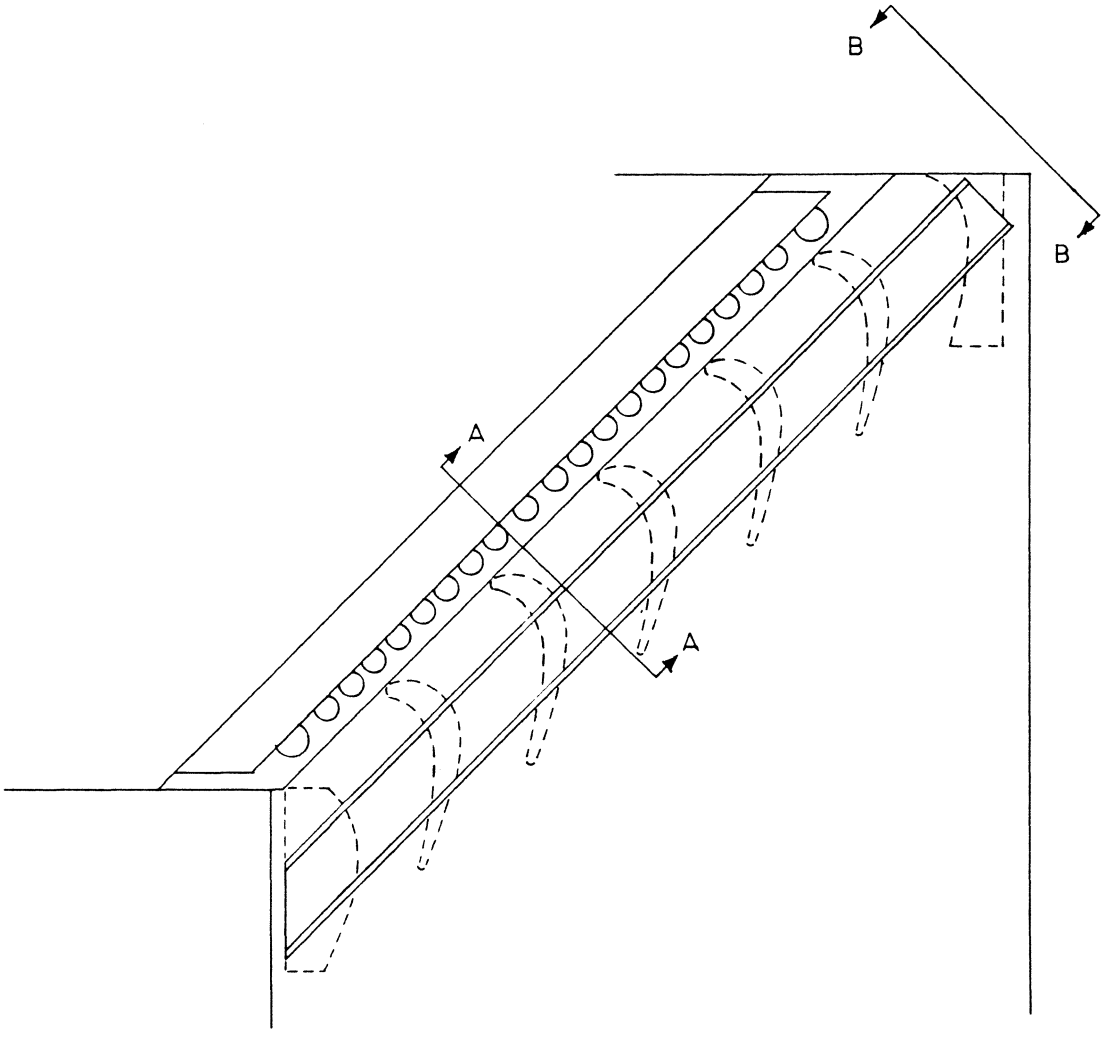

Fig. 13 Top View of Cascade Test Section

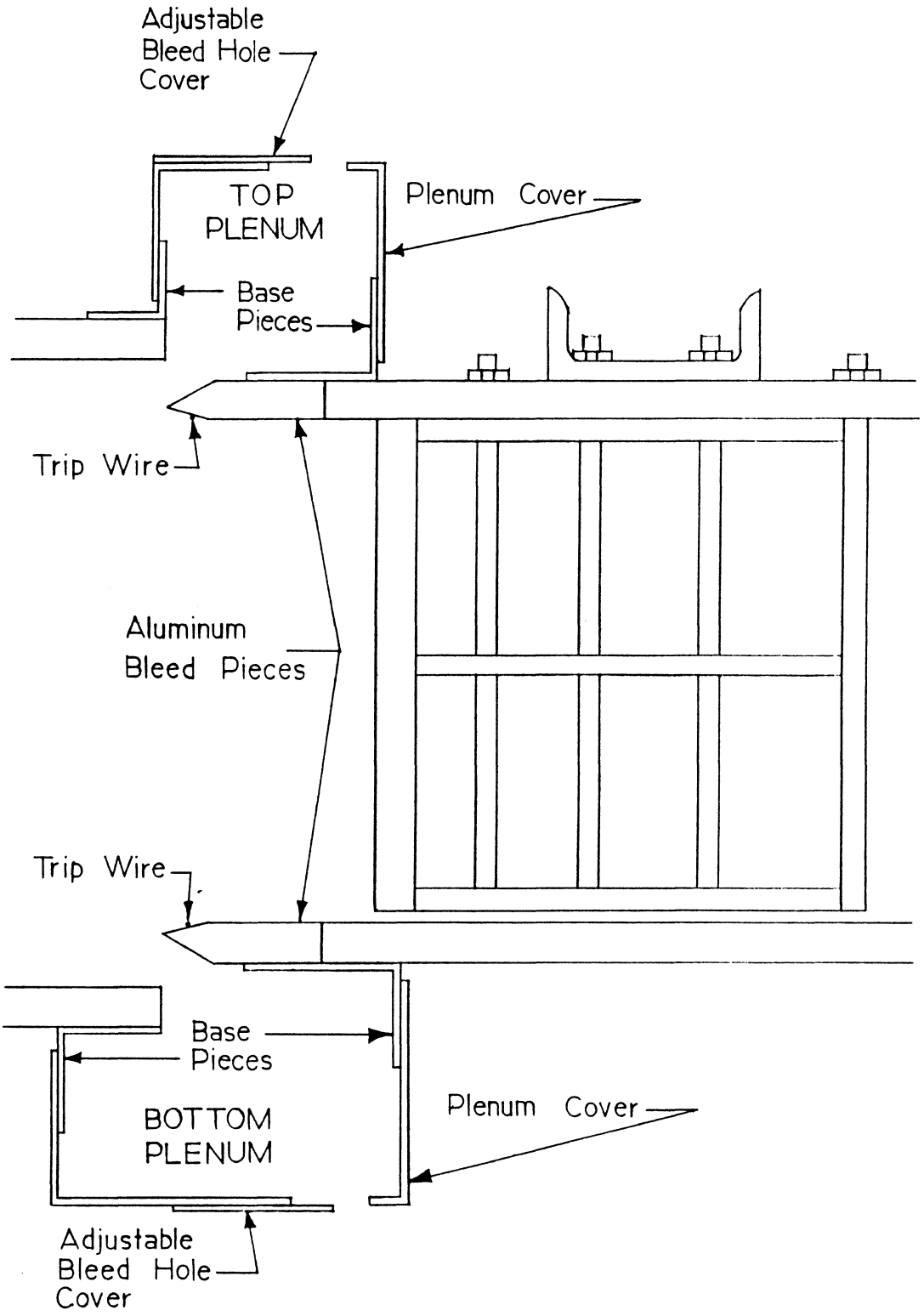

Fig. 14 View A-A of Cascade Test Section (refer to Fig. 13).

Fig. 15 View B-B of Cascade Test Section (refer to Fig. 13).

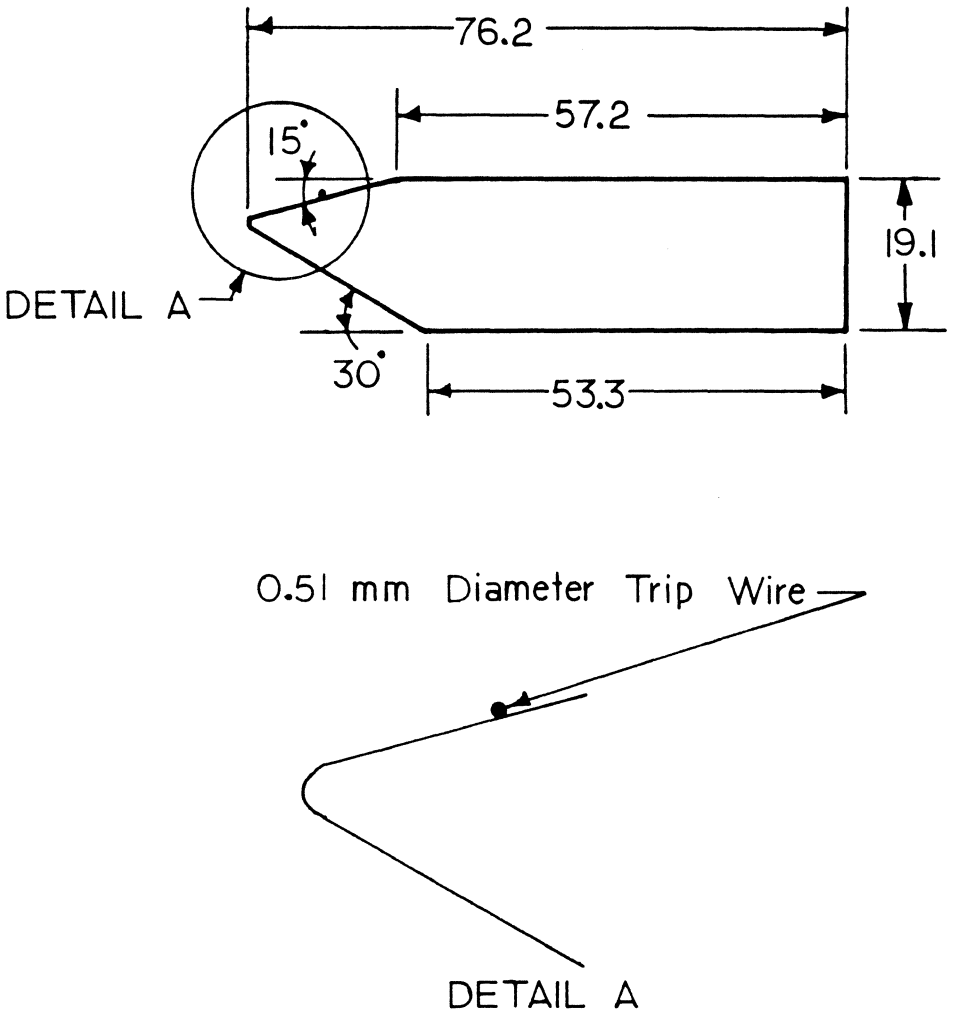

Fig. 16 Dimensions of Aluminum Bleed Piece (all linear dimensions in mm).

The air flow left the plenums through a series of bleed holes as shown for the top plenum in Fig. 17. These holes, symmetrically located around the blade positions to produce similar flow, were sized to have the same pressure drop as flow through the blade cascade. To obtain this sizing, the endwall boundary layer thickness, at the leading edge of the bleed, upstream of the middle blade was calculated, assuming the boundary layer was tripped turbulent on a wooden bar located inside the contraction of the wind tunnel. The size of the boundary layer was calculated as 24.2 mm, while the bleed gap was 25.4 mm; hence, for simplicity, the boundary layer was assumed to fill the bleed gap. Thus the average velocity of the flow through the bleed gap was taken as approximately 85 percent of the freestream velocity. The throat of the blade cascade had an area reduction of approximately 35 percent, therefore so must the bleed holes to have the same pressure drop. Also important, sharp edge orifices, like our bleed holes, have discharge coefficients of 0.6, which increased the size required. Finally, the area of the holes was further enlarged by 15 percent to provide a margin of safety.

Outside of, and bolted to, the plenums were sliding bleed hole covers which could be adjusted to change the area of the bleed holes, as can be seen in Fig. 17. These bleed hole covers were used with the two wooden bleeds to provide and maintain flow repeatability.

F. Measuring Equipment

A 32 tubed inclined manometer was used for obtaining flow repeatability. To prepare the manometer, the glass tubes were cleaned,

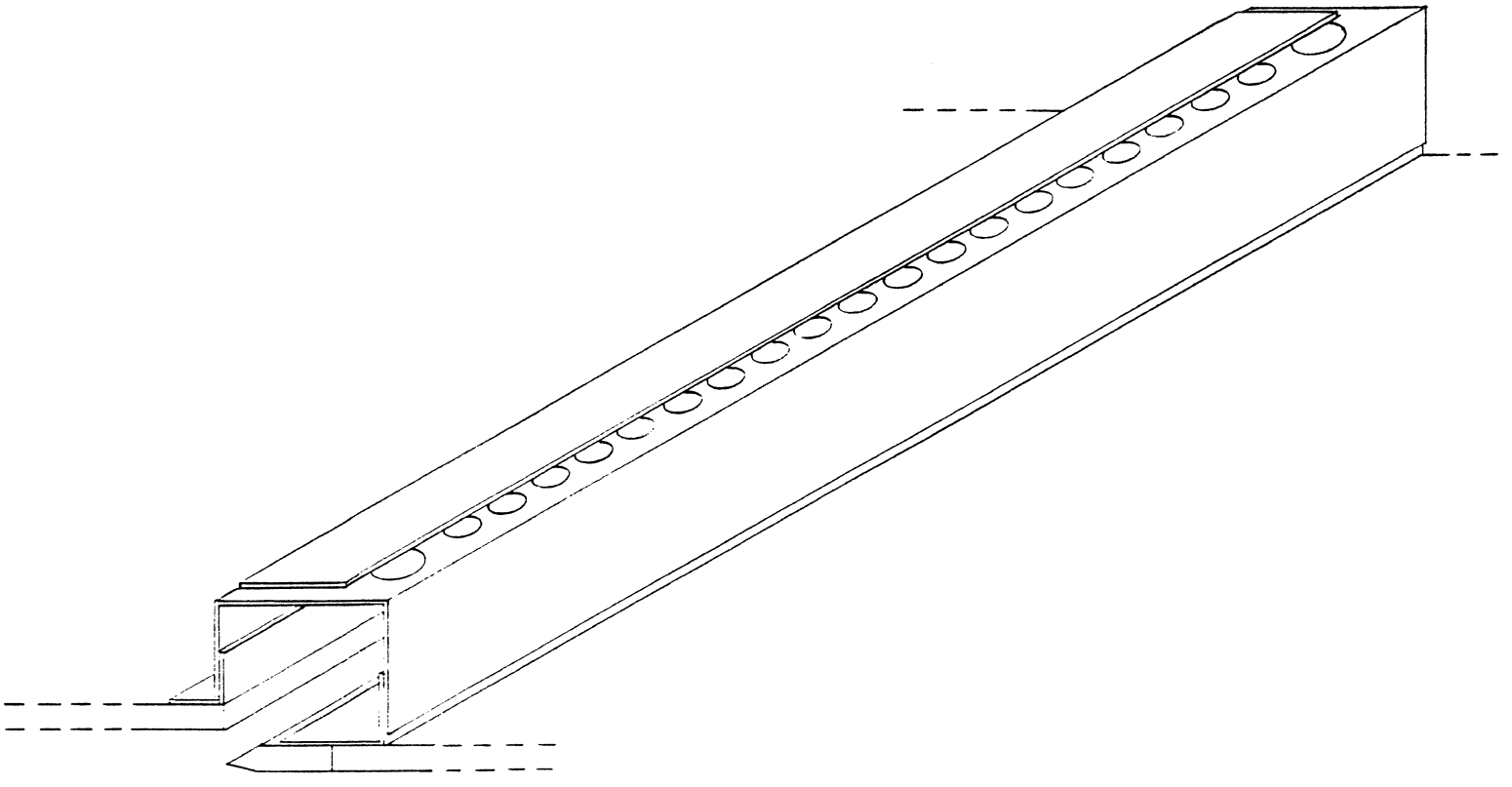

Fig. 17 Isometric View of Top Plenum

the table was leveled, and the manometer was inclined at 18° to the horizontal. The measuring fluid was red Meriam oil with a specific gravity of 0.826. The estimated uncertainty of the manometer readings was ± 1.3 mm, which converts to ± 3.2 Pa.

Two pitot probes, both constructed for this study, were used, see Fig. 18. Both probes had flattened tips to provide more accurate total pressure readings. The thickness of the probe tips was 0.53 mm.

Probe A was used to determine the inlet endwall boundary layer thickness. Probe B was used to measure velocities of the exit tip gap flow. Probe B was constructed so it would be offset upstream from the corresponding reference wall static pressure tapping by approximately 6.4 mm, as shown in Fig. 19.

A simple one-dimensional traversing gear arrangement was used with the pitot probes. The threaded rod in the traversing gear had 20 threads per 25.4 mm. A dial gauge, readable to ± 0.01 mm, was used to position the probes. Set to a zero reading when the probe was at the wall, the dial guage was adjusted by hand to move the probes in the tunnel.

Pressure readings were converted into electrical signals by a Statham pressure transducer (± 0.3 PSID, serial number 12251). The transducer signals were amplified in a BA-13 bridge amplifier (Vishay Instruments, Inc.). The output was then sent through a Type 3A74 preamplifier (Tektronix) and monitored on a Type 561A oscilloscope (Tektronix).

An inclined manometer (Meriam Model A-434) was used to calibrate the pressure transducer.

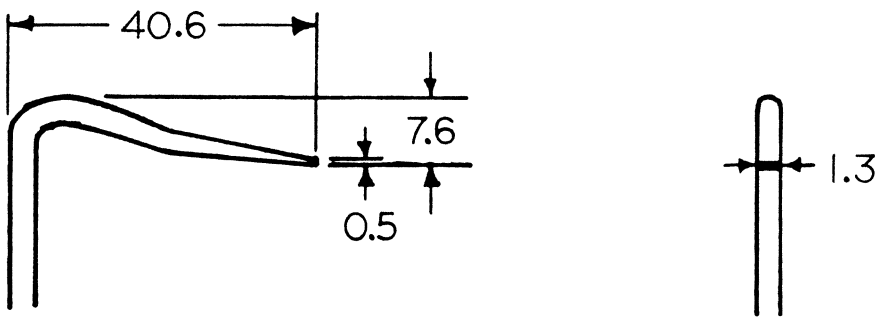

PROBE A

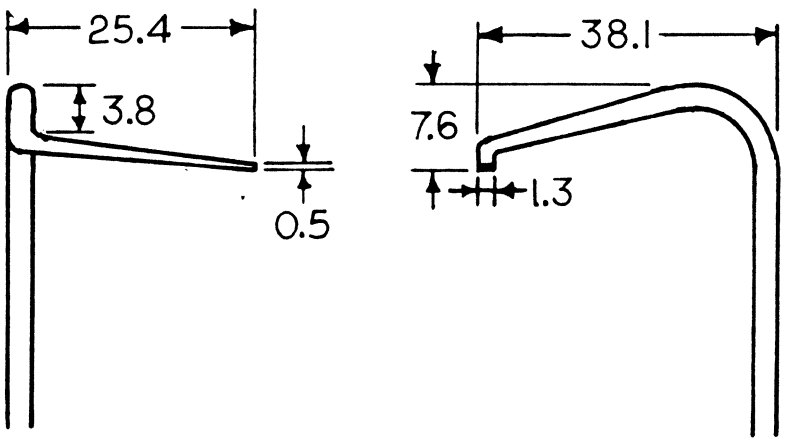

PROBE B

Fig. 18 Pitot Probes Used for Upstream Endwall Boundary Layer and Tip Gap Exit Velocity Profiles (all dimensions in mm).

Fig. 19 Pitot Probe B at Tip Gap Exit.

IV. FLOW VISUALIZATION

Flow visualization tests were performed to study the flow pattern on the tip gap endwall and on the suction surface of blade 3.

Ten grams of titanium dioxide (T_iO_2) were filtered through a 0.25 mm screen and mixed with 40 ml of diesel fuel and 2 drops of oleic acid. For the end wall, the visualization was performed on a 8.02 mm thick sheet of aluminum, and on the blade, a 0.09 mm thick sheet of Mylar was used. The aluminum and the Mylar were sprayed with Krylon Ultra-Flat Black Enamel (1602), which was allowed to dry. The flow visualization mixture was then painted on the surfaces. The aluminum sheet was laid on the bottom endwall and fixed in position with tape. The Mylar was also attached to the suction surface of the middle blade with tape.

The wind tunnel was run until the mixture was dry, and the visualization was then fixed with Krylon Crystal Clear (1301) Acrylic Spray Coating.

A. Endwall Surface Flow Visualization

The endwall surface flow visualization is presented in Fig. 20, with a closeup of blades 2, 3, and 4 in Fig. 21. A schematic of the visualization around blade 3 is given in Fig. 22.

At the endwall, the turbulent inlet boundary layer appears to split at point A, along lines L1 and L2. This flow approaching the blade leading edge, instead of rolling into a horseshoe vortex, as is common in a blade row with no tip gap, flows either under the tip clearance to the suction side of the blade, or across the passage as a secondary flow

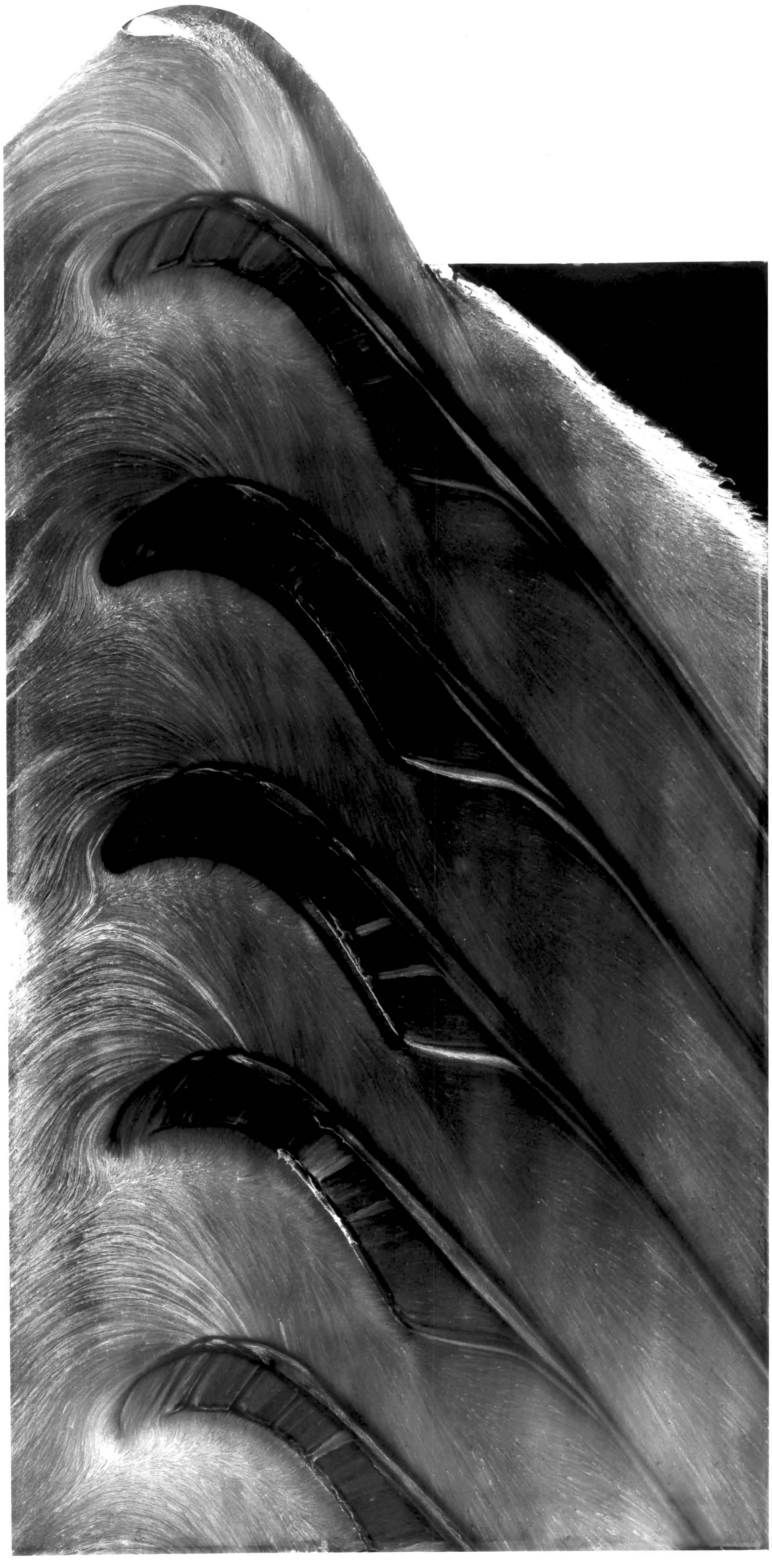

Fig. 20 Bottom Endwall Flow Visualization.

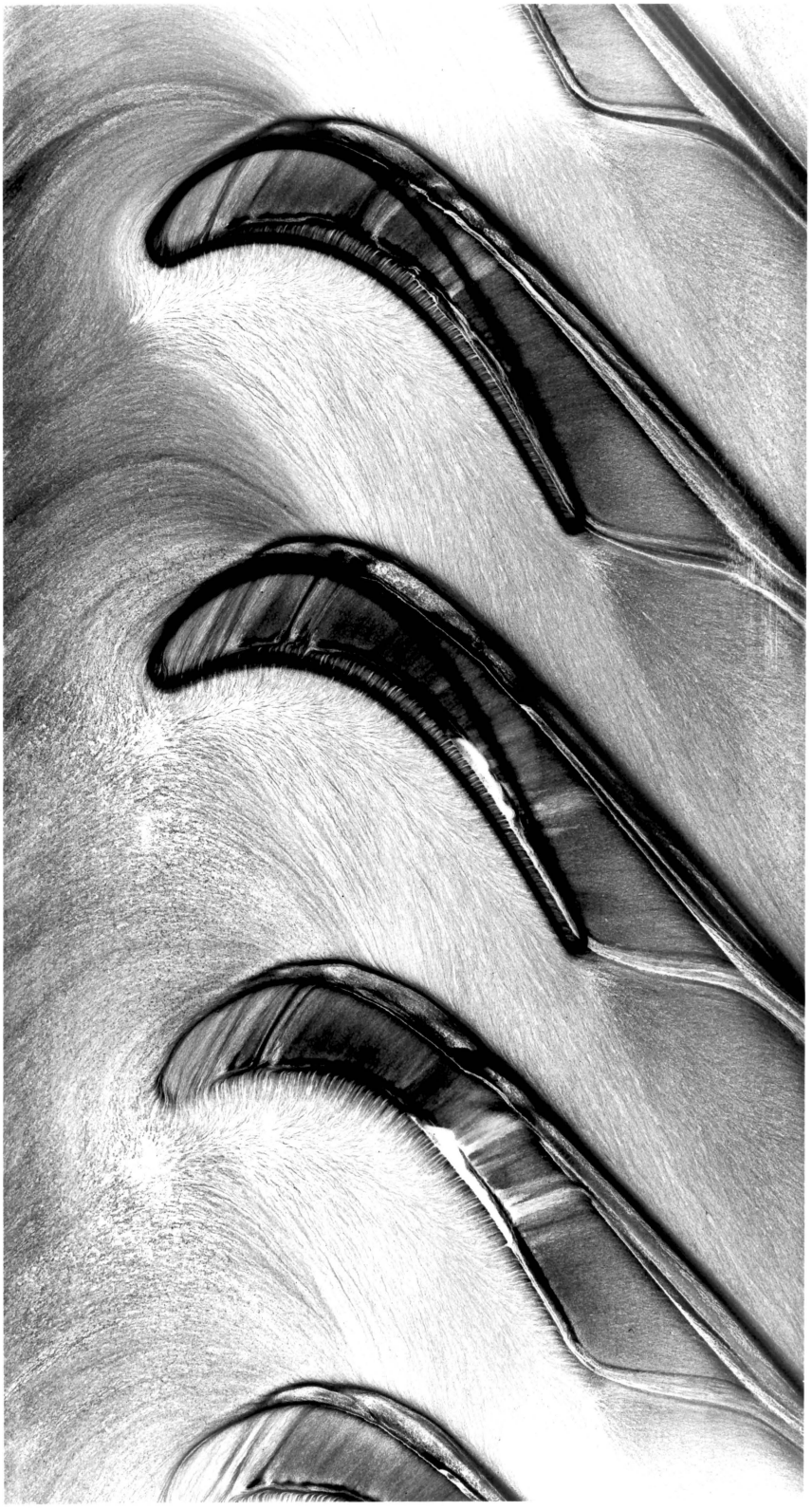

Fig. 21 Closeup of Endwall Flow Visualization.

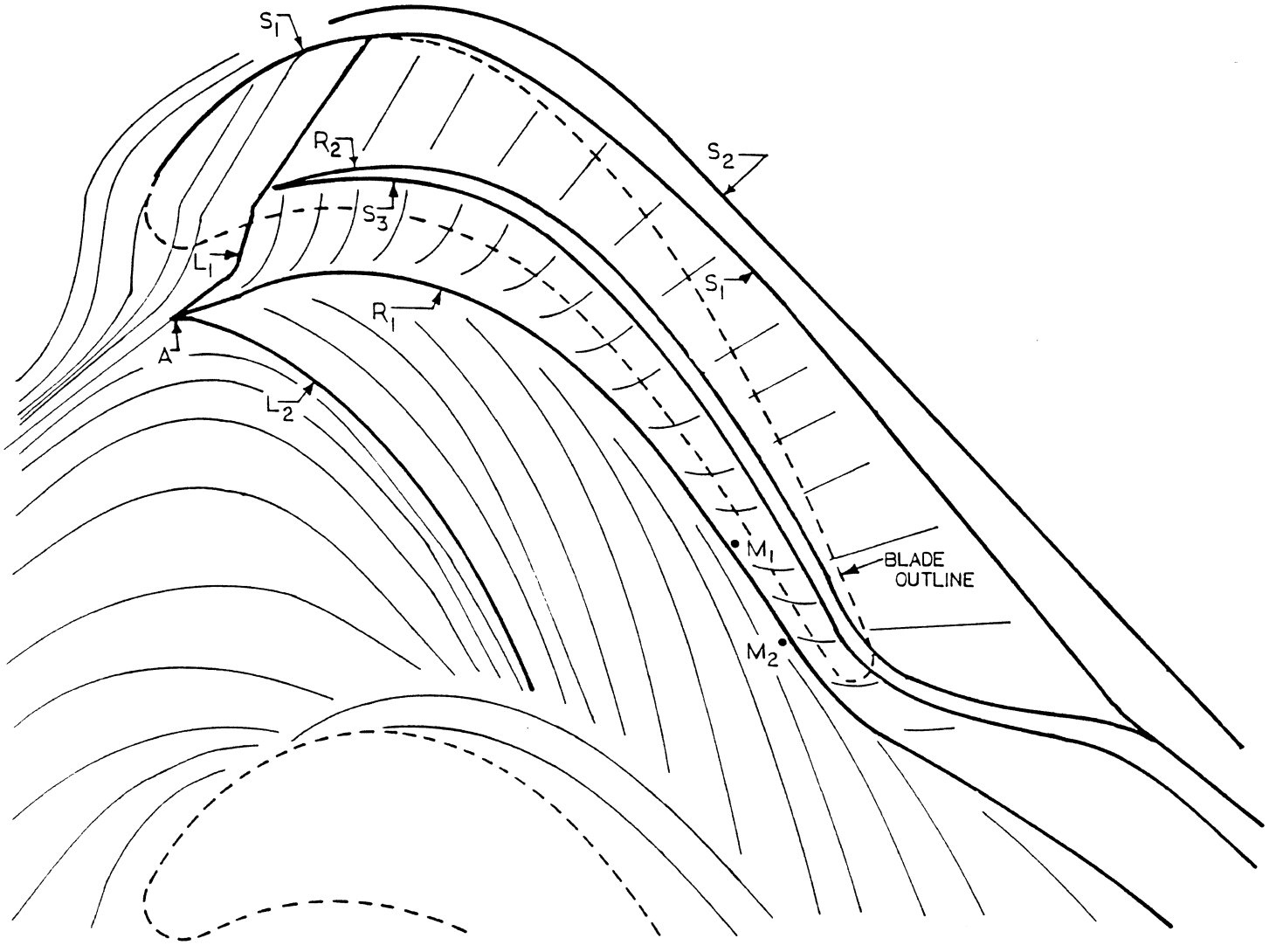

Fig. 22 Schematic of Endwall Flow Visualization

towards the suction side of the next blade. Upstream of L1, this flow stays attached under the blade until it separates along S1, when it encounters the flow in the passage on the suction side of the blade. Here, S1 lies under the blade outline; it continues downstream, moving out into the flow passage as the tip leakage flow penetrates into the flow path.

The tip leakage flow separates along line S1 and secondary flow moving from the pressure side of the passage to the suction side of the passage separates along line S2 as they meet. Flow in the region between S1 and S2 appears to be quite three-dimensional and is difficult to interpret.

Downstream of L1, running the remaining length of the blade, lie a separation line and a reattachment line, S3 and R2, respectively. As will be discussed in section V.B, this seems to be a laminar boundary layer separation followed by a turbulent boundary layer reattachment. This laminar boundary layer could be created in the blade passage after the inlet turbulent boundary layer is convected away, and might be caused by inviscid freestream flow then flowing down towards the endwall. This inviscid flow seems to attach as a laminar flow along R1 and then accelerate away from this line in a divergent flow pattern. This is confirmed by static pressure measurements along two planes of the blade passage which show pressure maxima at the marked points M_1 and M_2. Belik [15] and Senoo [16] are apparently the only ones to validate this laminar endwall boundary layer hypothesis in a turbine cascade [7]. Our results, indicating laminar separation of the endwall boundary layer beneath the blades constitutes a third observation of this behavior.

The tip leakage vortex dissipates downstream, as is suggested by S1 and R2 merging. The flow continues to separate along S3 and S2 as the two passage flows mix together.

B. Suction Surface Flow Visualization

The suction surface blade flow visualization is presented in Fig. 23. A tip leakage vortex is seen along the bottom of the blade, growing larger as the trailing edge is approached, steadily displacing the small passage vortex upward towards midspan. Near the bottom trailing edge of the blade, a small mixing seems to occur in the tip leakage vortex. Evidence of a passage vortex is also seen in the top half of the passage, where there is no tip gap.

C. Wool Tuft Flow Visualization

A metal probe, with a piece of wool attached to the tip, was inserted into the flow at the blade throat. The results of this test are shown in a schematic of the flow behavior in Fig. 24. The passage vortex above the tip gap leakage vortex was very weak and barely detectable with the wool tuft.

Fig. 23 Suction Surface Flow Visualization.

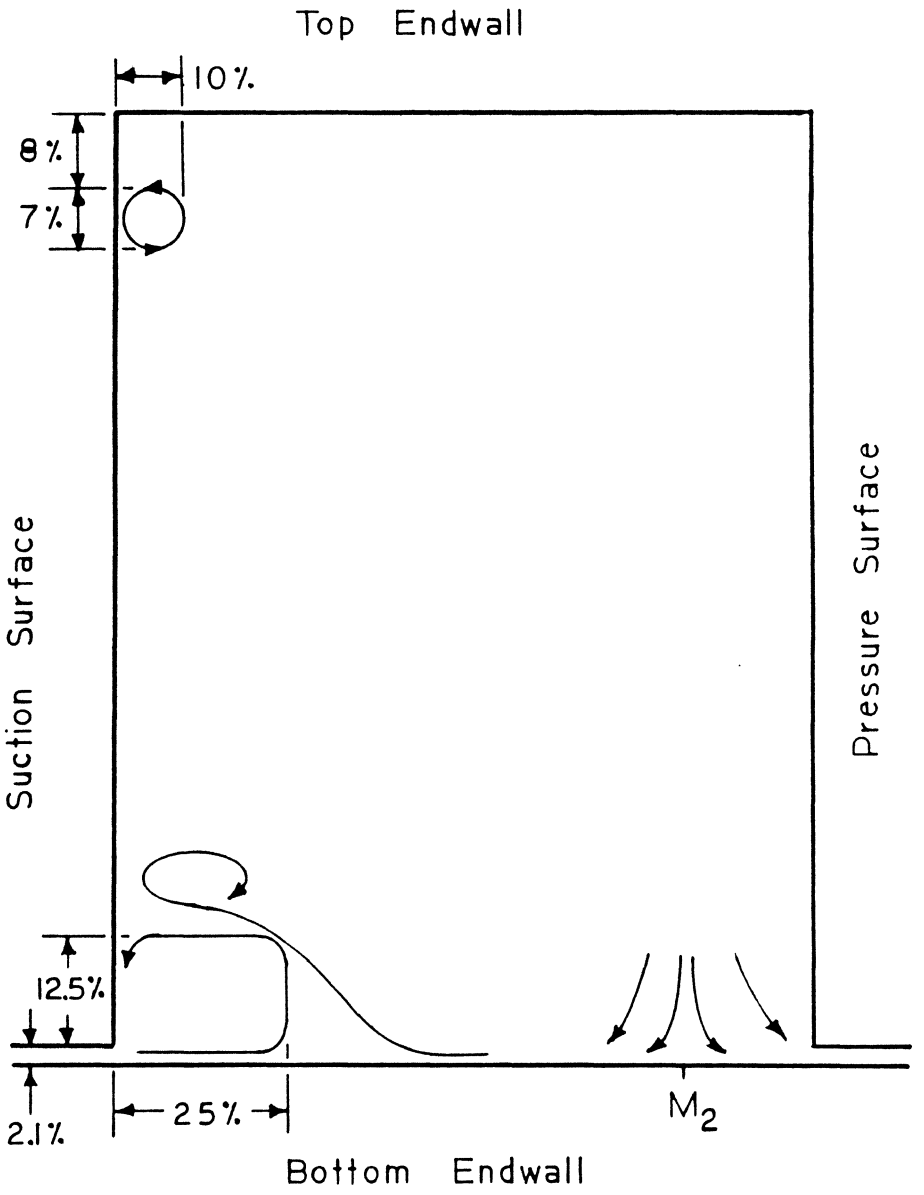

Fig. 24 Tentative Flow Behavior in the Blade Passage Throat, (Figure Indicates Approximate Spanwise and Blade-to-Blade Locations).

V. PRESSURE MEASUREMENTS

A. Locations of Pressure Measurements

1. Static Pressure Tappings

In order to study the tip leakage flow, the middle blade was instrumented with static pressure tappings on the pressure side, and on the bottom surface. The adjacent blade had tappings on the pressure side only. Also, the endwalls had tappings in the passage between the two blades and under the bottom of the middle blade.

The static pressure measurements on the middle blade allowed its performance as an airfoil to be measured. The static pressure measurements on the suction surface of the middle blade, the pressure surface of the adjacent blade, and the endwalls, indicated the performance of the passage between the blades. The static pressure measurements under the blade gave information about the development of the tip leakage flow.

Static pressure tappings were placed upstream of blades 2, 3, and 4 on the endwalls to measure the upstream static pressure. The three-dimensional viscous flow calculations of Moore and Moore [5] showed a static pressure contour extending approximately straight upstream from the leading edges of the blades, with a value corresponding to the upstream static pressure, see Fig. 25. This contour appeared to intersect the blade close to the location of the camber line at the leading edge. Similar behavior is observed in the two-dimensional inviscid flow calculations of Langston, et al. [3] and Graziani, et al. [6]. Hence, the tappings were positioned 77.4 mm upstream (1/3 of an axial chord) along this contour line.

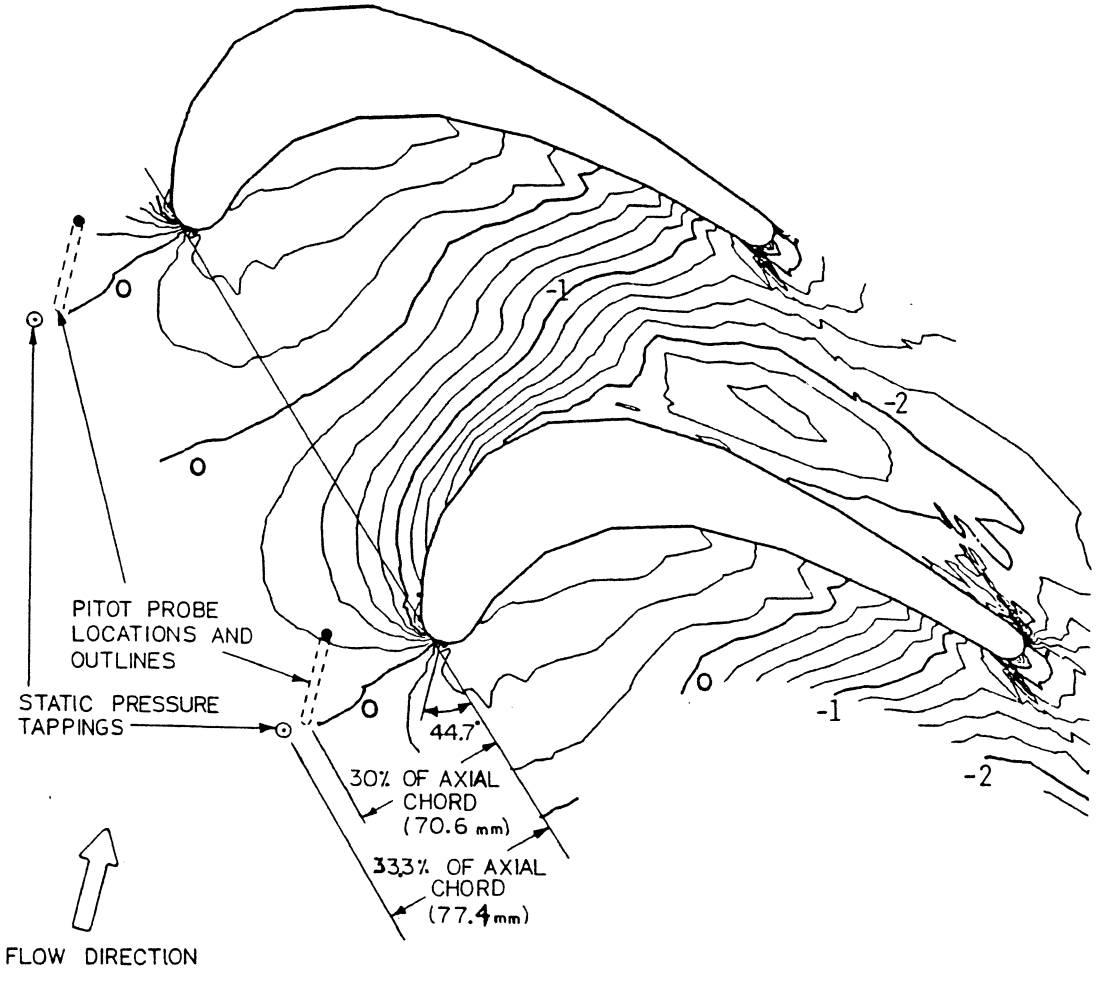

Fig. 25 Static Pressure Coefficients Around Langston, et al. Turbine Blade (after Moore and Moore [5]).

The axial locations of the planes used to locate the static pressure tappings are shown in Fig. 26. These planes closely correspond to the measurement planes used by Moore and Ransmayr [17] and Langston, et al. [3].

Rains [10] concluded that tip leakage flow can be assumed to flow perpendicular to the camber line of the blade. Hence, for flow entering the tip gap at plane 6a, at 60 percent of an axial chord, it would be assumed to exit at plane 7aa, at 72.3 percent of an axial chord. For this reason, plane 7aa, which was not used by Moore and Ransmayr, was utilized in this study.

Both sides of blade 3, the middle blade, were instrumented at 45 percent span, giving a picture of the blade loading at approximately midspan, to compare with Moore and Ransmayr's earlier results [17].

Heavily instrumenting the plane 6a, in the spanwise direction, on the pressure surfaces of both blades 2 and 3, fulfilled two purposes. It provided a measurement of the blade unloading as the tip gap was approached. Also, the flow behavior between blades 2 and 3 along plane 6a-6a was to be studied. Instrumenting the pressure surface of blade 2 at plane 6a, along with the suction surface of blade 3 at plane 6a, and plane 6a of both endwalls between blades 2 and 3, placed static pressure tappings all around the blade passage at this plane.

The throat of the passage between blades 2 and 3 , plane 6a-8b, was also studied. Static pressure tappings were placed on the pressure surface of blade 2 at plane 8b, plane 6a-8b of both endwalls, and again, the suction surface of blade 3 at plane 6a, to instrument this plane of the passage.

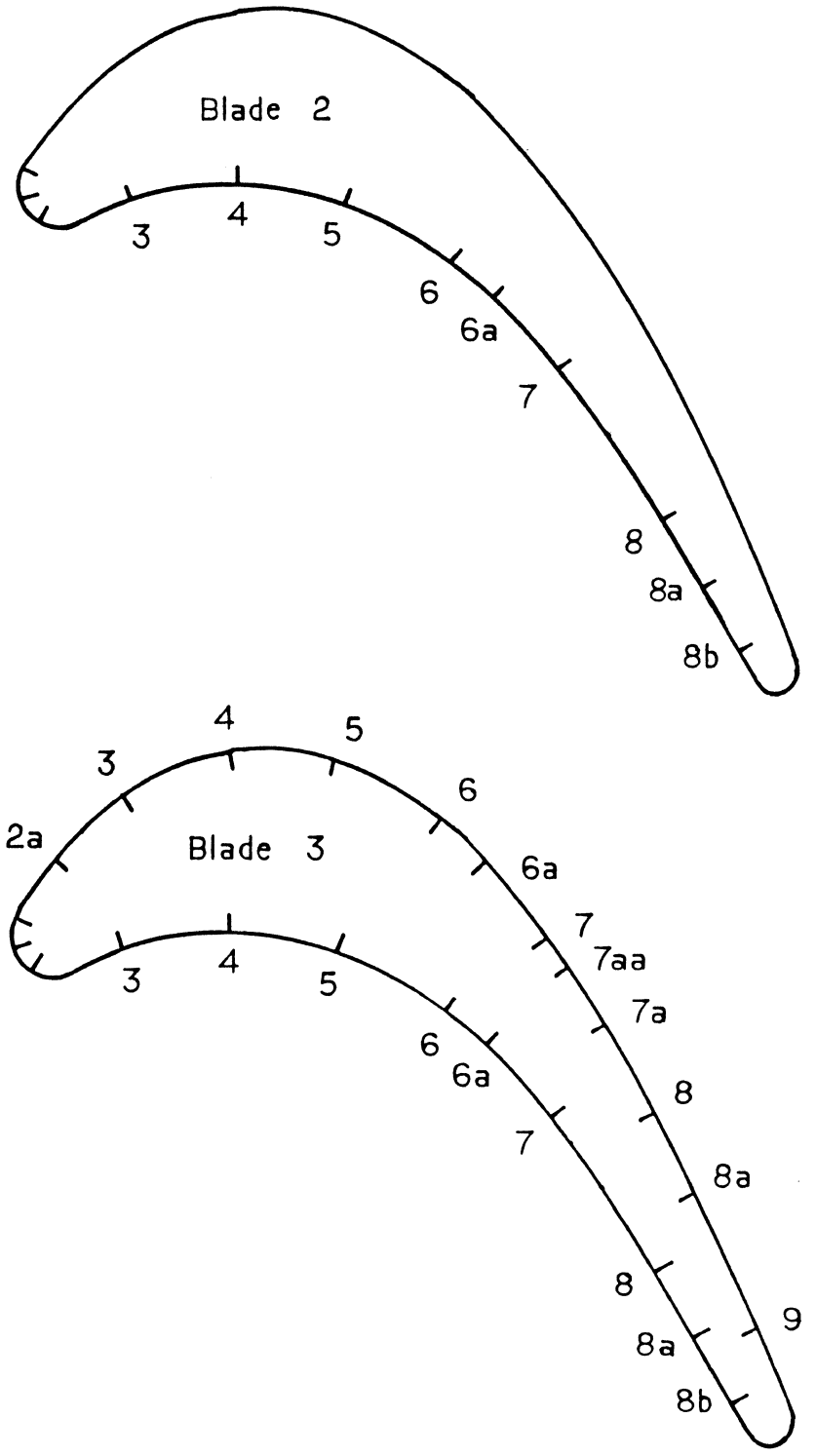

Fig. 26 Measurement Planes on the Blade Row.

A complete listing of the static pressure tapping locations for blade 3 is given in Table 1, and for blade 2 is given in Table 2.

Table 1 also contains the pressure tapping locations on the bottom of blade 3, along the top side of the tip gap. These locations are shown in Fig. 27. Again, plane 6a-7aa is approximately perpendicular to the blade camber line, corresponding to the path of the flow if it entered the tip gap at plane 6a. Plane 6a-6a was instrumented on the bottom of the blade to provide data to compare with future computational results.

Figure 28 shows the locations of the static pressure tappings on the top endwall. Plane 6a-6a, at 60 percent of an axial chord was instrumented. Also instrumented was the throat of the passage between blades 2 and 3, plane 6a-8b.

The bottom endwall was similarly instrumented, with additional tappings under the tip gap of blade 3, refer to Fig. 29. These pressure tappings, along with the pressure tappings on the bottom of blade 3, gave a picture of the development of the tip gap leakage flow along planes 6a-6a and 6a-7aa.

The tappings on the endwalls were 1.02 mm diameter holes drilled in 6.35 mm diameter brass rods. An exception to this is a series of tappings near the pressure surface of blade 3, which were drilled in a rotatable Plexiglas plug to provide closer readings and more definition of the pressure distribution at the entrance to the tip gap.

Finally, all five round leading edges were instrumented with three static pressure tappings. Figure 28 shows the exact angular locations. The pressure tapping 10° towards the pressure surface from

Table 1. Location of Static Pressure Tappings on the Middle Blade, Blade 3

(i) Pressure Surface:

Plane	Axial Distance[1] mm	% Span[2]
3	33.9	45
4	65.7	45
5	97.6	45
6	129.6	45
6a	141.1	87.5,75,55,45,25,12.5
7	161.3	45
8	193.1	45
8a	205.7	45
8b	215.9	45

(ii) Suction Surface:

Plane	Axial Distance[1] mm	% Span[2]
2a	12.7	45
3	33.9	45
4	65.7	45
5	97.6	45
6	129.6	45
6a	141.1	97.5,95,92,87.5,75,55, 45,25,12.5,8,5,2.5
7	161.3	45
7a	177.8	45
8	193.1	45
8a	205.7	45
9	225.1	45

Table 1 (continued)

(ii) Bottom Surface:

Plane	Axial Distance[3] mm	% Blade Width[4]
6a-6a	2.5	4.4
6a-6a	9.1	16
6a-6a	17.3	30
6a-6a	28.5	50
6a-6a	36.8	65
6a-6a	45.5	80
6a-7aa	1.5	4.4
6a-7aa	6.7	20
6a-7aa	13.7	40
6a-7aa	20.7	60
6a-7aa	27.7	80

1) Measured from blade leading edge: axial chord = 235.2 mm
2) Measured from top endwall; span = 234.4 mm
3) Measured from pressure surface
4) Blade width for plane 6a-6a = 57.2 mm
   Blade width for plane 6a-7aa = 34.8 mm

Table 2. Locations of Static Pressure Tappings on Blade 2

Pressure Surface:

Plane	Axial Distance[1] mm	% Span[2]
3	33.9	45
4	65.7	45
5	97.6	45
6	129.6	45
6a	141.1	98.9,97,8,96.7,95.7,94.6, 87.5,75,55,45,25,12.5
7	161.3	45
8	193.1	45
8a	205.7	45
8b	215.9	87.5,75,55,45,25,12.5

1) Measured from blade leading edge; axial chord = 235.2 mm
2) Measured from top end wall; span = 234.4 mm

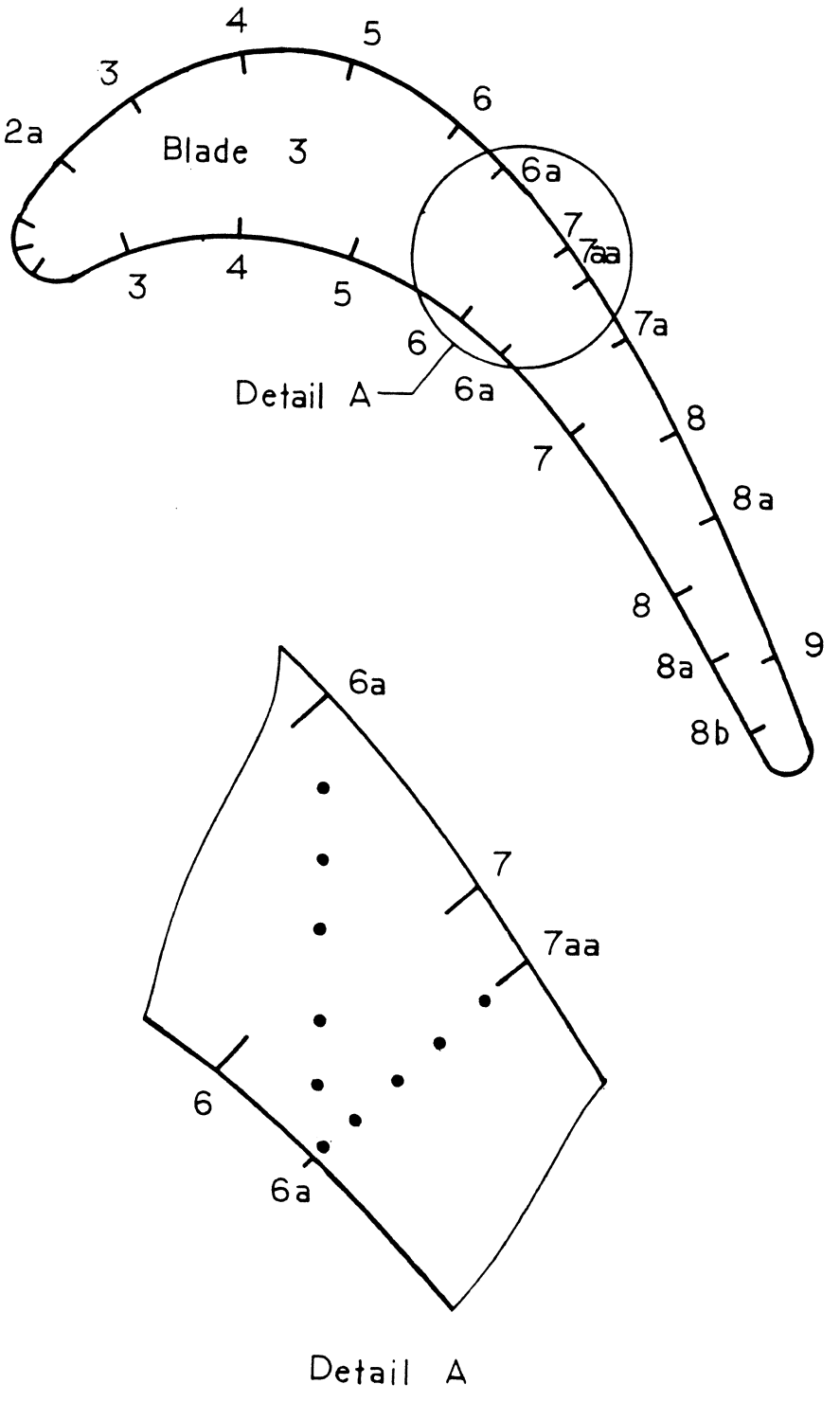

Fig. 27 Static Pressure Tapping Locations on Bottom of Blade 3.

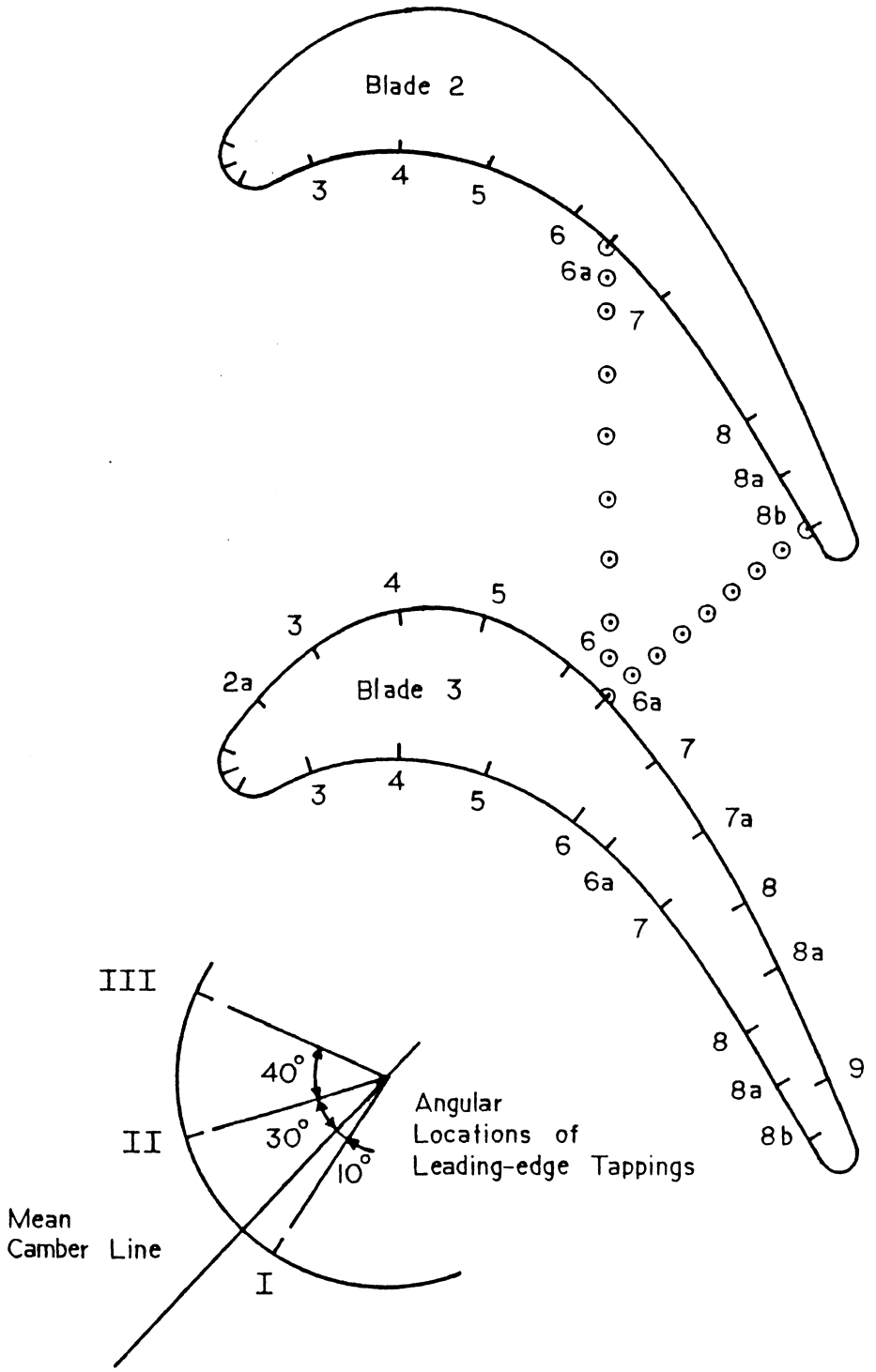

Fig. 28 Static Pressure Tapping Locations on Top Endwall and the Round Leading Edges of the Blades.

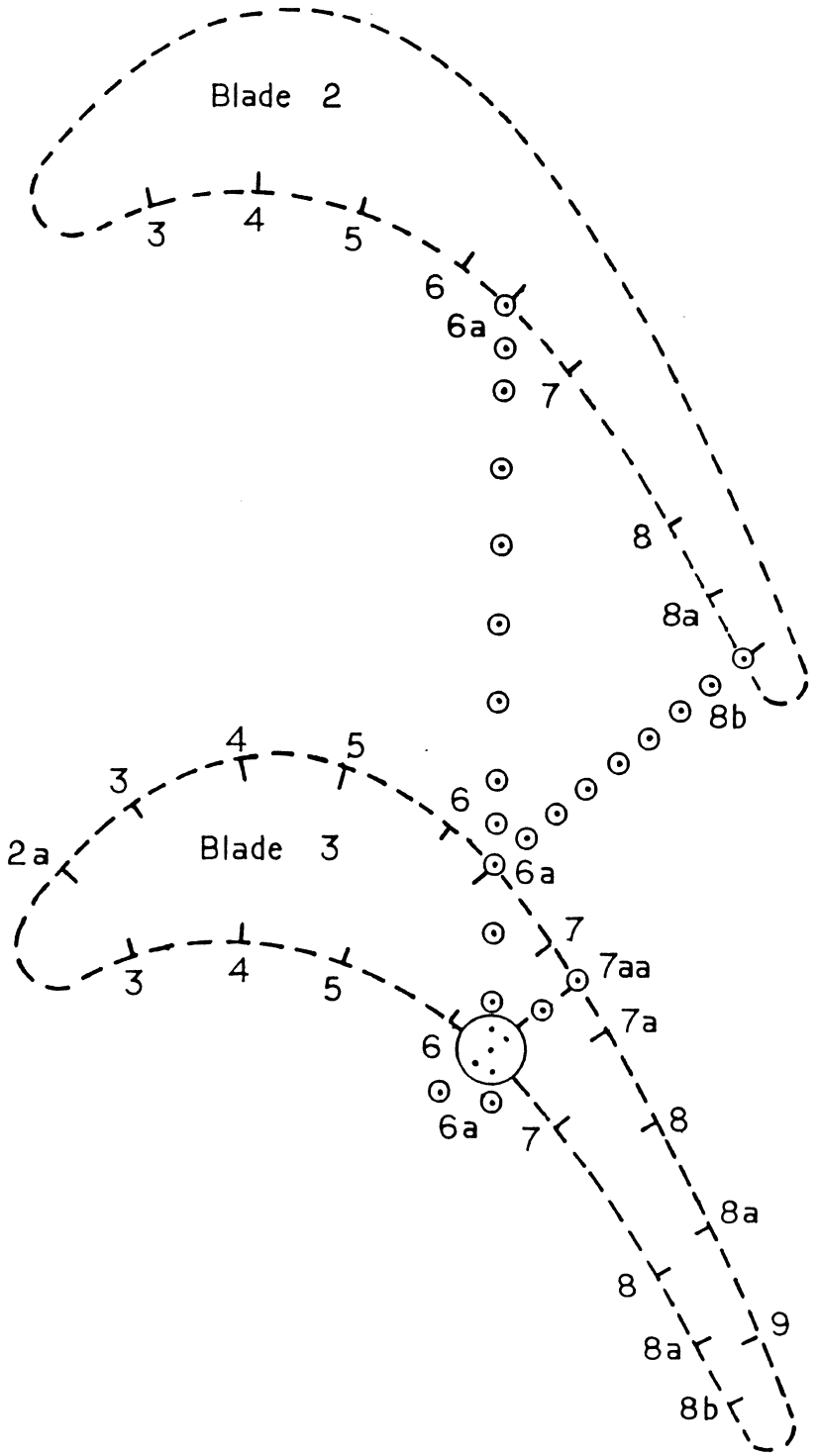

Fig. 29 Static Pressure Tapping Locations on Bottom Endwall.

the mean camber line is at 45 percent span from the upper wall, and located close to the stagnation point. The tapping at 40° and 80° from the first tapping were at 40 percent and 35 percent span, respectively. The cylindrical leading edge tube could be rotated about its axis to adjust the angular position of the static pressure tappings. The tubes were positioned during the blade assembly using a template.

2. Pitot Probe Locations

Pitot probe measurements were used to obtain information concerning the upstream endwall boundary layers and the velocity distribution at the exit of the tip gap. The boundary layers were traversed 30 percent of an axial chord upstream of the leading edges of blades 2, 3, and 4, on both endwalls. The probe was positioned so that the probe tip was located on the same pressure contour as the upstream static pressure tappings, but just downstream of these tappings, refer to Fig. 25.

The tip gap exit velocity profile was measured at two locations, marked D and E in Fig. 5. The upstream position, D, and the downstream position, E, were located so the probe tip was 6.4 mm upstream of the tip gap exit on planes 6a-6a and 6a-7aa, respectively. This was done so the probe tip would be close to the tip gap exit at planes 6a-6a and 6a-7aa, but not close enough to interfere with the readings of the static pressure tappings on these two planes.

B. Results and Discussion

The static pressure coefficient cp_s is defined as

$$cp_s = \frac{P_s - P_{so}}{\frac{1}{2} \rho U_o^2}$$

where

P_s = local static pressure

P_{so} = endwall static pressure upstream of blade 3

and

U_o = upstream freestream velocity.

1. Flow Conditions

The inlet freestream velocity was U_o = 20.1 m/s. The air density and viscosity were 1.11 kg/m^3 and 0.0000188 kg/ms respectively, at the standard test conditions of 94.9 kPa and 298 K. The Reynolds number based on the blade axial chord and an exit velocity of 32.3 m/s was 4.5 x 10^5.

2. Blade Leading Edges

Figure 30 gives a picture of the flow repeatability combined with the accuracy of the locations of the static pressure tappings on the round leading edges of the blade. The readings from each of the five blades at locations I, II, and III (see Fig. 28) are shown together for comparison. Using the apparent locations as a measure of the repeatability, the flow is seen to be repeatable within ± 1.7 degrees.

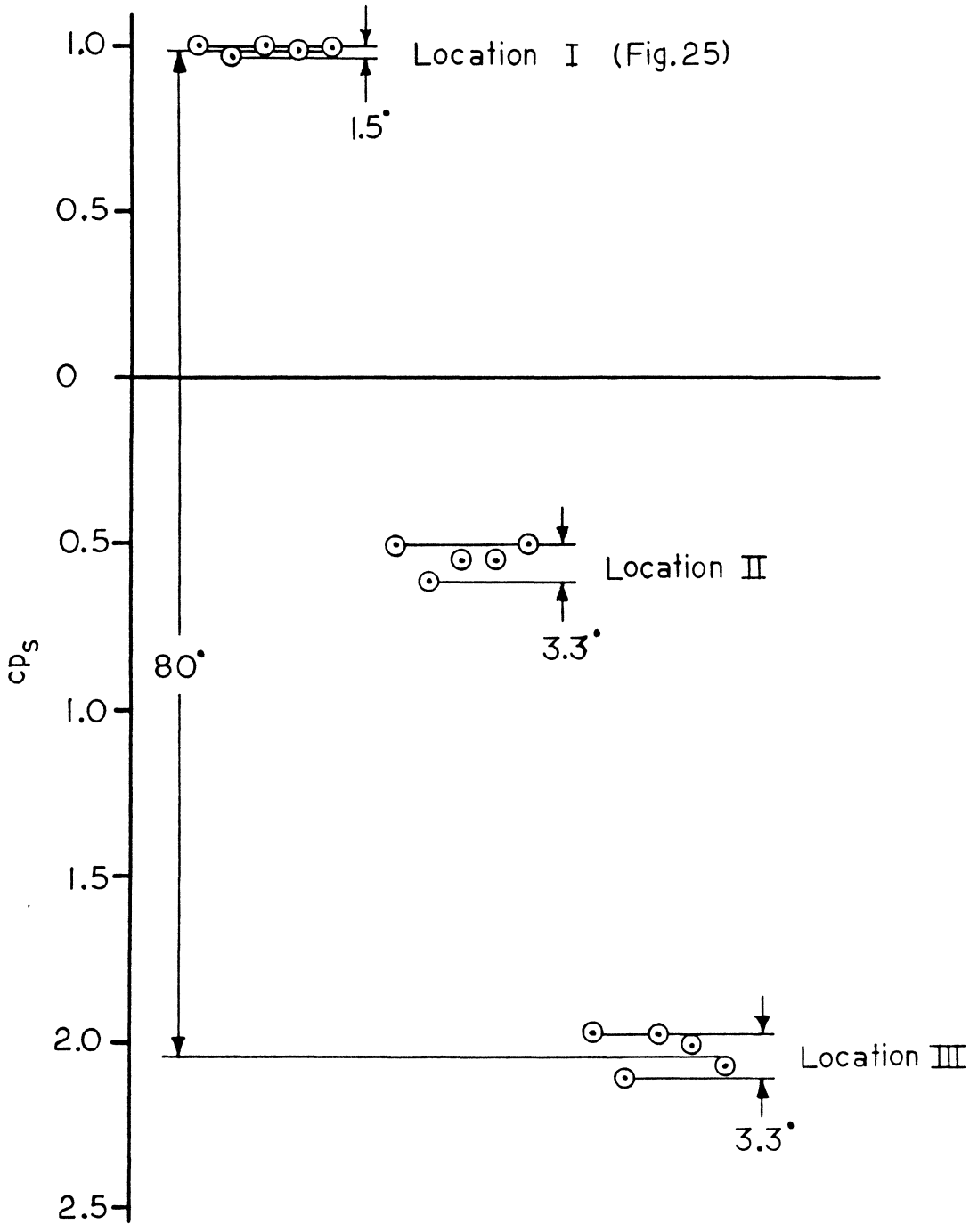

Fig. 30 Comparison of the Static Pressure Coefficients on the Round Leading Edges of the Blades.

3. Upstream Endwall Boundary Layers

The boundary layer parameters for the six upstream undwall traverses are presented in Table 3. Seventeen readings were taken in each boundary layer with additional readings in the freestream flow. The measurements were taken in approximately 0.13 mm increments with the traversing gear described in Section III.F. The calculated turbulent boundary layer thickness, based on the probe tip being located 36.5 mm downstream of the trip wire on the chamfer of the two aluminum bleed pieces, was 1.57 mm. Adding on the diameter of the trip wire, 0.51 mm, the estimated boundary layer thickness was 2.08 mm, which was close to the measured values.

The shape factors were close to the zero pressure gradient value for a flat plate, $H_{12} = 1.4$, which was expected.

The small deviations can probably be explained by the fact that no corrections were applied to the locations of the pressure measurements near the endwall (effective locations). Also, a linear velocity profile was assumed between the near wall measurement point and the endwall.

Improvements in the shape factor evaluation would probably require knowledge of the skin friction coefficient which we were not able to measure, due to the extreme thinness of the boundary layer at the pitot probe locations.

One important observation from the consistency of the boundary layer parameters in Table 3 was that they indicated that the boundary layer bleeds were functioning as designed. The boundary layers did not convect down the aluminum bleed piece and pile up on one side wall of the wind tunnel.

Table 3. Results of Boundary Layer Measurements Upstream of the Cascade

(i) Bottom Endwall:

	Blade 2	Blade 3	Blade 4
δ_{99}	2.18 mm	2.06 mm	2.18 mm
δ^*	0.30 mm	0.29 mm	0.26 mm
Θ	0.20 mm	0.19 mm	0.18 mm
H_{12}	1.50	1.48	1.47

(ii) Top Endwall:

	Blade 2	Blade 3	Blade 4
δ_{99}	2.18 mm	2.18 mm	2.31 mm
δ^*	0.26 mm	0.29 mm	0.30 mm
Θ	0.18 mm	0.20 mm	0.20 mm
H_{12}	1.47	1.49	1.49

4. Blade Loading

The static pressure distribution around the blade at 45 percent span is presented in Fig. 31. The squares represent values from Moore and Ransmayr [17], who used the same blade shape and size but had no tip gap in a slightly different wind tunnel configuration. The agreement is good, especially on the pressure surface. However, there are quite large differences along the suction surface.

One reason for this is that the ratio of the inlet boundary layer displacement thickness to the passage height for the present tests is much smaller ($\delta^*/\Delta z = 0.0012$) than that of Moore and Ransmayr ($\delta^*/\Delta z = 0.023$). The effectively larger mass flow rate in the present tests increased the loading on the blade. This effect of lowered suction surface pressures, caused by a thinner inlet boundary layer was also observed by Graziani, et al. [6].

Secondly, the thinner inlet boundary layer, combined with the presence of a tip gap, alters the three-dimensionality of the flow. Our blade cascade had a smaller passage vortex in the upper half of the passage, little evidence of a horseshoe vortex near the bottom endwall, and a tip leakage vortex. Thus, the three-dimensional flow in the present tests is quite different from that of the earlier tests; and variations in the wall static pressure, especially on the suction surface, are also correspondingly different.

5. Tip Gap Static Pressures

Figure 32 shows the static pressure tapping locations used for the tip gap along plane 6a-7aa, which is approximately the path of the flow

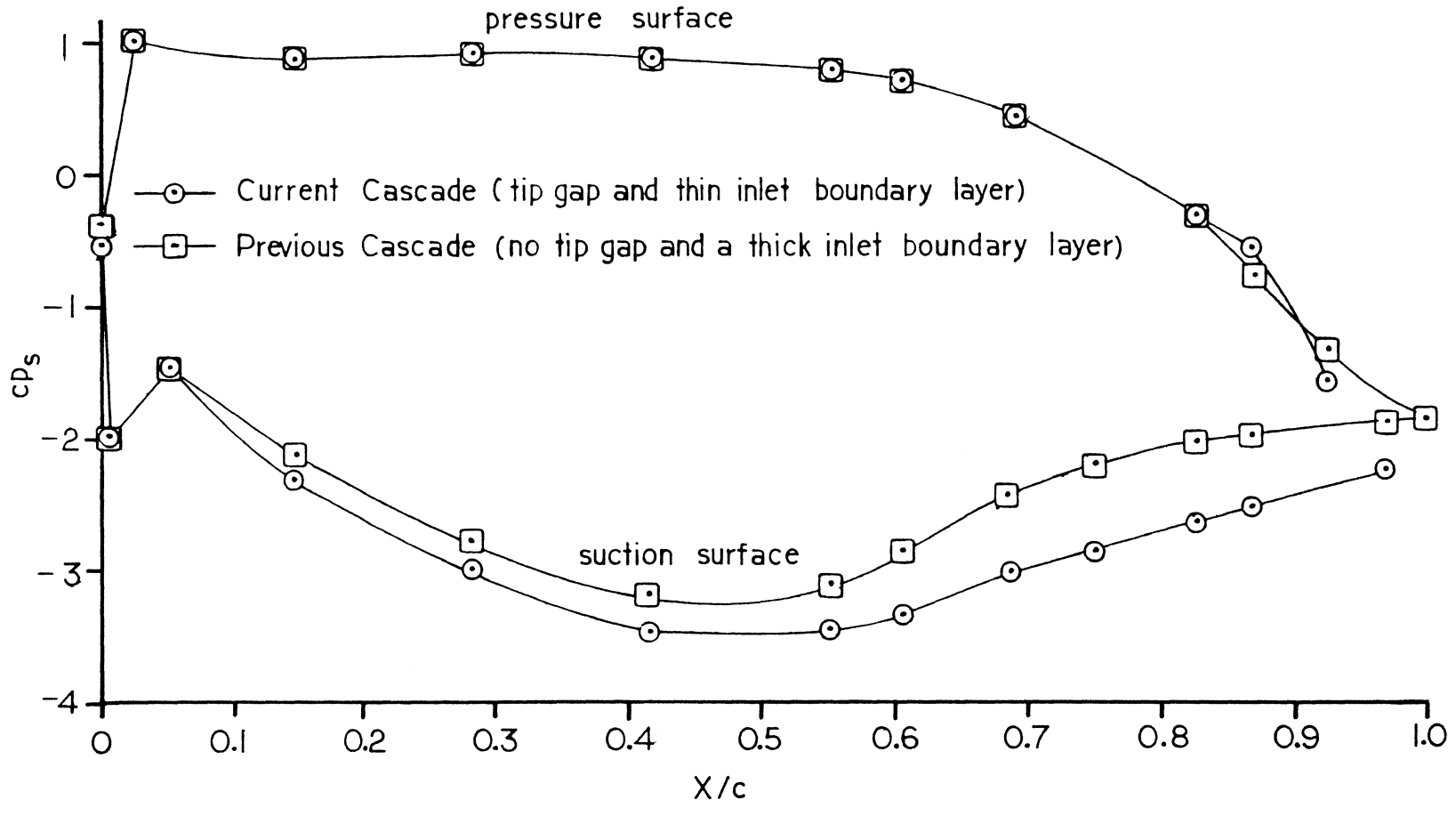

Fig. 31 Static Pressure Distribution Around Blade 3 at 45 Percent Span.

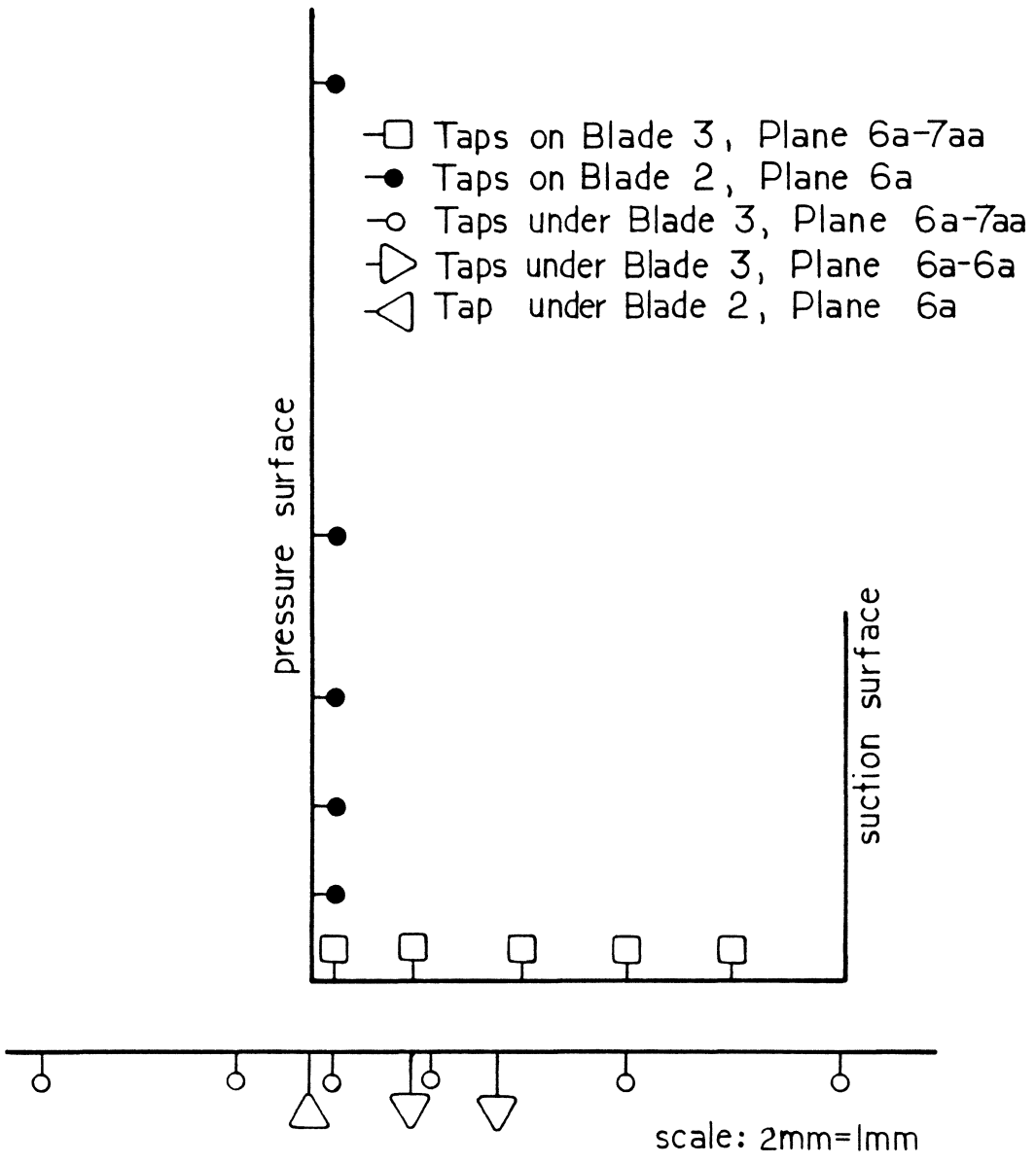

Fig. 32 Static Pressure Tapping Locations Used for the Tip Gap Static Pressure Distribution.

entering the tip clearance at plane 6a. The static pressure distribution is displayed in Fig. 33. The static pressures along the bottom endwall, represented by the dotted line, show the flow accelerating rapidly as the tip gap is approached. At the entrance of the tip gap, cp_s has fallen from 0.61 down to -2.44. The flow continues to accelerate along the endwall until approximately 18 percent through the gap where $cp_{s,min} = -5.8$. Along the blade bottom, near the entrance to the tip clearance, cp_s is quite low, -6.9 to -6.8. Now, in the same region through the tip gap, 18-20 percent, both the endwall and blade bottom pressures start to rise rapidly, reaching about the same pressure at the tip gap exit, $cp_s = -3.1$.

Several observations can be made. The velocity on the blade bottom is expected to be quite high with such a low pressure. Assuming Bernoulli's equation applies, the velocity can be estimated,

$$P_{upstream} + \underbrace{\frac{1}{2}\rho U^2_{upstream}}_{o} = P_{min} + \frac{1}{2}\rho U^2_{max}$$

or

$$\frac{P_{upstream} - P_{so}}{\frac{1}{2}\rho U_o^2} = \frac{P_{min} - P_{so}}{\frac{1}{2}\rho U_o^2} + \frac{U_{max}^2}{U_o^2}$$

Thus

$$cp_{s,upstream} - cp_{s,min} = \frac{U_{max}^2}{U_o^2}$$

or

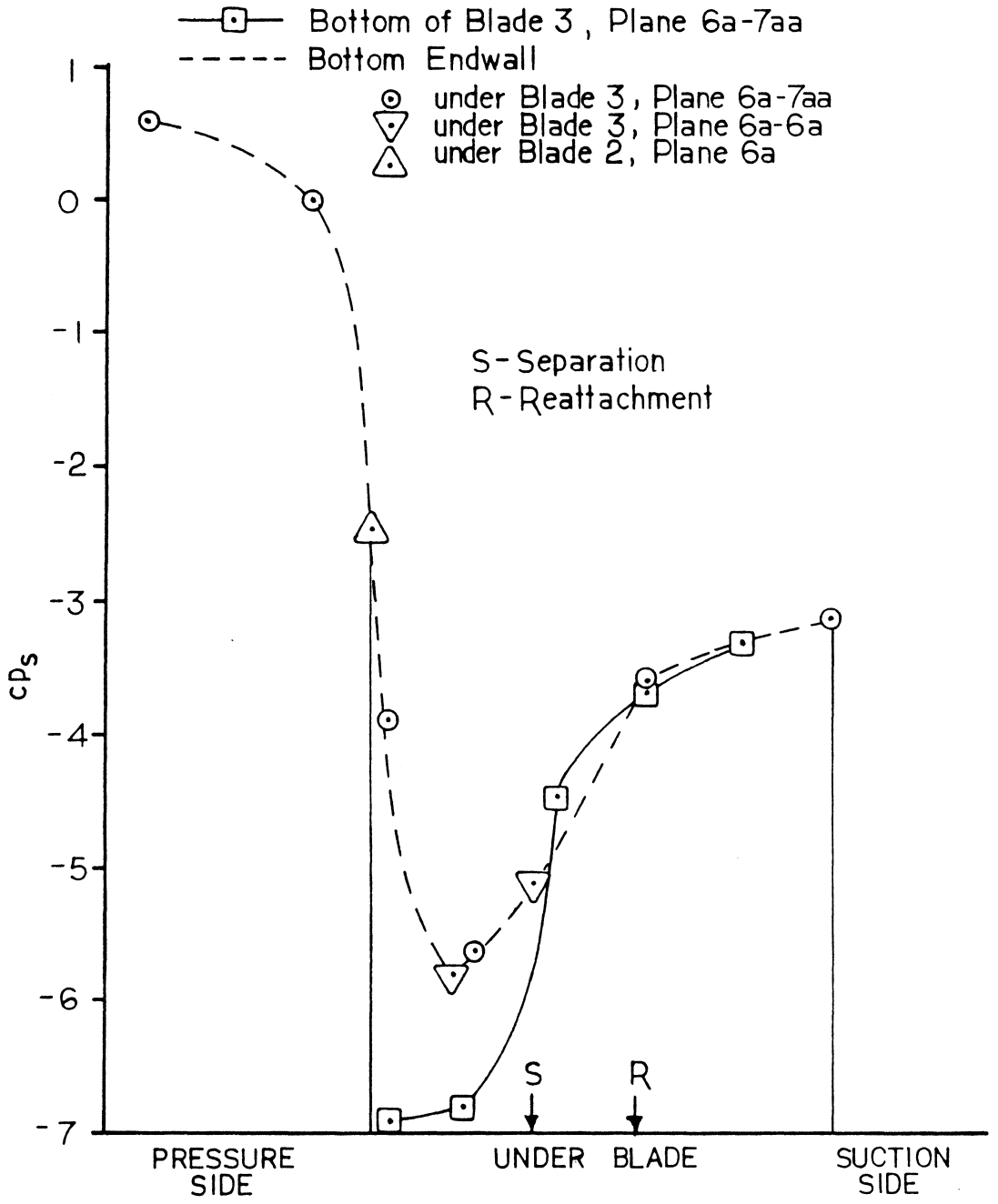

Fig. 33 Tip Gap Static Pressure Distributions, Plane 6a-7aa.

$$\frac{U_{max}}{U_o} = \left(cp_{s,upstream} - cp_{s,min}\right)^{1/2} \quad .$$

With $cp_{s,upstream,ideal} = 1.0$ and $cp_{s,min} = -6.9$,

$$\frac{U_{max}}{U_o} = \left(1.0 - (-6.9)\right)^{1/2}$$

$$\therefore \frac{U_{max}}{U_o} = 2.81 \text{ and } U_{max} = 56.5 \text{ m/s} \quad .$$

Also, mixing seems to occur in the final 80 percent of the tip gap, as evidenced by the slowing of the flow or equivalently, the pressure rise on both the endwall and the bottom of the blade. This suggests two things. The first is the presence of a vena contracta at the minimum pressure along the endwall. This vena contracta has been hypothesized by Graham [14] and Rains [10]. The second is that the pressure through the tip gap at the exit seems to be quite uniform.

From the flow visualization, Fig. 21, separation is seen to occur on the endwall at approximately 35 percent along plane 6a-7aa, with reattachment at approximately 56 percent of the tip gap width, marked by S and R respectively in Fig. 33. At the separation point cp_s is read as -5.1. Bernoulli's equation can be used again to get the following:

$$\frac{\frac{U}{U_o}}{\frac{U_{max}}{U_o}} = \frac{\left(cp_{s,upstream} - cp_s\right)^{1/2}}{\left(cp_{s,upstream} - cp_{s,min}\right)^{1/2}} \quad .$$

From the vena contracta, $cp_{s,min} = -5.8$, to this separation point, the flow slows to

$$\frac{U}{U_{max}} = \frac{(1.0 - (-5.1))^{1/2}}{(1.0 - (-5.8))^{1/2}}$$

$$\therefore \frac{U}{U_{max}} = 0.95 \quad .$$

Turbulent separation occurs in the range of $U/U_{max} = 0.5 - 0.7$, whereas laminar separation occurs when $U/U_{max} \simeq 0.95$. Thus, this value suggests laminar separation and supports the conclusion of Belik [15] and Senoo [16] that the endwall boundary layer can be laminar. The present results suggest that the endwall boundary layer downstream of lines L1 and L2, refer to Fig. 22, is laminar.

The pressure distribution for the tip gap along plane 6a-6a, Fig. 34, shows similar behavior.

6. Tip Gap Exit Velocity Distribution

The tip gap exit velocity profiles for planes 6a-6a and 6a-7aa are plotted and compared in Fig. 35. The velocities were determined with the assumption that uniform exit static pressures existed at both planes, refer to Section V.B.5. The higher velocities at plane 6a-7aa than at plane 6a-6a can partly be explained using Fig. 27. For the flow that exits at plane 6a, the area under the tip gap increases more than it does at plane 7aa due to the larger curvature of the blade. Therefore the flow exiting at plane 6a has been diffused greater than

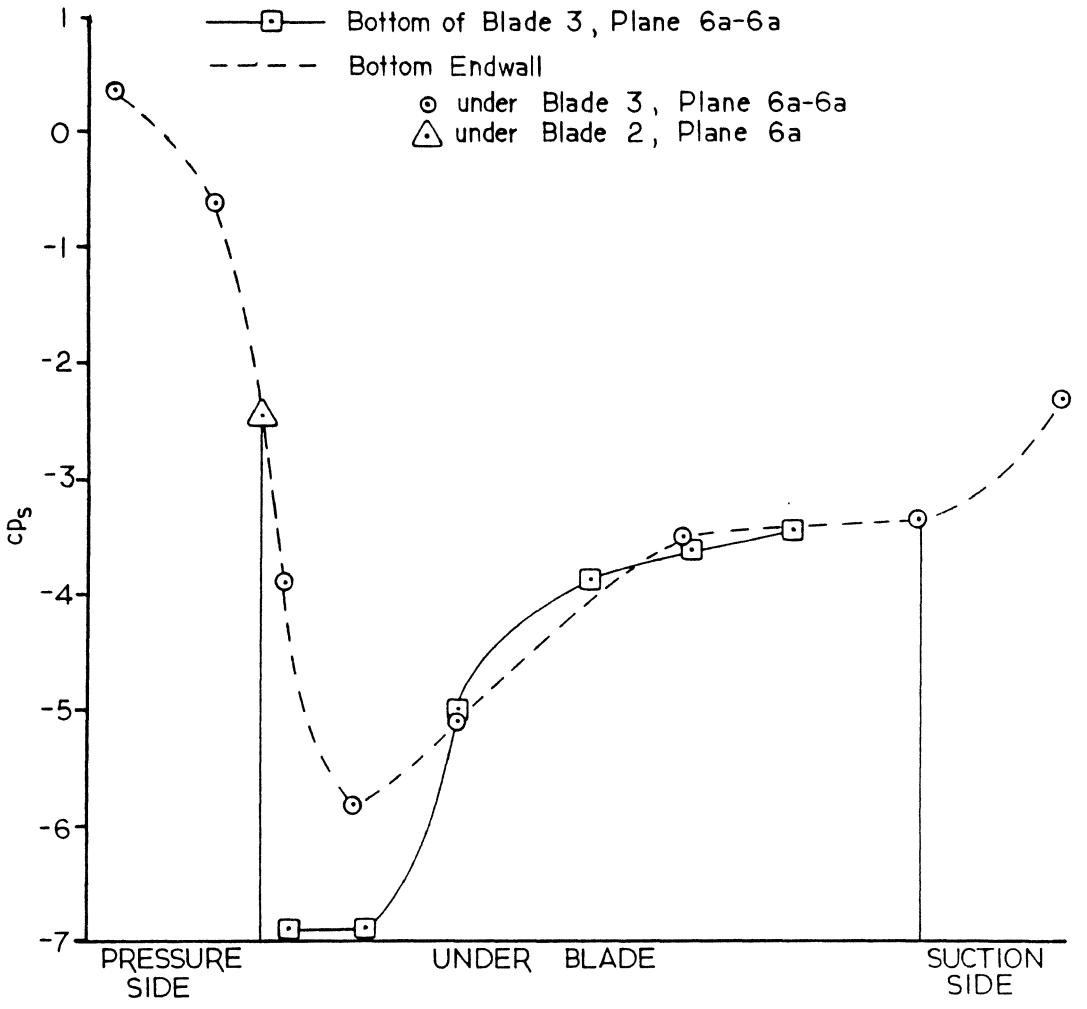

Fig. 34 Tip Gap Static Pressure Distributions, Plane 6a-6a.

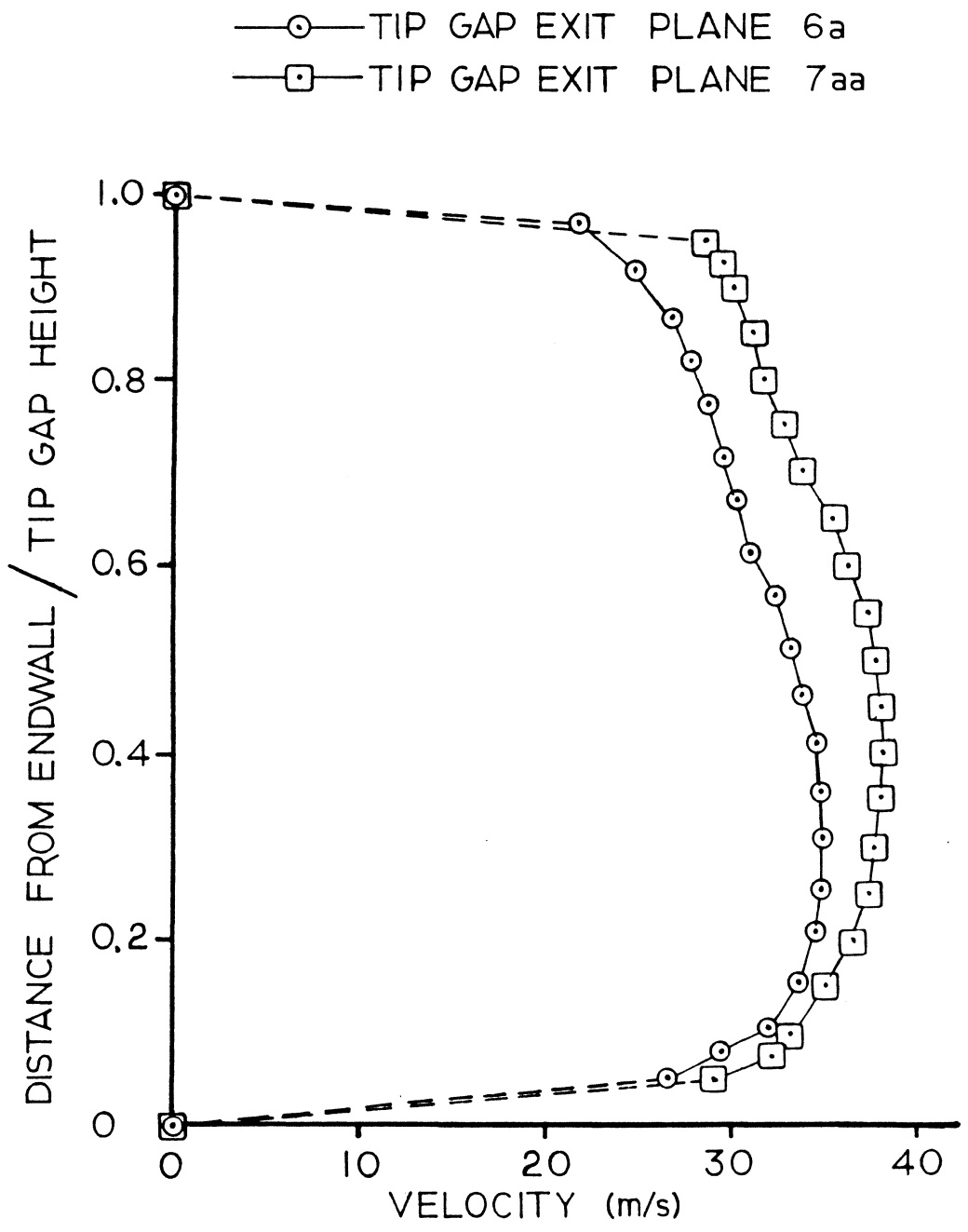

Fig. 35 Exit Tip Gap Velocity Distributions, Planes 6a and 7aa.

the flow exiting at plane 7aa. Another factor contributing to the different exit velocites could be the different pressure drops along the two flow paths.

The endwall boundary layer velocity profile at the tip gap exit for plane 6a-7aa, taken from Fig. 35 to have a thickness of 2.05 mm, is plotted in Fig. 36. It is compared against a laminar boundary layer velocity profile, represented by a parabolic curve, and a turbulent boundary layer velocity profile, represented by a 1/7th power curve. As Fig. 35 shows, the measured data points are very close to resembling a turbulent boundary layer velocity profile. Hence, it is assumed that at the tip gap exit, the boundary layer is turbulent. Thus, after the laminar boundary layer separation approximately 35 percent of the way into the tip gap, the reattachment that follows at approximately 56 percent of the tip gap is probably turbulent. This conclusion is counter to what Graham [14] supposed; he thought that the tip gap exit boundary layer was "undoubtedly" laminar.

7. Blade Passages

Figure 37 shows the pressure distribution around the throat of the passage. The top half of the passage, which had no tip gap, is marked by the solid line. This pressure distribution is similar in shape to the ones found by Moore and Ransmayr [17], Langston, et al. [3], and Graziani, et al. [6]. All of these studies were on blade cascades with no tip gaps. The shape of the pressure distribution near the corner of the endwall and the suction surface is characteristic of flow with a passage vortex.

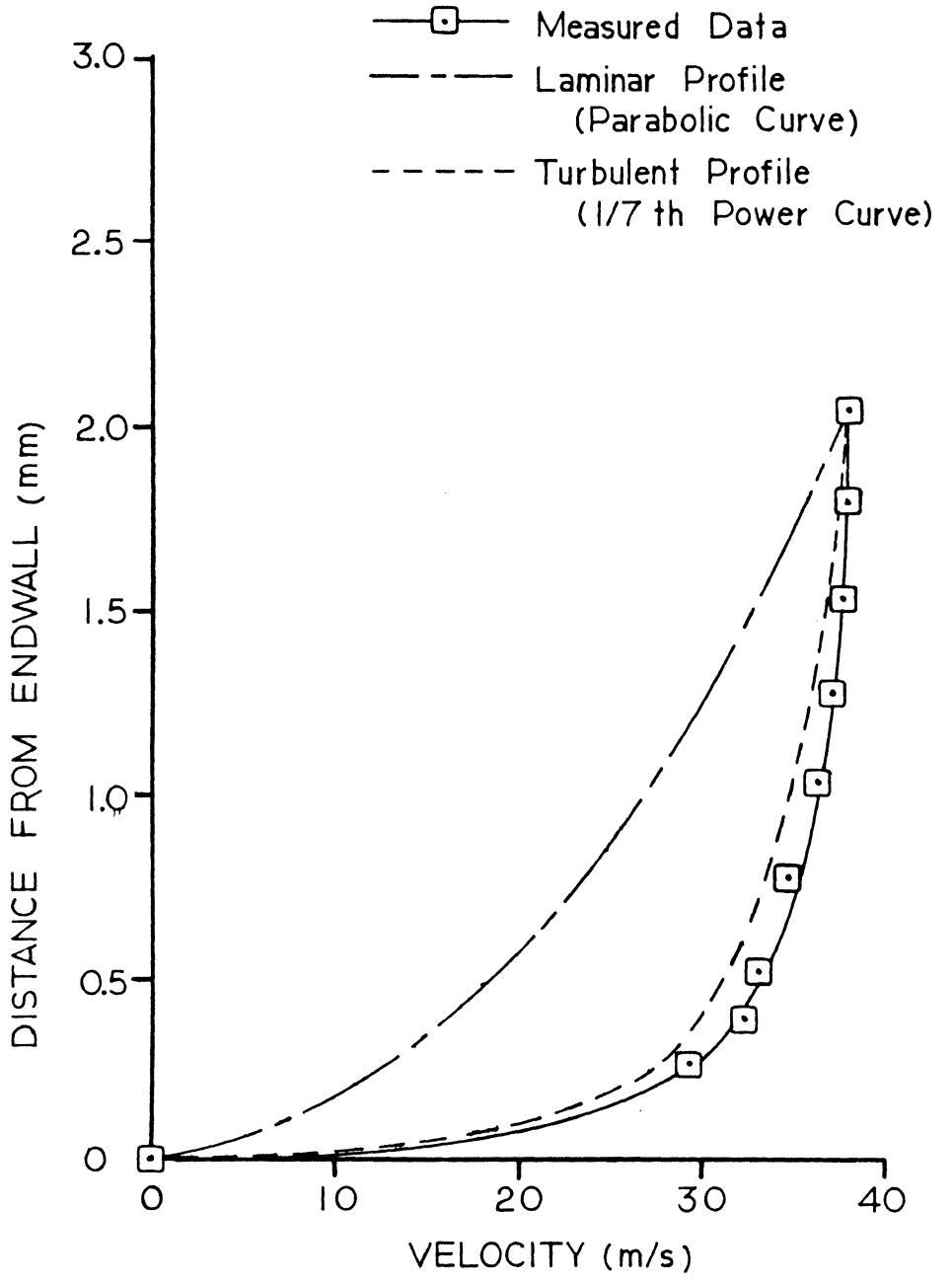

Fig. 36 Comparison of Tip Gap Exit Endwall Boundary Layer Velocity Profile, Plane 7aa, with Laminar and Turbulent Boundary Layer Velocity Profiles.

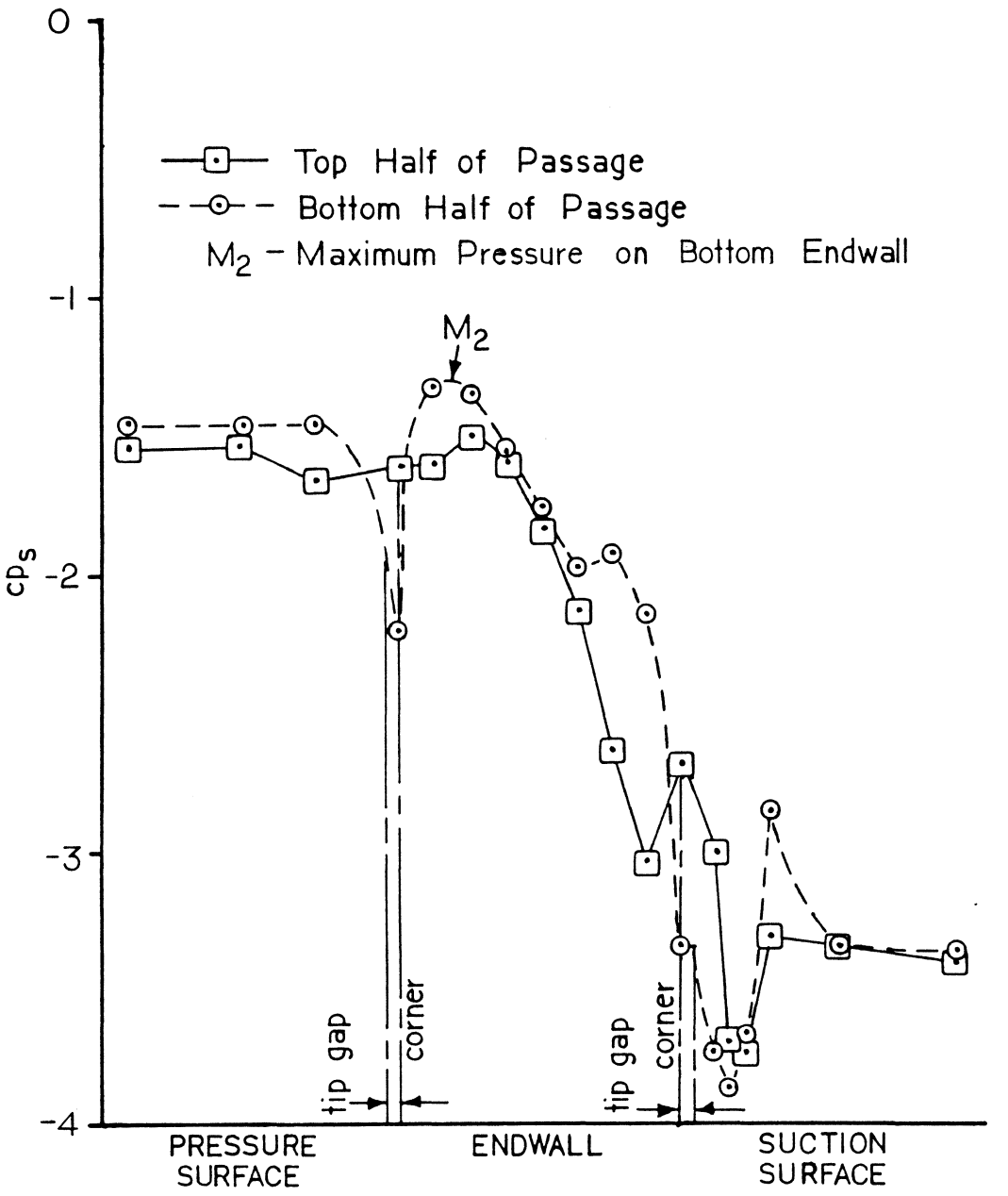

Fig. 37 Wall Static Pressure Distribution Around the Throat of the Blade Passage (Plane 6a-8b).

However, the behavior of the bottom half of the passage, the dotted line, is quite different. (Figure 24 shows a tentative picture of what is happening in this part of the throat.) Going down the pressure surface, as the tip gap is approached, blade unloading occurs rapidly. As shown in Fig. 33, the pressure is not uniform across the tip gap entrance.

Proceeding across the passage towards the suction side, as the distance from the tip gap is increased, the pressure rises to a maximum (point M2 in Fig. 22). The pressure then falls as the suction surface is approached, due to the curvature of the flow path, see Fig. 22.

At about 70 percent of the distance across the endwall, toward the suction surface, a small pressure minimum occurs. Referring again to Fig. 24, this is due to the secondary flow climbing over the tip leakage vortex. The uplifting of this fluid causes the pressure increase, which can be qualitatively explained by the equation

$$\frac{\partial P}{\partial r} \simeq \rho \frac{V^2}{r} \quad .$$

From here to the tip gap, the pressure falls as the tip gap leakage flow becomes stronger, until the tip gap itself is reached. The pressure across the tip gap exit, unlike the tip gap entrance, is nearly uniform, as is shown in Fig. 34.

Going up the suction surface of the blade, the pressure reaches a minimum, due to the influence of the tip gap leakage vortex adjacent to the blade, again see Fig. 24.

Rapidly the pressure then rises to a maximum between the tip leakage vortex and the passage vortex. This is caused by the passage vortex which has now climbed over the tip leakage vortex. Fluid between these two vortices is convected towards the suction surface causing a near stagnation of secondary flow at the wall and a corresponding pressure peak.

As mentioned previously, the passage vortex in the lower half of the passage is weak and hard to detect with a wool tuft. If there had been more pressure tappings along this spanwise section of the blade, or if the passage vortex had been stronger, we would expect a second pressure minimum on the suction surface, this one just above the pressure maximum. This would be the point where the core of the passage vortex came close to contacting the blade.

The static pressure distribution around plane 6a-6a of the blade passage is presented in Fig. 38. Similar flow behavior as in Fig. 37 is seen, with higher pressures on the pressure surface of the blade, at plane 6a, upstream of plane 8b. Significant blade unloading occurs between planes 6a and 8b as seen in Fig. 31. This leads to lower velocities and higher pressures at plane 6a.

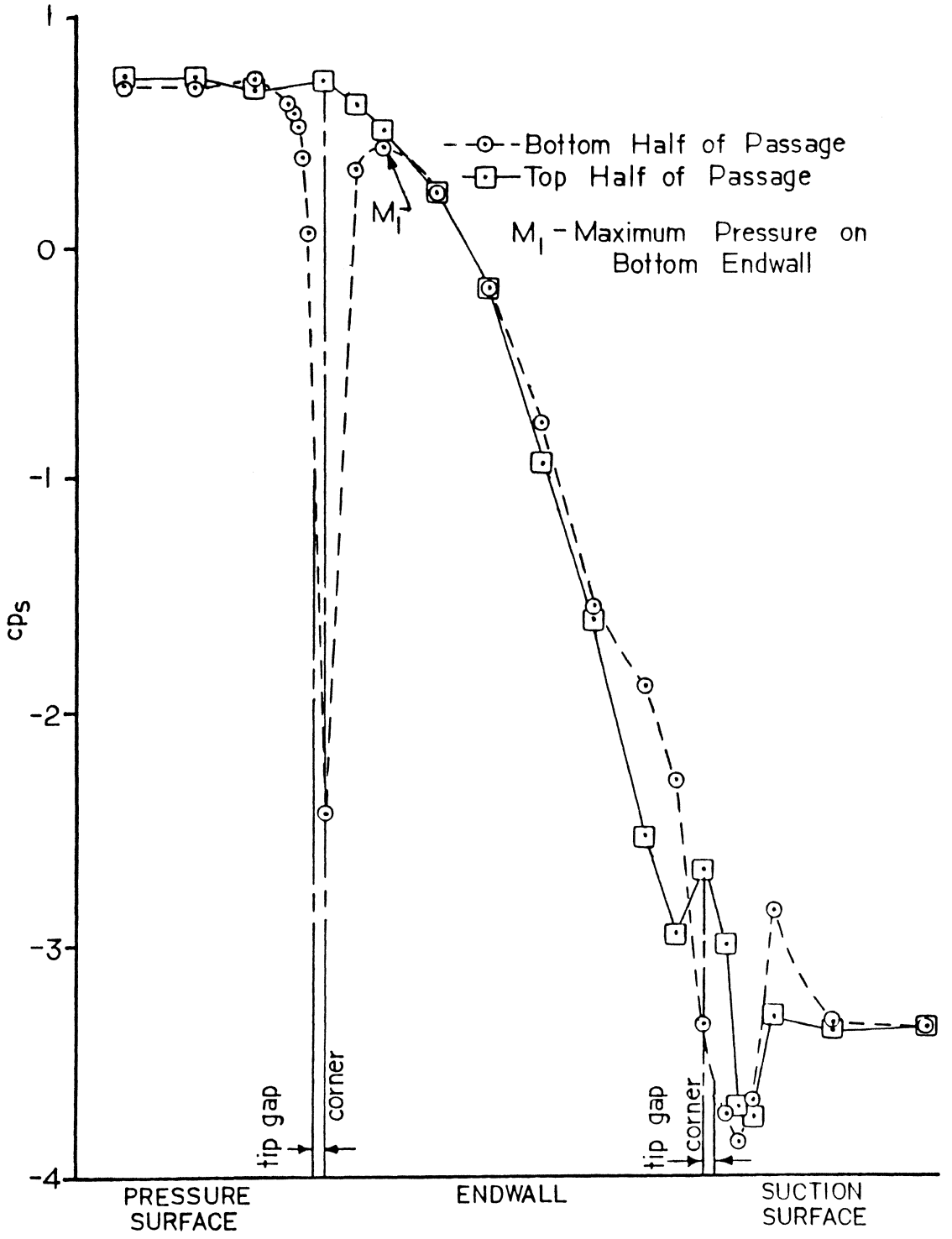

Fig. 38 Wall Static Pressure Distribution Around the Blade Passage at Plane 6a-6a.

VI. FLOW ANALYSIS

A. Potential Flow Analysis

Potential flow theory has been used before to describe flow into a tip gap. Rains [10] in 1954, developed a model, based on flow at rest entering a slot, Fig. 39, where, based on symmetry, the centerline of the slot was the bottom endwall. His solution yielded the following equation for obtaining the velocity at any position in the flow field

$$z = x + iy = \frac{\delta_t \sigma}{\pi} \left[\ell n\left(\frac{W_t + \zeta}{W_t - \zeta}\right) - \frac{2W_t}{\zeta} + \frac{i\pi}{2} \right]$$

where σ, the contraction ratio, is $\pi/(\pi+2)$, ζ is the complex velocity, u-iv, and W_t is the tip clearance velocity normal to the blade. Using Bernoulli's equation between the upstream and downstream pressures, P_1 and P_2, respectively, then

$$W_t = \left(\frac{2(P_1 - P_2)}{\rho} \right)^{1/2}$$

This solution has two limiting cases. One is for flow along the endwall and the other is for flow on the pressure surface of the blade as the tip gap is approached. Rayleigh [18], in 1876, also solved this potential flow problem, however, just for these two limiting cases. The two theories, Rayleigh's and Rains', are compared for the endwall in Fig. 40, and for the pressure surface of the blade in Fig. 41. The discrepancy was found to be in Rains' theory. The corrected general solution was found to be:

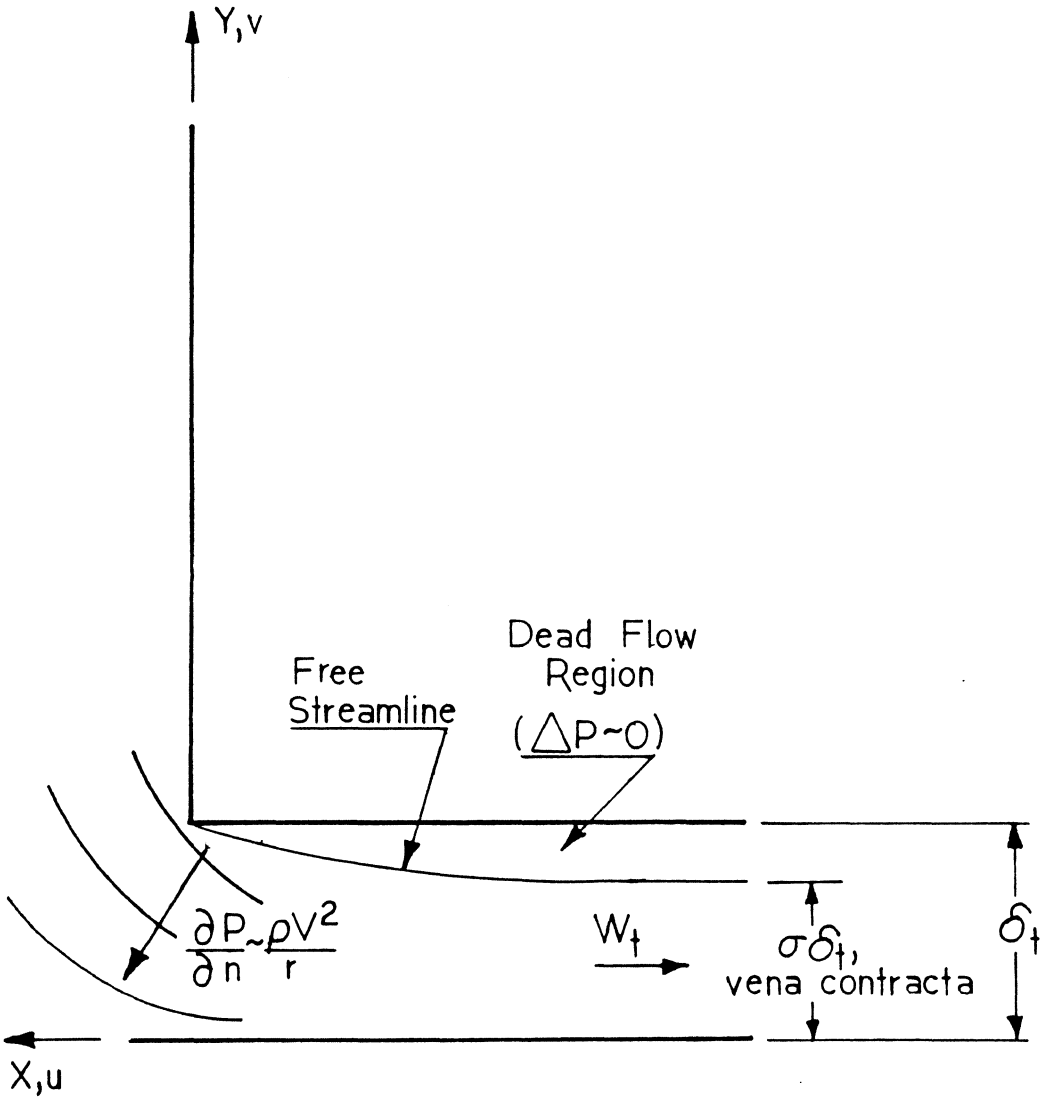

Fig. 39 Potential Flow Model of Flow into a Tip Gap.

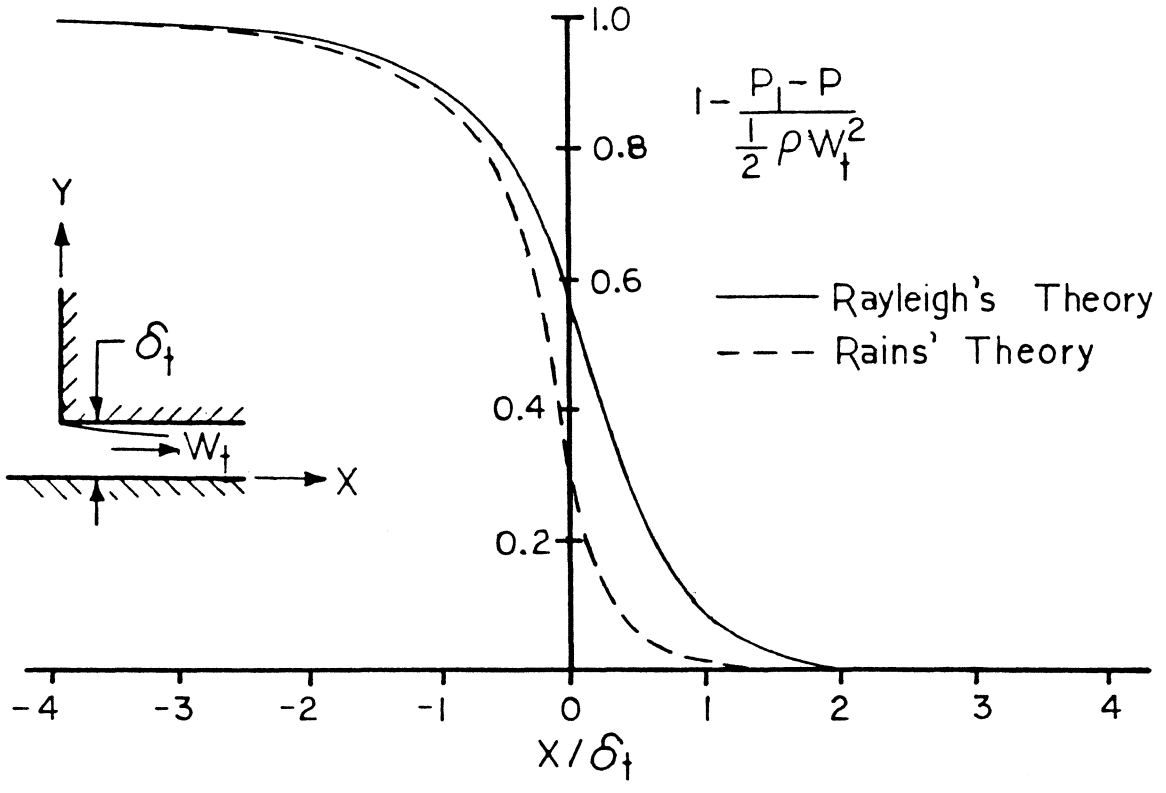

Fig. 40 Comparison of Rayleigh's and Rains' Potential Flow Solutions, Pressures on Bottom Endwall.

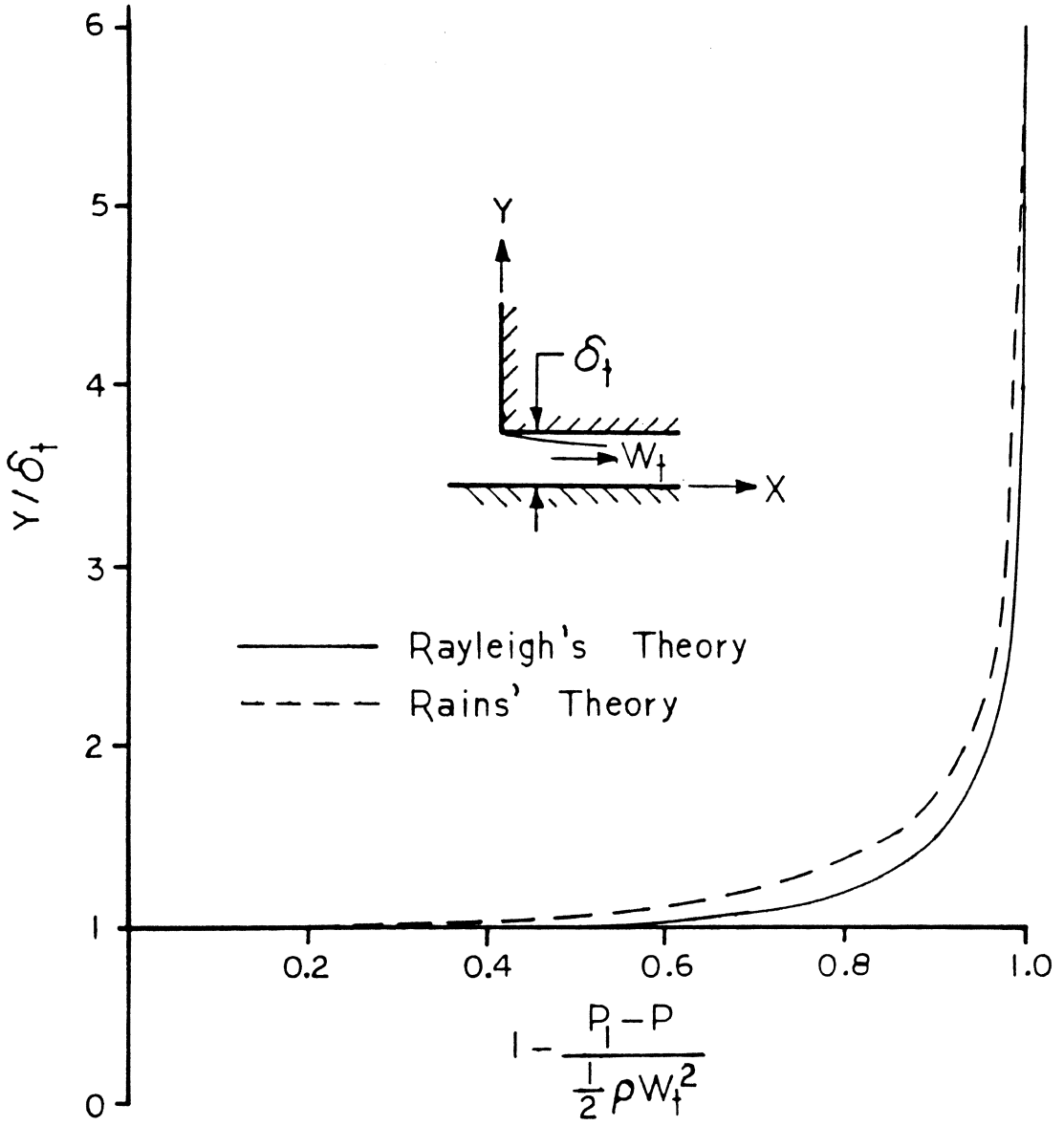

Fig. 41 Comparison of Rayleigh's and Rains' Potential Flow Solutions, Pressures on Blade Pressure Surface.

$$z = x + iy = \frac{2\delta_t \sigma}{\pi} \left[\ell n \left(\frac{W_t + \zeta}{W_t - \zeta} \right) - \frac{W_t}{\zeta} \right]$$

where the nomenclature is the same as used by Rains.

The reduction of this solution, obtained from Milne-Thomson [19], to the two limiting cases, which matched Rayleigh's theory, is given in Appendix A.

1. Comparison with Static Pressure Data

The static pressure data for flow through the tip gap along plane 6a-7aa is compared with Rayleigh's theory, for the endwall in Fig. 42, and for the pressure surface of the blade in Fig. 43. The static pressure coefficients were normalized in the following way:

$$\frac{cp_s - cp_{s,min}}{cp_{s,max} - cp_{s,min}} .$$

For all the data, a value of $cp_{s,min} = -6.85$ was used. This was the average value of the lowest pressures obtained on the bottom on the blade, rather than on the endwall, see Fig. 33. As shown in Fig. 39, the free streamline, as predicted by potential flow theory, would have approximately the same pressure as the bottom of the blade. This is due to the dead flow region in between the free streamline and the blade bottom surface where pressure differences are small. Then, with curved streamlines, the following equation applies

$$\frac{\partial P}{\partial n} \simeq \frac{\rho V^2}{r}$$

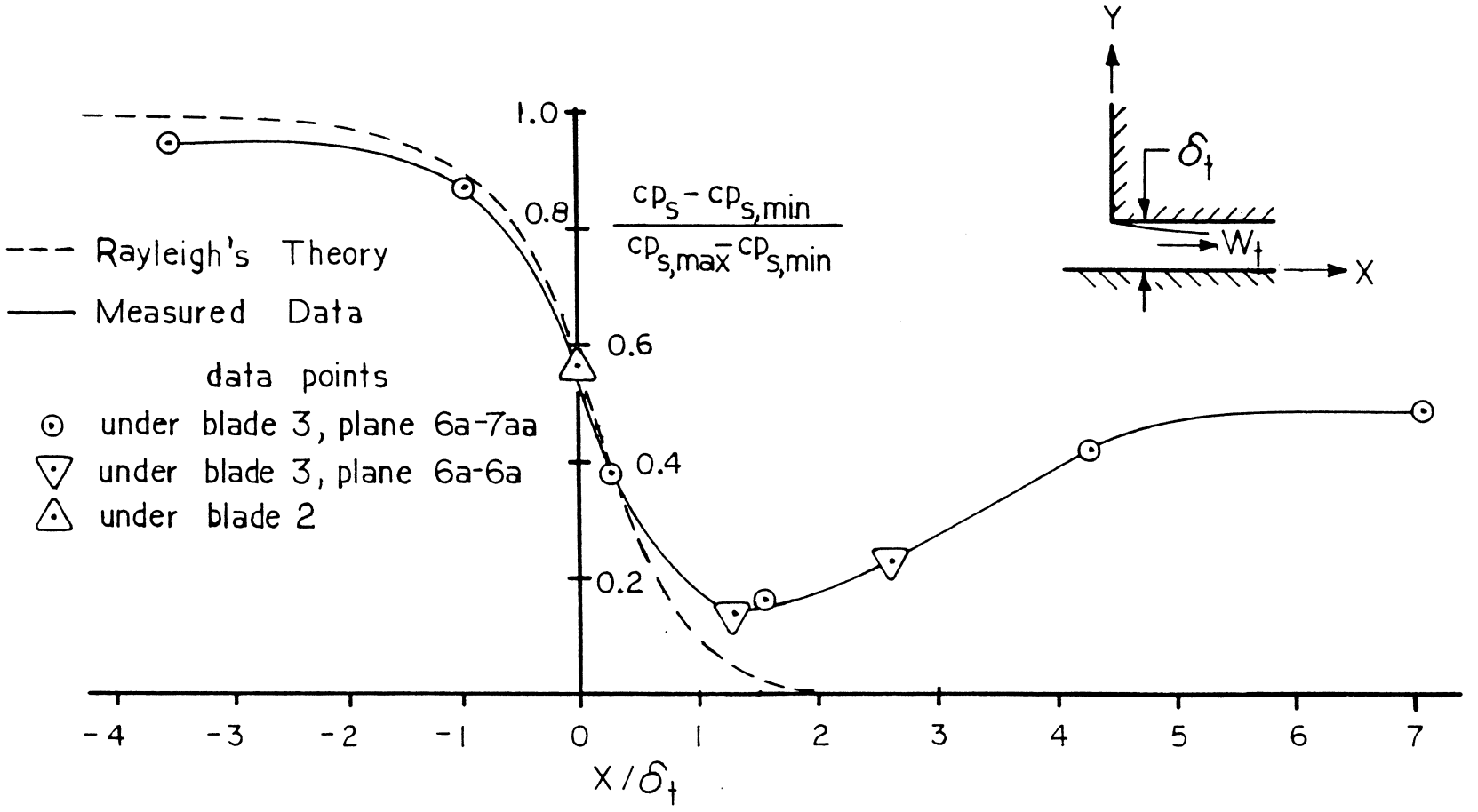

Fig. 42 Normalized Measured Pressures on Endwall Compared with Potential Flow Theory.

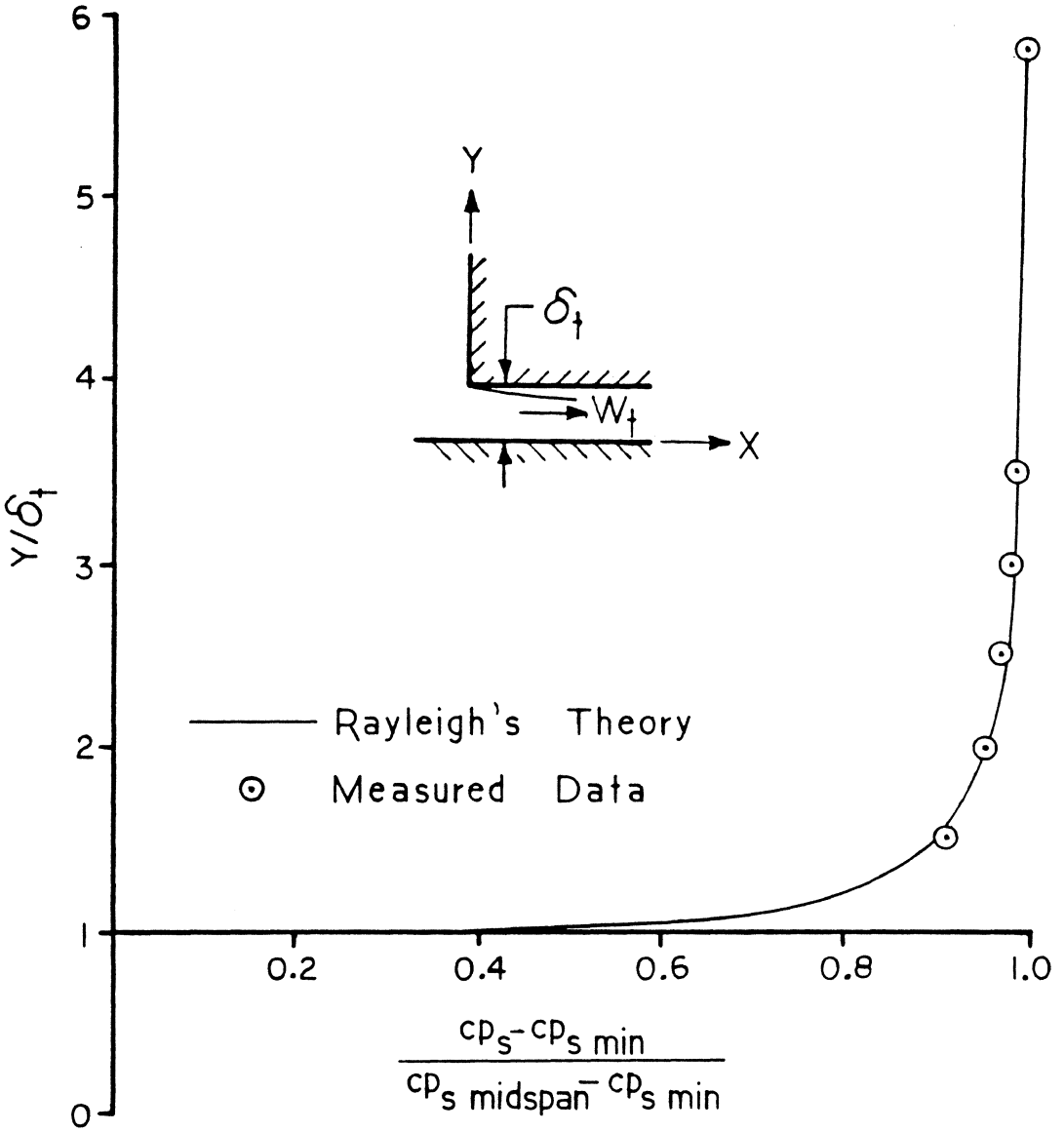

Fig. 43 Normalized Measured Pressures on Blade Pressure Surface Compared with Potential Flow Theory.

This indicates that there will exist a higher pressure at the bottom endwall than at the free streamline, which our data confirms. Thus, Rayleigh's theory, since it is based on a general solution of the flow region, would suggest using this minimum value, and not the minimum pressure along the endwall.

However, the value of $cp_{s,max}$ used for normalizing each limiting case differed. For the bottom endwall, $cp_{s,upstream,ideal} = 1.0$ was used as the maximum possible value. For the pressure surface of the blade, $cp_{s,midspan} = 0.713$ was used as $cp_{s,max}$, obtained from data shown in Fig. 31.

Along the endwall, good agreement is found at the tip gap entrance, for Rayleigh the normalized value is 0.58, and for our data the value is 0.56. Variations soon occur further into the gap as mixing begins, which Rayleigh's theory does not predict. Upstream of the gap the normalized data does not approach 1.0 because the actual $cp_{s,upstream}$ is approximately 0.6, rather than the ideal value of 1.0.

The static pressure distribution on the pressure surface of the blade shows excellent agreement at all points with Rayleigh's theory. For this case, the blade is seen to unload on the pressure surface over about two tip gap heights from the end of the blade.

2. Comparison with the Contraction Coefficient

Another comparison can be made with the potential flow theory and our investigation. Rayleigh shows the theoretical contraction coefficient is 0.611. A two-dimensional contraction coefficient can be calculated from the data as follows:

1) $\dot{Q} = C_c \cdot U_{max} \cdot \delta_t$

2) $\frac{U_{max}}{U_o} = \sqrt{1 - cp_{s,min}}$

Combining 1) and 2)

3) $\dot{Q} = C_c U_o \delta_t \sqrt{1 - cp_{s,min}}$

4) Measured volume rate = $\dot{Q} = \int U d\delta_t$ (continuity)

Combining 3) and 4)

$$C_c = \frac{\int U \frac{d\delta_t}{\delta_t}}{U_o \sqrt{1 - cp_{s,min}}}$$

$\int U \frac{d\delta_t}{\delta_t}$ = Area integral of velocity from plane 7aa, Fig. 35. = 34.3

$$C_c = \frac{34.3}{(20.1)(\sqrt{1 - (-6.85)})}$$

$$\therefore C_c = 0.608$$

This lends further support to the idea that the tip leakage flow exhibits a vena contracta near the entrance of the tip gap. The agreement between the theoretical contraction coefficient and that

deduced from the measurements is excellent. It also suggests that tip gap flow discharge coefficients may be better analyzed using the minimum static pressure under the blade, rather than an overall static pressure drop from the pressure side to the suction side, which is how it is usually done now.

B. Potential Flow with Mixing Analysis

A simple two-dimensional potential flow with mixing model for flow through the tip gap, see Fig. 44, was developed for comparison with our data. For this model, values of $cp_{s,upstream}$ and $cp_{s,exit}$ were assumed fixed at values of 1.0 and -3.1, respectively. This was equivalent to fixing the upstream and exit pressures. The value of $cp_{s,upstream} = 1.0$ is an ideal value, if the upstream flow had no velocity. $cp_{s,exit} = -3.1$ was based on the assumption mixing had occurred and was obtained from Fig. 33. Now, as in Section V.B.5, using the Bernoulli equation for the flow into the tip gap up to the vena contracta,

$$P_{upstream} + \underbrace{\frac{1}{2}\rho U^2_{upstream}}_{o} = P_{min} + \frac{1}{2}\rho U^2_{max}$$

or

$$\frac{P_{upstream} - P_{so}}{\frac{1}{2}\rho U_o^2} = \frac{P_{min} - P_{so}}{\frac{1}{2}\rho U_o^2} + \frac{U_{max}^2}{U_o^2}$$

Thus

1) $$cp_{s,upstream} - cp_{s,min} = \frac{U_{max}^2}{U_o^2}$$

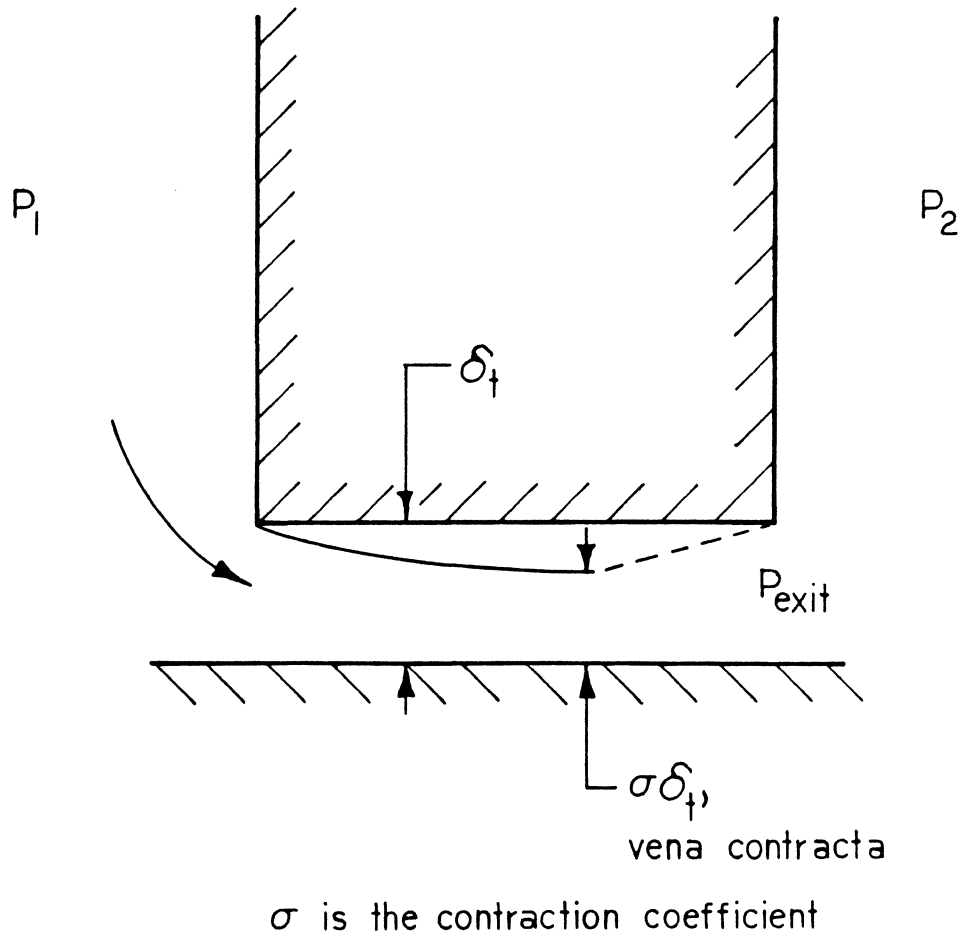

Fig. 44 Sketch of Actual Tip Gap Flow Geometry (not to scale).

Assuming mixing occurs between the vena contracta and the tip gap exit, the momentum equation yields

$$\frac{P_{exit} - P_{min}}{\rho U_{max}^2} = \sigma - \sigma^2 = 0.611 - (0.611)^2$$

$$\frac{P_{exit} - P_{min}}{\rho U_{max}^2} = 0.2377$$

$$\frac{P_{exit} - P_{min}}{\frac{1}{2}\rho U_o^2} = 0.2377 \frac{\rho U_{max}^2}{\frac{1}{2}\rho U_o^2}$$

2) $$cp_{s,exit} - cp_{s,min} = 0.475 \frac{U_{max}^2}{U_o^2} .$$

Combining 1) and 2)

$$cp_{s,min} = \frac{1}{0.525}\left[cp_{s,exit} - 0.475\ cp_{s,upstream}\right]$$

$$cp_{s,min} = \frac{1}{0.525}\left[-3.1 - 0.475\ (1.0)\right]$$

$$\therefore\ cp_{s,min} = -6.81$$

This is the pressure the model will asymptotically approach within the distance of approximately two tip gaps under the blade, referring to Fig. 42. It agrees well with measured minimum static pressure coefficient of -6.85, see Fig. 33.

On the endwall at the tip gap entrance, the model predicts

$$cp_s = cp_{s,min} + 0.58\left(cp_{s,upstream} - cp_{s,min}\right)$$

$$cp_s = -6.81 + 0.58 \left[1 - (-6.81)\right]$$

$$cp_s = -2.28$$

Again, this compares well with the measured value of -2.44 from Fig. 33.

The endwall static pressure distribution for this model is compared to the measured data in Fig. 45. The pressure drop into the gap is predicted well, as the vena contracta is approached. If no mixing occurred after the vena contracta, the pressure would remain at the minimum pressure, as shown by the intermittent line. With mixing, the rate of the theoretical pressure rise can only be estimated, shown by the dotted line. It may, in fact, approach the data more closely.

One major difference between this model, which includes mixing, and the actual turbine cascade, is that the area in the tip gap region increases perpendicular to the camber line across the blade width. Thus, in reality, the flow area is not constant and the flow geometry is not exactly two-dimensional. Secondly, this model does not account for the observed laminar boundary layer separation or the turbulent boundary layer reattachment on the endwall in the tip gap, both of which are shown graphically in Fig. 46. However, for a simple analysis, this two dimensional potential flow model is surprisingly accurate.

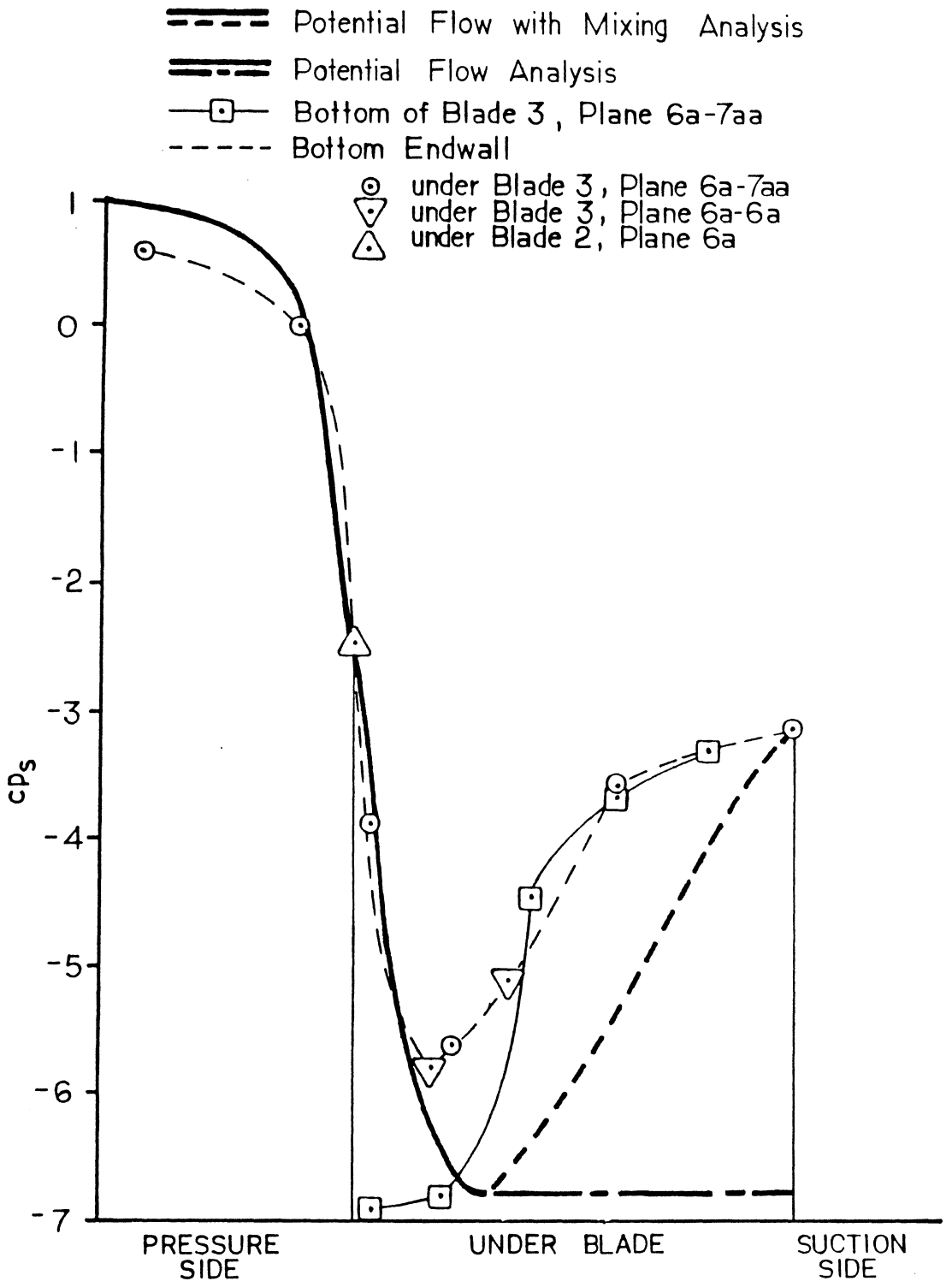

Fig. 45 Tip Gap Static Pressure Distributions, Plane 6a-7aa, Compared with Flow Models.

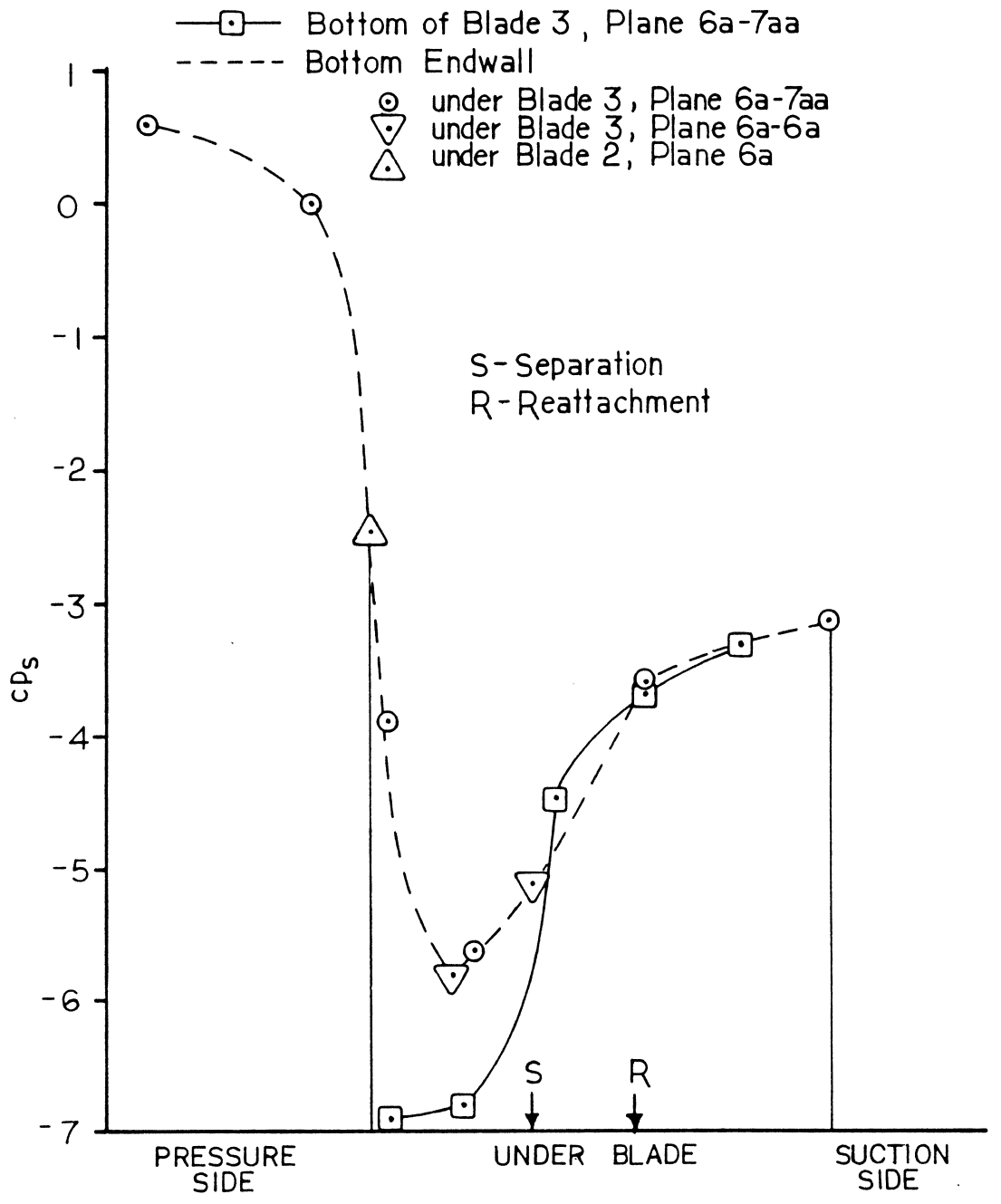

Fig. 46 Tip Gap Static Pressure Distributions, Plane 6a-7aa.

VII. CONCLUSIONS

A. Purpose of Study

Attempts to control flow through the tip clearance gap on turbine blades have been based on minimizing the discharge coefficient under the blade tips. To effectively alter the discharge coefficient, however, the flow behavior in the tip gap region must be understood. This study investigated and analyzed the tip gap leakage flow on a five blade linear turbine blade cascade.

B. The Wind Tunnel

The cascade was geometrically similar to the earlier VPI&SU cascade with the addition of a tip gap and two endwall boundary layer bleeds. Some important information concerning the tunnel is:

1. A uniform tip gap of 2.1 percent, 5mm, of the blade height existed with only slight variations across the blade row. This tip gap with a stationary endwall exhibited a tip leakage vortex, as commonly found in turbines with tip gaps of at least 1.2 percent of the blade height while operating at normal engine speed. Since this applies to most real turbines, our test was a good simulation.
2. The repeatability of the cascade flow was established through similar flow visualizations and from static pressure measurements on the leading edges of the blades.
3. The two endwall boundary layer bleeds performed as designed, reducing the inlet endwall boundary layer thickness upstream

of the blades ($\delta^*/\Delta z = 0.0012$) below the size of tip gap ($\frac{\delta_t}{\Delta z} = 0.021$).

4. The exit Reynolds number based on the axial chord was 4.5×10^5.

C. Tip Leakage Flow Measurements

The static and total pressure measurements and the flow visualizations gave the following results:

1) Blade unloading occurred on the pressure surface of the blade as the tip gap was approached.

2) A pressure minimum existed on the bottom surface of the blade near the inlet of the tip gap, $cp_s = -6.85$.

3) Higher pressures were measured on the endwall than on the bottom of the blade except near the tip gap exit.

4) A vena contracta occurred close to the tip gap entrance.

5) The contraction coefficient, based on the minimum pressure under the blade and the measured exit flow, was calculated as 0.61 (previous calculations of tip leakage flow have used an overall discharge coefficient based on a downstream pressure instead of the minimum pressure in the tip gap).

6) The static pressure rose from the vena contracta, $cp_{s,min} = -6.85$, to the tip gap exit, $cp_{s,exit} = -3.1$.

7) A fairly uniform static pressure distribution existed across the tip gap at the exit.

8) A fairly uniform tip gap exit velocity distribution gave evidence of flow mixing in the latter part of the tip gap.

9) A laminar boundary layer separation took place under the blade, suggesting a laminar endwall boundary layer upstream of the tip gap.

10) A turbulent endwall boundary layer was seen at the tip gap exit, probably due to a turbulent boundary layer reattachment after the laminar boundary layer separation.

11) A tip leakage vortex existed in the passage, as predicted, and appeared to displace the passage vortex up the suction surface of the blade.

D. Tip Leakage Flow Models

A model based on potential flow theory with a free streamline corresponding to the minimum pressure under the blade, seems to work well up to the vena contracta. This model, based on the tip gap flow being perpendicular to the camber line of the blade, provides the following:

1) Good agreement of the static pressure distribution on the endwall with the measured values, up to the vena contracta.

2) Good agreement of the blade unloading on the pressure surface of the blade with the measured values.

3) A contraction coefficient of 0.61. This is in excellent agreement with the measured value, and suggests that the minimum pressure under the blade should be used to determine the discharge coefficient of the tip gap.

A model based on potential flow theory and including a one-dimensional mixing analysis after the vena contracta provided not only

the above results but also predicted a minimum static pressure coefficient of -6.81, under the blade (based on $cp_{s,max}$ and $cp_{s,exit}$); this is close to the measured value, -6.85. Thus it gives a well modelled pressure rise from the vena contracta to the tip gap exit. This flow model appears to be more accurate in predicting flow behavior in the tip gap region. With the improved insight offered by this flow model better tip gap design may be possible.

VIII. REFERENCES

1. Booth, T. C., Dodge, P. R., and Hepworth, W. K., "Rotor-Tip Leakage Part 1 - Basic Methodology," ASME Paper No. 81-GT-71, Trans. ASME, J. of Engineering for Power, Vol. 104, January 1982, pp. 154-161.

2. Barber, T. J., and Langston, L. S., "Three Dimensional Modelling of Cascade Flows," AIAA Paper No. 79-0047, 1979.

3. Langston, L. S., Nice, M. L., and Hooper, R. M., "Three-Dimensional Flow Within a Turbine Cascade Passage," Trans. ASME, Journal of Eng. for Power, Vol. 99, Jan. 1977, pp. 21-28.

4. Moore, J., and Adhye, R., "Secondary Flows and Losses Downstream of a Turbine Cascade," ASME Paper No. 85-GT-64, Trans. ASME, J. of Engineering for Gas Turbines and Power, Vol. 107, October 1985, pp. 961-968.

5. Moore, J., and Moore, J. G., "Performance Evaluation of Linear Turbine Cascades Using Three-Dimensional Viscous Flow Calculations," ASME Paper No. 85-GT-65, Trans. ASME, J. of Engineering for Gas Turbines and Power, Vol. 107, October 1985, pp. 969-975.

6. Graziani, R. A., Blair, M. F., Taylor, J. R., and Mayle, R. E., "An Experimental Study of Endwall and Airfoil Surface Heat Transfer in a Large Scale Turbine Blade Cascade," Trans. ASME, J. of Engineering for Power, Vol. 102, April 1980, pp. 257-267.

7. Sieverding, C. H., "Recent Progress in the Understanding of Basic Aspects of Secondary Flow Passages in Turbine Blade Passages," ASME Paper 84-GT-78, Trans. ASME, J. of Engineering for Gas Turbines and Power, Vol. 107, April 1985, pp. 248-257.

8. Herzig, H. A., Hansen, A. G., and Costello, G. R., "A Visualization Study of Secondary Flows in Cascades," NACA TN 2947, Feb. 1953.

9. Roelke, R. J., Turbine Design and Application, ed. by Arthur Glassman, NASA SP-290, 1973, pp. 127-128.

10. Rains, D. A., "Tip-Clearance Flows in Axial Flow Compressors and Pumps," California Institute of Technology Report No. 5, June 1954.

11. Booth, T. C., and Wadia, A. R., "Rotor-Tip Leakage: Part II - Design Optimization Through Viscous Analysis and Experiment," ASME Paper No. 81-GT-72, Trans. ASME, J. of Engineering for Power, Vol. 104, January 1982, pp. 162-168.

12. Lakshminarayava, B., "Methods of Predicting the Tip Clearance Effects in Axial Flow Turbomachinery," Trans. ASME, J. Basic Engineering, Vol. 92, 1970, pp. 467-482.

13. Moore, J., "Construction of a 5-Blade Replica of the Langston Turbine Cascade with a 9.26 inch Axial Chord," Turbomachinery Research Group, Report No. JM/81-1, VPI&SU, 1981.

14. Graham, J. A. H., "Investigation of a Tip Clearance Cascade in a Water Analogy Rig," ASME Paper No. 85-IGT-65.

15. Belik, L., "Three Dimensional and Relaminarization Effects in Turbine Blade Cascades-An Experimental Study," Proceedings of 1977 Joint JSME/ASME Gas Turbine Congress, pp. 301-310.

16. Senoo, Y., "The Boundary Layer on the Endwall of a Turbine Nozzle Cascade," Trans. ASME, J. of Engineering for Power, Vol. 80, 1958.

17. Moore, J., and Ransmayr, A., "Flow in a Turbine Cascade: Part 1 - Losses and Leading-Edge Effects," ASME Paper No. 83-GT-68, Trans. ASME, J. of Engineering for Gas Turbines and Power, Vol. 106, April 1984, pp. 400-408.

18. Rayleigh, J. W. S., "Notes on Hydrodynamics," Scientific Papers, Vol. 1, Dover Publications, 1964, pp. 297-304.

19. Milne-Thomson, L. M., Theoretical Hydrodynamics, MacMillan, 5th edition, 1968, pp. 332-334.

20. Hildebrand, F. B., Advanced Calculus for Applications, Prentice-Hall, 2nd edition, 1976, p. 550.

IX. APPENDICES

A. Potential Flow Solution for Flow into a Slot

From Milne-Thomson [19], we get for Fig. A1,

$$(1) \qquad z = x + iy = \frac{2\delta_t i}{\pi + 2}\left[\tan\frac{\lambda}{2} - \lambda + \pi\right]$$

and

$$(2) \qquad \zeta = u - iv = i\, W_t \cot\frac{\lambda}{2}\ .$$

Combining (1) and (2)

$$z = \frac{2\delta_t i}{\pi + 2}\left[\frac{iW_t}{\zeta} - 2\tan^{-1}\left(\frac{iW_t}{\zeta}\right) + \pi\right]\ .$$

Now, with σ = contraction coefficient = $\frac{\pi}{\pi+2}$,

$$(3) \qquad z = \frac{2\delta_t \sigma}{\pi} i\left[\frac{iW_t}{\zeta} - 2\tan^{-1}\left(\frac{iW_t}{\zeta}\right) + \pi\right]$$

From Hildebrand [20], we see

$$(4) \qquad \tan^{-1}\left(\frac{iW_t}{\zeta}\right) = \frac{i}{2}\,\ell n\left(\frac{\zeta+W_t}{\zeta-W_t}\right)$$

and

$$(5) \qquad \ell n(-1) = i\pi\ .$$

Combining (3), (4), and (5),

$$z = \frac{2\delta_t \sigma}{\pi} i\left[\frac{iW_t}{\zeta} - i\,\ell n\left(\frac{\zeta+W_t}{\zeta-W_t}\right) - i\ell n(-1)\right]$$

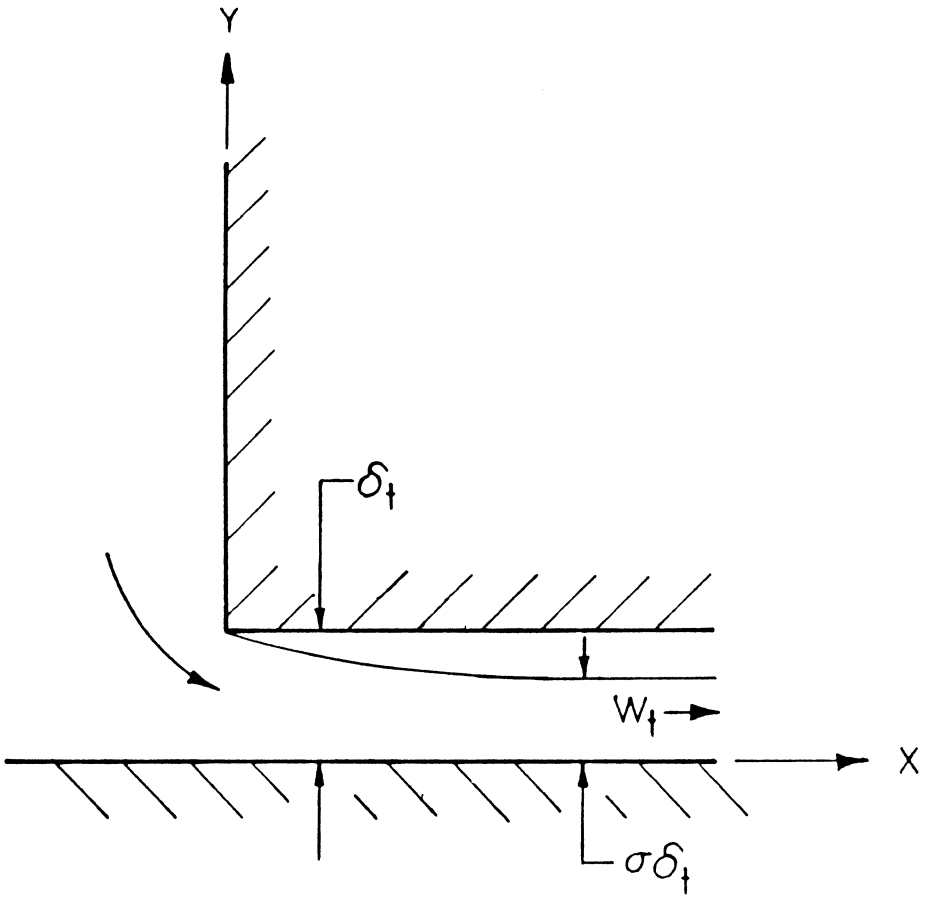

$$\sigma = \frac{\pi}{\pi+2} \quad , \quad \delta_t = \frac{2+\pi}{2}$$

Fig. A1 Tip Gap Geometry Used by Milne-Thomson [19].

and the correct form of the general solution for flow through a slot is:

$$\therefore z = x+iy = \frac{2\delta_t\sigma}{\pi}\left[\ell n\left(\frac{W_t+\zeta}{W_t-\zeta}\right) - \frac{W_t}{\zeta}\right]$$

Limiting Cases

I) Along the centerline.

Referring to Fig. A1, $z = x$ and $\zeta = u$.

$$x = \frac{2\delta_t\sigma}{\pi}\left[\ell n\left(\frac{W_t + u}{W_t - u}\right) - \frac{W_t}{u}\right]$$

and

$$\frac{2\delta_t\sigma}{\pi} = \frac{2\left(\frac{2+\pi}{2}\right)\left(\frac{\pi}{\pi+2}\right)}{\pi} = 1$$

thus

$$x = \ell n\left(\frac{1 + \frac{u}{W_t}}{1 - \frac{u}{W_t}}\right) - \frac{W_t}{u} .$$

Let $V = \frac{u}{W_t}$,

$$x = \ell n\left(\frac{1 + V}{1 - V}\right) - \frac{1}{V} .$$

Now, transform coordinates to coordinates of Fig. A2, $x = -y$.

$$\therefore y = \frac{1}{V} - \ell n\left(\frac{1 + V}{1 - V}\right)$$

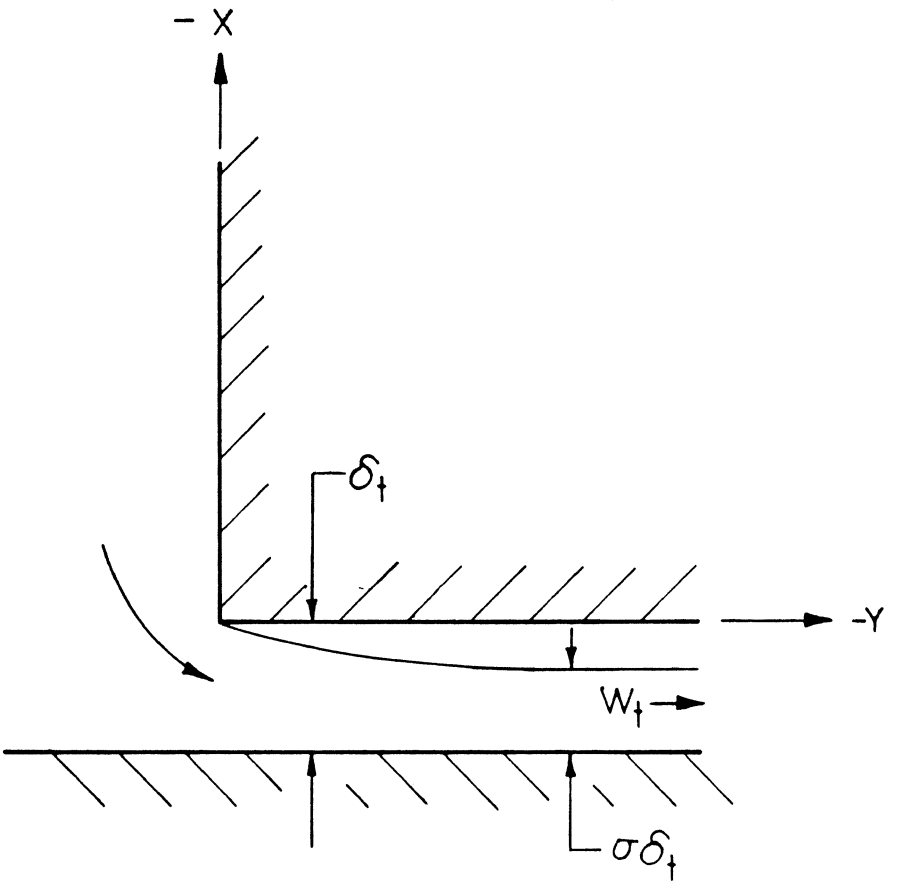

Fig. A2 Tip Gap Geometry Used by Rayleigh [18].

This matches Rayleigh's [18] solution for flow along the centerline.

II) Along the pressure surface of the wall.

Referring to Fig. A1, $z = iy$ and $\zeta = -iv$.

$$iy = \ell n \left(\frac{W_t - iv}{W_t + iv}\right) + \frac{W_t}{iv} \quad , \quad \frac{2\delta_t \sigma}{\pi} = 1$$

$$iy = \ell n(-1) + \ell n\left(\frac{iv - W_t}{iv + W_t}\right) + \frac{W_t}{iv} \quad .$$

From Hildebrand [20], we see

$$\ell n\left(\frac{iv - W_t}{iv + W_t}\right) = 2\, i\, \tan^{-1}\left(\frac{W_t}{v}\right) \quad .$$

Thus,

$$iy = i\pi + 2\, i\, \tan^{-1}\left(\frac{W_t}{v}\right) - \frac{iW_t}{v} \quad .$$

Let $V = \frac{-v}{W_t}$,

$$y = \pi - 2\, \tan^{-1}\left(\frac{1}{V}\right) + \frac{1}{V}$$

Now, transform coordinates to coordinates of Fig. A2, $x = -y + 1 + \frac{\pi}{2}$.

$$\therefore x = 2\, \tan^{-1}\left(\frac{1}{V}\right) - \frac{1}{V} + 1 - \frac{\pi}{2}$$

This matches Rayleigh's [18] solution for flow along the pressure

surface of the wall.

B. Calibration of the Statham Pressure Transducer

The pressure transducer described in Section III.F converted pressure signals into electrical signals and therefore had to be calibrated. This was performed using some of the static pressure tappings in the wind tunnel. First, a static tapping was connected to an inclined manometer and a pressure was read. Then, the tapping was connected to the pressure transducer/bridge amplifier/oscilloscope set up described in Section III.F. The bridge was balanced and the measured dial reading (MDR) off the bridge amplifier was read.

Using this data, the following calibration curve, Fig. A3, was obtained and is compared to the measured data points. A least squares fit for a straight line was used to develop the calibration curve. With the manometer accurate to ± 0.1 " H_2O, we see from Fig. A3 that all data points lie on the calibration curve within the accuracy with which they could be read.

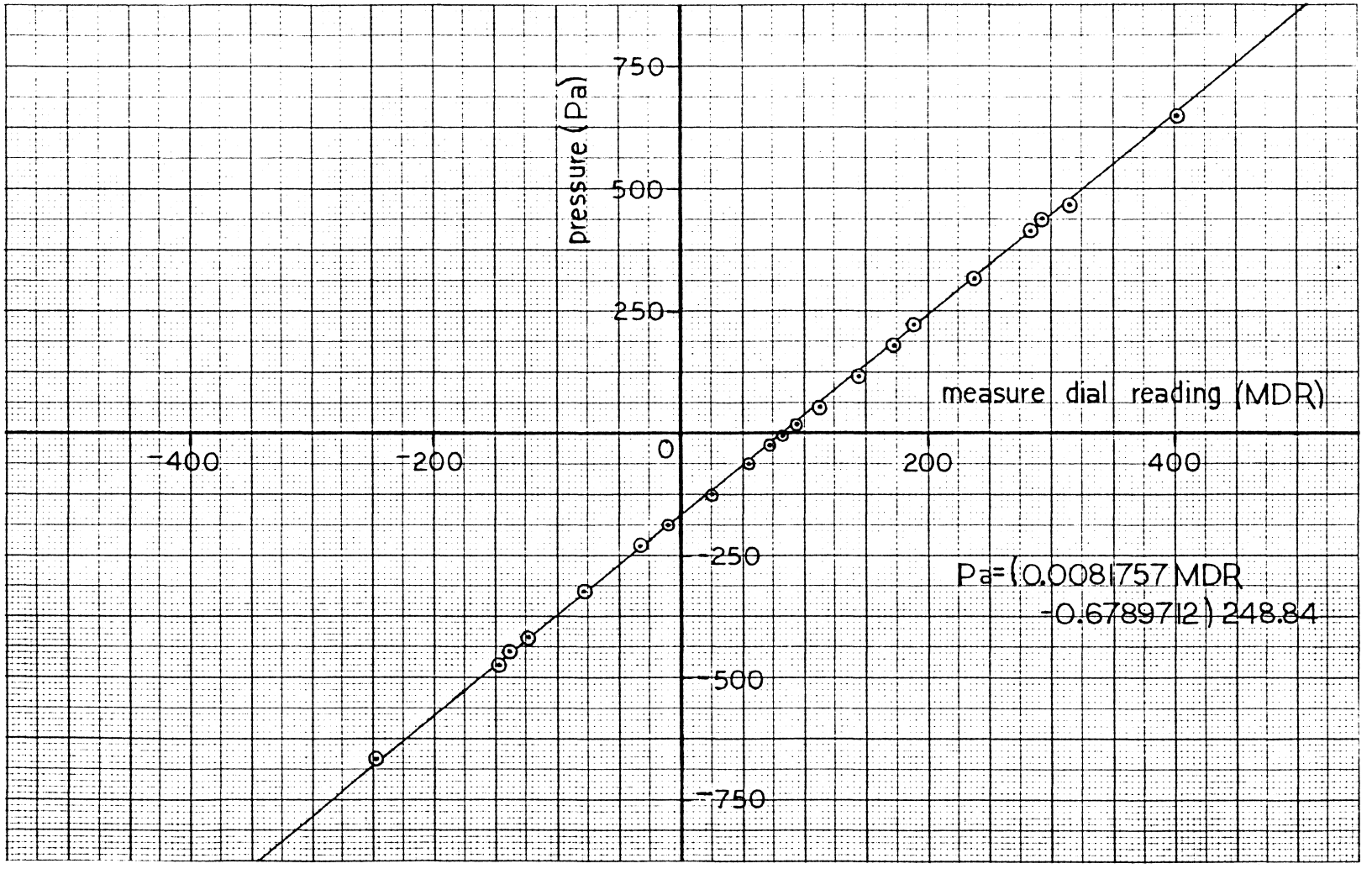

Fig. A3 Calibration Curve of Statham Pressure Transducer Serial No. 12251.

The vita has been removed from the scanned document